University of Cape Town

Minor dissertation presented in partial fulfilment of the requirements for the degree of Master of Science in Astrophysics and Space Science

in the Department of Astronomy

The Effect of the Cosmic Web on Galaxy Evolution in RESOLVE-A

Author:
Munira Hoosain

Supervisors:
Assoc. Prof. S.L Blyth
Dr R.E. Skelton

February 2021

Plagiarism Declaration

I, Munira Hoosain, know the meaning of plagiarism and declare that all of the work in the document, save for that which is properly acknowledged, is my own.

Abstract

Galaxy environment plays a significant role in galaxy evolution. While most work has focused on the effect of cluster and group environment, large scale structures, such as filaments and voids, may provide additional contributions. Recently, various authors have found correlations between galaxy morphology, stellar mass and colour, and the distance to cosmic web filaments in both simulations and data. However, the effect of filaments on the gas supply of galaxies is still under investigation due to conflicting results.

I use data from the Resolved Spectroscopy of a Local Volume (RESOLVE) survey, which is a low-redshift galaxy census complete down to log $M_\star/M_\odot$= 8.9, to study the relationship between galaxy properties and the cosmic web. I use the Discrete Persistence Structures Extractor (DisPerSE), a topology-based software package, to map filaments in the RESOLVE-A field. This work shows that galaxies in RESOLVE-A have, higher stellar masses close to filaments. When accounting for the additional effect of groups, I find no variation in the colour of galaxies with respect to their distance to filament. Low-mass (log $M_\star/M_\odot < 9.7$) galaxies increase in gas fraction with increasing distance to filament, which may indicate that low-mass galaxies lose gas as they enter filaments.

Contents

List of Figures

Chapter 1

Introduction

Galaxies do not exist in isolation but are observed to form part of an intricate cosmic web (Bond et al., 1996). This web is made up of high-density regions containing galaxy clusters connected by large, tenuous filaments and walls surrounding low-density voids. The relation between a galaxy's environment and properties, such as colour, morphology and gas content, has been well established within galaxy groups and clusters, but more work is needed to understand the effect of the cosmic web on galaxy evolution.

Of recent debate has been the effect of Large Scale Structure filaments on galaxy evolution; in particular, whether the neutral hydrogen (HI) gas content of galaxies is affected by their proximity to filaments. Simulations have shown that cold mode accretion mechanisms may allow filaments to 'feed' galaxies with additional HI gas, leading to enhancements in star formation and mass (Kereš et al., 2005). Additionally, Aragon Calvo et al. (2019) proposed a model of Cosmic Web Detachment (CWD), where star-formation is quenched in galaxies which have been cut off from filaments. Observationally, interest in this topic has been renewed thanks to the development of large radio telescopes like MeerKAT (inaugurated in 2018), and the upcoming Square Kilometer Array, which are capable of measuring faint HI signals with improved sensitivity and efficiency (Jonas & MeerKAT Team, 2016).

1.1 The Cosmic Web

The cosmic web was first observed through galaxy redshift surveys in the local universe, which mapped the three-dimensional distribution of galaxies and revealed structures such as the Perseus-Pisces supercluster (Gregory et al., 1981) and the Sloan Great Wall (Gott III et al., 2005). More recent surveys have also revealed structures like the Vela supercluster, hidden by the Milky Way's galactic plane (Kraan-Korteweg et al., 2016). The cosmic web consists of galaxy clusters and superclusters, which form the dense 'nodes', connected by filaments and walls, sheets and voids. Filaments, which range in width from 1-5 Mpc (Cautun et al., 2014), and walls (which have a larger width than length) and diffuse sheets surround low-density voids. Figure 1.1, is a composite image showing the dark matter dis-

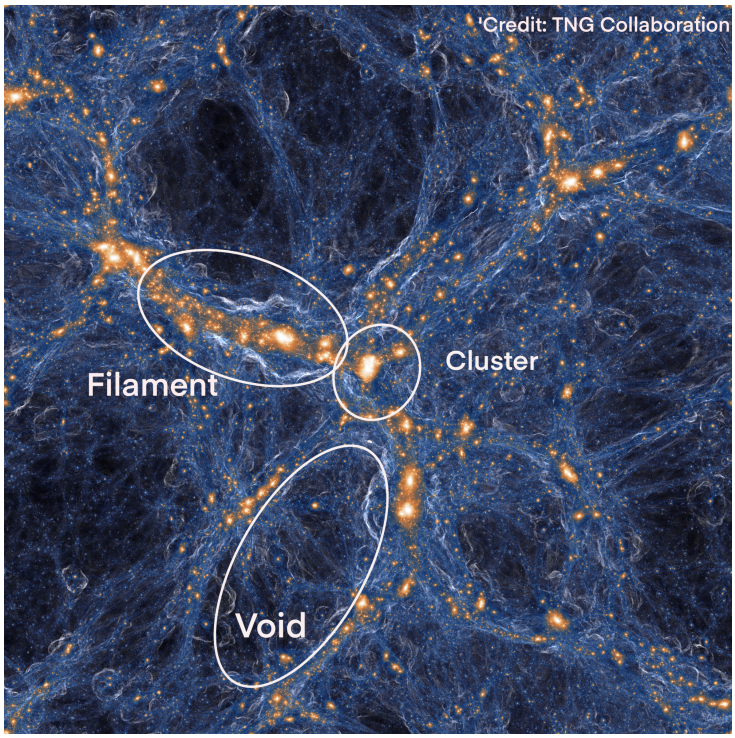

Figure 1.1: Composite image showing the dark matter distribution from the IllustrisTNG simulations. Gravitationally collapsed structures are indicated in orange and white. This figure includes examples of cluster, filament and void regions.

tribution from the IllustrisTNG simulations [1] which has been adapted to show these components.

To illustrate the relative volume occupied by the components of the cosmic web, the pie charts in Figure 1.2 (Aragón-Calvo et al., 2010a) show that while filaments occupy only $8.8\ \%$ of the universe volume, they contain nearly 40% of the mass content.

In the standard model of cosmology, the large scale structure observed today is a consequence of two mechanisms (Bond et al., 1996) : fluctuations in the initial matter density field shortly after the Big Bang, and hierarchical formation.The initial fluctuations seeded regions of overdensity and underdensity, which were amplified by gravitational collapse (Zel'Dovich, 1970). Dark matter haloes formed first, gathering baryonic matter from which galaxies could form (Mo et al., 2010). Hierarchical formation describes how large structures form from smaller structures merging together over cosmic time. Over time, these structures have evolved as matter is transported under the force of gravity. As shown by Aragón-Calvo et al. (2010a) and Cautun et al. (2014), at high redshifts, diffuse, sheet-like structures collapse into filaments - which subsequently merge together and channel matter to the dense clusters and superclusters, resulting in the prominent structures seen in the local universe today. Dark matter haloes are channelled by filaments towards overdense regions and, in the hierarchical formation model, merge together. This gives rise to

[1] Image source: IllustrisTNG (Public Domain: https://www.tng-project.org/media/)

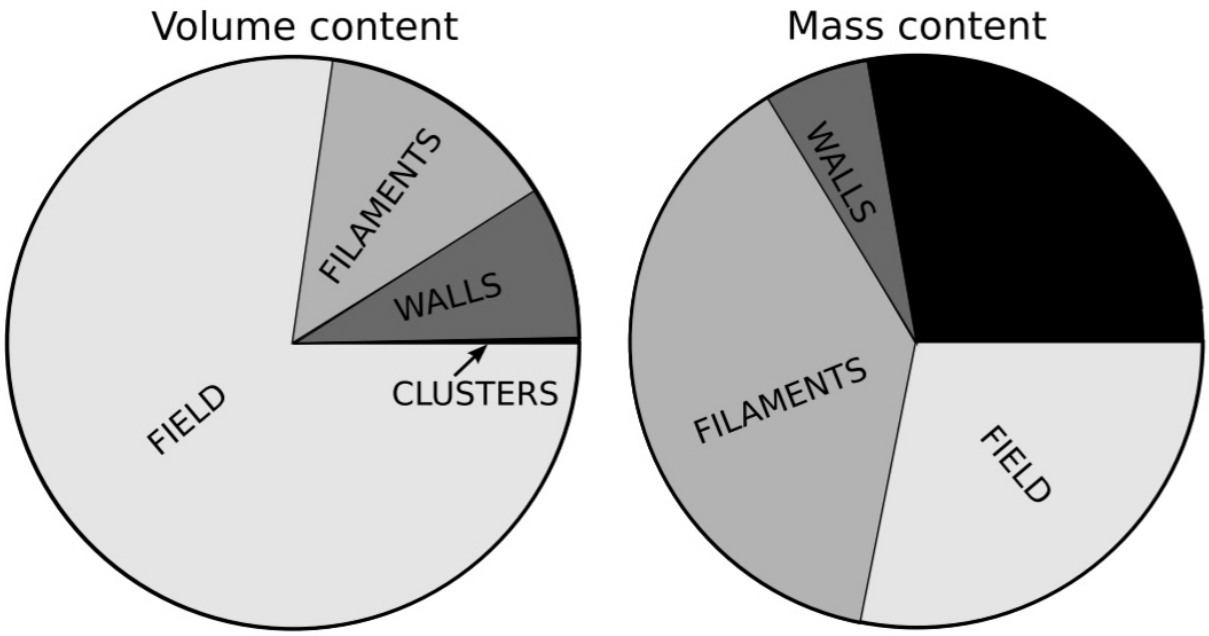

Figure 1.2: Relative volume and mass of components of the cosmic web, from Aragón-Calvo et al. (2010a). Field represents void regions. The black region indicates clusters.

galaxy clusters at the peaks of the density field, connected by filaments which surround underdense voids (Mo et al., 2010). This structure formation has been modelled in cosmological hydrodynamic simulations, such as the Millenium simulation (Springel et al., 2005), and shows that the large scale structure observed in the baryonic matter closely follows the distribution of dark matter.

Additionally, Tidal torque theory (TTT) describes how early dark matter haloes gain angular momentum during formation, resulting in the alignment or misalignment of the spin vector with large scale structures - which may impact the mass assembly of galaxies within the dark matter haloes (Peebles, 1969; Doroshkevich, 1970; Porciani et al., 2002; Laigle et al., 2015). High-mass dark matter haloes are predicted to have their spin axis perpendicular to nearby filaments and large scale structures, with low-mass haloes parallel to nearby filaments (see Kraljic et al. 2020).

1.2 Galaxy Evolution and Environment

Galaxies typically fall into two categories based on their colour, mass and general morphologies - 'red', bulge-dominated elliptical galaxies which have very little ongoing star formation, high stellar masses and are gas-poor, or 'blue' star-forming galaxies which are typically gas-rich and lower in stellar mass. For a general 'field' population, i.e. where there is no effect due to environment, this bimodality is often demonstrated by the colour-magnitude diagram, which shows that bright galaxies with a red colour index form a well-defined 'red

sequence' and galaxies with bluer colour indices create a 'blue cloud' (Baldry et al., 2004). Galaxies that are actively forming stars are bluer due to the presence of O and B type stars, which typically have a short lifespan and are no longer prominent in older, quiescent galaxies (Mo et al., 2010).

One of the indications that galaxies are affected by their environment is the morphology-density relation (Dressler, 1980). This relation shows that the proportion of early-type galaxies (i.e. elliptical and S0 galaxies) increases as environmental density increases. This may be due to an increase in galaxy-galaxy interactions, which produce early-type galaxies (Toomre & Toomre, 1972; Peng et al., 2010). A detailed analysis of galaxies in the Sloan Digital Sky Survey (SDSS) revealed that the stellar mass of galaxies increases with density and that the specific star formation rate (sSFR) is the property which is most sensitive to environment (Kauffmann et al., 2004; Peng et al., 2010). More recently, Alpaslan et al. (2015) examined the properties of galaxies with respect to large scale structure, group and pair environments in the Galaxy And Mass Assembly (GAMA) survey and found that stellar mass seems to be the most important predictor of galaxy properties, rather than large scale structure environment.

Additionally, the star formation rate density has dropped by an order of magnitude since redshift $z \sim 1$ (Hopkins, 2004). The mechanisms behind this change over cosmic time are still under investigation, but this indicates that star formation in the universe has been subject to quenching over the last $\sim$ 8 billion years.

Galaxies require a large volume of molecular hydrogen gas for star formation, which must constantly be refuelled to maintain star formation. While hierarchical merging can increase the supply of gas available to galaxies (Mo et al., 2010), large scale structure and environment also affect the gas content and therefore star formation rates of galaxies.

Cosmological hydrodynamic simulations reveal two mechanisms for gas accretion by galaxies. Gas falls into a gravitational potential well and is shock-heated to the virial temperature, before cooling and forming stars. This traditional 'hot mode' accretion is dominant for high mass galaxies. In contrast, in 'cold mode' accretion, which occurs at lower masses and does not involve shock heating prior to accretion, gas is channelled by cosmic web filaments into galaxies (Kereš et al., 2005). While cold mode and hot mode accretion are redshift-dependent, cold mode accretion dominates in low-density environments at low redshifts. Additionally, Kraljic et al. (2020) showed that the spin-alignment of galaxies with the cosmic web is linked to the accretion of HI gas from filaments.

Galaxies may also be refuelled internally through the conversion of neutral hydrogen (HI) gas to molecular hydrogen (H_2), suggesting that HI gas may be an effective tracer of a galaxy's long-term star formation potential (Mo et al., 2010). Kannappan et al. (2013) showed that galaxy mass transition scales may connect galaxy structure and gas fractions to galaxy refuelling mechanisms. Galaxies may be accretion-dominated, where galaxies grow in stellar mass rapidly by accreting gas which can be used to form new stars, process-dominated, where galaxies form stars at the same rate as fresh gas is acquired, or quenched, which is characterised by a poor gas fraction and low star formation.

Galaxy environments play a significant role in quenching star formation in galaxies by remov-

ing gas from galaxies through various mechanisms. In high and intermediate density regions like galaxy clusters and groups, galaxies can lose their gas through processes like ram pressure stripping (Gunn & Gott III, 1972), which removes cold gas from galaxies due to the intra-cluster medium (ICM) or intra-group medium (IGM); harassment (Moore et al., 1996), where galaxy-galaxy interactions affect the gas content of galaxies; tidal stripping due to interactions with other galaxies (Toomre & Toomre, 1972); or starvation mechanisms, where galaxies are cut off from gas supply mechanisms, like Cosmic Web Detachment (Aragon Calvo et al., 2019). Cosmic web Detachment (CWD) is a model which suggests that quenching happens when a galaxy is cut off from its supply of cold gas from cosmic web filaments through major mergers, satellite accretion or by crossing or infalling along the cosmic web (Aragon Calvo et al., 2019). In addition, simulations have shown that dwarf galaxies may experience cosmic web stripping, where dwarf galaxies which do not have enough binding energy to prevent ram-pressure stripping due to the gas and dark matter content of the cosmic web (Benítez-Llambay et al., 2013). Galaxy groups are particularly noteworthy in quenching galaxies before they enter denser, cluster environments through pre-processing (Fujita, 2004), where various processes such as galaxy-galaxy interactions, strangulation and evaporation remove gas from galaxies and induce quenching. This may contribute to the morphology-density relation, and may also occur in filaments (Sarron et al., 2019; Odekon et al., 2018).

Galaxy environments play a crucial role in the evolution of galaxies. Although stellar mass is one of the most important factor in determining a galaxy's evolution, the effects on the gas content due to environment have the potential to induce changes in galaxy properties such as colour and star formation rate.

1.3 Observed Properties of Galaxies in the Cosmic Web

Galaxy evolution in the cosmic web has been a subject of interest over the past 10 years. Earlier work on the cosmic web focused on the cosmological properties of filaments, with studies looking at Tidal Torque Theory and results from cosmological hydrodynamic simulations showing interest in the spin properties of galaxies. While spin remains a topic of interest, recent works have focused on how galaxies have evolved under the influence of their location in the cosmic web environment.

One of the most consistent trends within the literature is that the stellar mass of galaxies in filaments is typically higher than galaxies outside of filaments (Laigle et al., 2017; Chen et al., 2017; Luber et al., 2019; Welker et al., 2019; Malavasi et al., 2017). This has been observed at various redshifts and using different filament finding methods.

Changes in galaxy morphology are an indicator of processes such as merging and quenching. Kuutma et al. (2017) found an increase in the fraction of early-type galaxies close to filaments. Additionally, Santiago-Bautista et al. (2020) found an increase in the elliptical to spiral ratio close to filaments, indicating that filaments - as intermediate density regions - follow the morphology-density relation.

Closely tied to stellar mass and morphology, galaxy colours indicate the star formation prop-

erties of galaxies. Kuutma et al. (2017), Chen et al. (2017), Kraljic et al. (2017) and Luber et al. (2019) found that galaxies were redder within filaments compared to galaxies outside of filaments. Kuutma et al. (2017) and Kraljic et al. (2017) found that these redder colours corresponded to a decrease in the specific star formation rates for galaxies in filaments. Additionally, Sarron et al. (2019), Blue Bird et al. (2020), Laigle et al. (2017) and Malavasi et al. (2017) found increases in the fraction of passive (i.e. non-star forming) galaxies within filaments, indicative of quenching due to the filaments.

While several studies have examined the stellar properties of galaxies in filaments, more observations are needed to understand the gas properties of galaxies. Kleiner et al. (2016) showed that galaxies with $\log M_\star / M_\odot > 11$ had higher HI masses within filaments compared to galaxies in a control sample outside of filaments, when correcting for density, providing direct evidence for gas accretion from filaments. However Odekon et al. (2018) found conflicting results in a lower mass regime ($8.5 < \log M_\star/M_\odot < 10.5$), using data from the ALFALFA survey, showing that galaxies lose HI gas as they enter filaments and redden as they are quenched. Using preliminary observations from the CHILES survey and photometric HI estimations, Luber et al. (2019) and Blue Bird et al. (2020) suggest that the gas fraction of galaxies may increase away from filaments. However, the differing mass ranges between the studies on the gas content of galaxies with respect to filaments may suggest that stellar mass affects whether galaxies replenish or lose gas from the cosmic web (Odekon et al., 2018).

The spin alignment (or mis-alignment) of galaxies is mass-dependent and may allow galaxies to accrete gas from the cosmic web, as shown by simulations (Kraljic et al., 2020; Laigle et al., 2015; Laigle et al., 2017). Galaxy spin alignments with nearby filaments were first observed by Tempel et al. (2013) and Tempel & Libeskind (2013). Welker et al. (2019) presented the first detection that this spin alignment may be mass dependent, in agreement with simulations. This was followed by Blue Bird et al. (2020), who observed galaxies with their spin aligned to nearby filaments.

These observations show distinct differences between galaxies in different large scale structure environments, beyond simulations. Galaxies in close proximity to filaments have higher stellar masses and redder colours, and follow the morphology-density relation. However, while the spin and gas properties are related, more observations are needed to understand the complex processes that affect the gas content and refuelling of galaxies with respect to filaments.

1.4 Problem Statement

As I have shown, the cosmic web and galaxy environments are important for observational studies and theoretical models to consider in understanding how galaxies evolve. Observations point to effects of the cosmic web on galaxy morphology, through measurements of the elliptical-to-spiral ratio and consistent trends showing that galaxies close to filaments have more mass and are more passive than their counterparts further away. However, the impact on the neutral gas properties of galaxies in filaments is still not well understood,

despite its importance in theories of detailing how galaxies are refuelled.

It is important to note that few of the studies of galaxy evolution in filaments distinguish between filaments and galaxy groups, which may be embedded in filaments and drive similar observational trends. Groups pre-process galaxies, resulting in quenched galaxies (Fujita, 2004; Sarron et al., 2019). While the morphology-density relation (Dressler, 1980) indicates that galaxy evolution is affected by local density, it does not account for the additional effect of filaments. Untangling the effect of the cosmic web from the effect of groups and clusters is important for understanding galaxy evolution models. Furthermore, understanding this impact at low redshift will feed into our expectations at high redshifts, which is relevant for upcoming surveys like LADUMA on the MeerKAT telescope.

The aim of this project is to identify filaments in the local universe and investigate the properties (such as stellar mass, colour and gas fraction) of the galaxies inside and outside the filaments to examine the role filaments might play on the evolution of galaxies. To do this, I will use data from the REsolved Spectroscopy Of a Local VolumE (RESOLVE) survey (Kannappan & Wei, 2008), which is a highly complete census of the local universe. I will map the cosmic web filaments, accounting for the group environments to examine how filaments affect galaxy evolution properties.

Throughout this work, the standard ΛCDM model is assumed with $\Omega_{\rm M}$ = 0.3, Ω_{Λ} =0.7 and H_0 = 70 km/s/Mpc. Chapter 2 provides an overview of the data used in this project from the REsolved Spectroscopy Of a Local VolumE (RESOLVE) survey (Kannappan & Wei, 2008), the accompanying Environmental COntext (ECO) survey (Moffett et al., 2015) and SIMBA simulations (Davé et al., 2019). Chapter 3 provides an overview of the various methods for detecting filaments, motivates my choice of method and explains its mathematical framework. An outline of the steps taken to prepare the data is also presented in Chapter 3. The analysis of galaxy properties with respect to filaments and the results of this analysis are presented in Chapter 4. Finally, Chapter 5 discusses the results in context and the summary, conclusion and outlook for future work are presented in Chapter 6.

Chapter 2

Data

2.1 The RESOLVE survey

The analysis of galaxy properties with respect to filaments in this dissertation relied on using observational data from the third data release (DR3) of the REsolved Spectroscopy Of a Local VolumE (RESOLVE) (Kannappan & Wei, 2008) survey, as well as simulated data from the SIMBA simulations (Davé et al., 2019). The RESOLVE survey is a volume-limited census of the local universe. RESOLVE is highly complete down to low mass, gas rich galaxies ($M_{bary} \sim 10^{9.1-9.3}$ $M_{\odot}$), where M_{bary} = ($M_{\star}$+ 1.4 M_{HI}), and covers a wide range of physical scales. The survey includes high-resolution gas and stellar kinematic information, enabling detailed studies of galaxy properties. Additionally, RESOLVE is accompanied by a group catalogue (Eckert et al., 2017) and the Environmental COntext catalogue (ECO) (Moffett et al., 2015), which provides a 1 Mpc buffer around the edges of the RESOLVE-A field. The comprehensive redshifts and group catalogue available for RESOLVE ensure that three-dimensional positions of galaxies can be presented accurately and corrected for redshift space distortions, which is crucial for mapping filamentary structures.

RESOLVE consists of two fields, RESOLVE-A and RESOLVE-B. Collectively, the survey extends to a velocity range of 4500 km/s < cz < 7000 km/s and occupies a total volume of $\sim$ 52 000 Mpc^3. Details of the two fields can be found in Table 2.1

Additionally, survey membership was refined using galaxy groups. The Friends-of-Friends algorithm as described in Berlind et al. (2006) was used to determine the galaxy groups with an on-sky linking length = 0.07 and a line-of-sight linking length = 1.1 (see Eckert et al.

	RESOLVE-A	RESOLVE-B
R.A.	131.25 ° < R.A. < 236.25°	22 hr < R.A. < 3 hr
Dec.	0 ° < Dec. < 5°	-1.25° < Dec. < +1.25°
Volume	$\sim$ 38 400 Mpc^3	$\sim$ 13 700 Mpc^3
Completeness limit (r-band)	M_r < -17.33	M_r < -17

Table 2.1: Properties of the RESOLVE A and B fields

(2016)). If a galaxy fell within the volume boundary, but belonged to a group outside of the survey volume, it was excluded from the survey. Likewise, if a galaxy fell outside the survey volume, but was associated with a group that belonged within the volume, it was included in the survey.

Figure 2.1 from Eckert et al. (2015) shows the RA and *cz* distribution of both fields. In total, RESOLVE-A, which is the focus of this study, contains $\sim$ 1490 galaxies.

2.1.1 Data Overview

The RESOLVE data reduction, galaxy properties and photometric gas fraction estimates are presented in Eckert et al. (2015). The atomic (HI) gas census is described in Stark et al. (2016). In this section, I will briefly summarise these processes.

Photometry and Spectroscopy

Optical data for the RESOLVE survey was drawn from several catalogues, including the SDSS redshift survey (Aihara et al., 2011), the updated Zwicky catalogue (Falco et al., 1999), UKIDSS YHK photometry (Hambly et al., 2008), 2MASS *JHK* (Skrutskie et al., 2006) and *GALEX* NUV (Morrissey et al., 2007), which were supplemented with observations from various telescopes. The data were reprocessed with custom sky subtraction and multiple extrapolation techniques were used to measure total flux and systematic errors with the methods by described by Kannappan et al. (2013). From this improved photometry, extinction-corrected colours and galaxy mass estimates were produced using Spectral Energy Distribution (SED) fitting with the parameters from Eckert et al. (2015). The u-r colours, which are used in this work, were corrected for internal and foreground extinction and include k-corrections. The colour-magnitude diagram is shown in Figure 2.2. The colour-magnitude diagram shows that the sample is dominated by the blue cloud, which consists of lower mass, gas-rich galaxies with ongoing star formation, and features a minimal red sequence. As shown in Stark et al. (2016), RESOLVE features a variety of environmental densities. Additionally, these features are typical for when most galaxies fall within low to intermediate density regions, rather than high density clusters.

HI data

The atomic gas census for RESOLVE was presented by Stark et al. (2016). In summary, the HI data was sourced from the ALFALFA survey (Giovanelli et al., 2005), which overlapped with the RESOLVE footprint, archival data compiled by Springob et al. (2005) and new observations with the Green Bank Telescope (GBT) and Arecibo telescope. Stark et al. (2016) cross-matched RESOLVE with the ALFALFA catalogue and additionally searched the ALFALFA data cubes for galaxies which did not have counterparts in the ALFALFA catalogues, yielding upper limits on the HI mass or weak detections.

The new observations with the GBT and Arecibo are described in Stark et al. (2016). Galaxies with 'confused' detections - i.e., where two or more sources were present within the telescope beam were de-confused using their known redshifts and expected HI linewidths

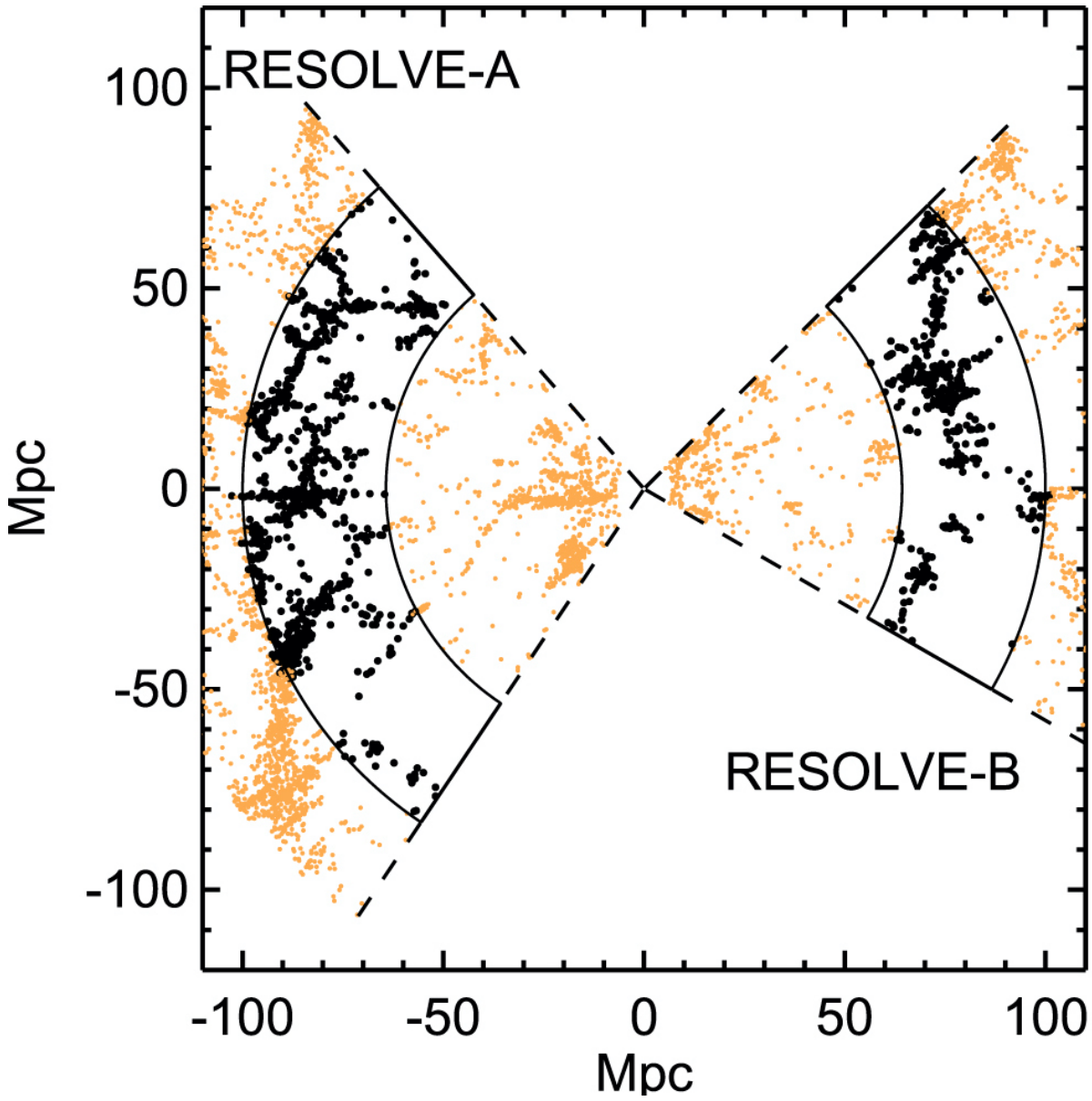

Figure 2.1: The RA-*cz* distribution of galaxies in RESOLVE-A and RESOLVE-B from Eckert et al. (2015). The RESOLVE subvolumes are outlined in black. The orange data points represent galaxies which fall in groups outside of the survey volume.

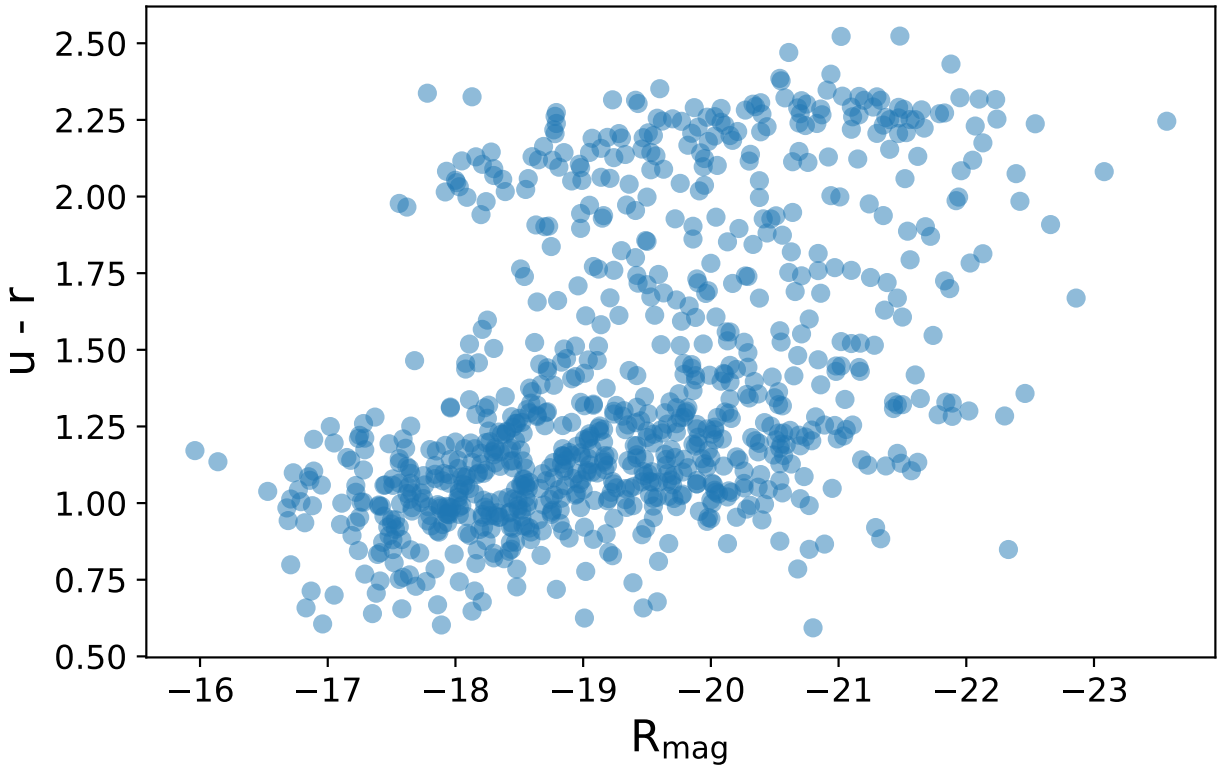

Figure 2.2: The colour-magnitude diagram for galaxies in the RESOLVE-A sample is shown using the *u*-*r* colour and absolute R magnitudes.

where possible. HI masses and upper limit estimates were determined by analysis of the 21 cm line profiles.

To create a complete census of HI masses and gas fraction measurements and estimates, supplementary techniques, such as photometric gas fraction estimates, were used where direct, high signal-to-noise (S/N > 5) detections were unavailable. Photometric gas fractions were calculated using the tight correlation between observed galaxy colour and gas fraction (Kannappan, 2004). In Eckert et al. (2015), the correlation between the u-J SED modelled colour and the log gas-to-stellar mass ratio of galaxies with direct HI measurements, as well as the b/a axis ratio was used to predict the photometric gas fraction for galaxies in RESOLVE.

In summary, the 'optimal combination' of direct detections, upper limits and photometric gas fractions, as described in the RESOLVE Data tutorial (Kannappan, 2019), was used as follows:

- Direct HI detections from Stark et al. (2016), consisting of high signal-to-noise detections (S/N > 5), low signal-to-noise detections (S/N <5) and successfully de-confused detections are used where available
- Strong upper limits, where 1.4 $M_{HI}/M_{\star}$< 0.05, are treated as HI measurements (see Stark et al. (2016) and Eckert et al. 2016)
- Photometric gas fraction estimates from Eckert et al. (2015), are used:
  - to replace missing HI data
  - for galaxies with weak upper limits, i.e. where 1.4 $M_{HI}/M_{\star}$> 0.05 (see Eckert et al. 2016), provided that the photometric gas fraction estimate is less than the gas fraction determined using the weak upper limit
  - where HI detections could not be de-confused because the galaxies overlapped strongly in velocity-space (see Stark et al. 2016).

Figure 2.3 shows the number of galaxies with direct HI detections, upper limits and photometric gas fraction estimates in low, intermediate and high mass bins. At low and intermediate masses, most HI measurements are sourced from direct detections. Because low and intermediate mass galaxies are typically more gas-rich than high mass galaxies (Kannappan et al., 2013), these distributions are expected.

Dark matter halo masses

Dark matter halo masses were estimated using the Friends-of-Friends groups and halo abundance matching, as described in Eckert et al. (2016). The most massive galaxy in each group is marked as the central, while all other galaxies in each group are marked as satellites. Additionally, single galaxies are marked as centrals.

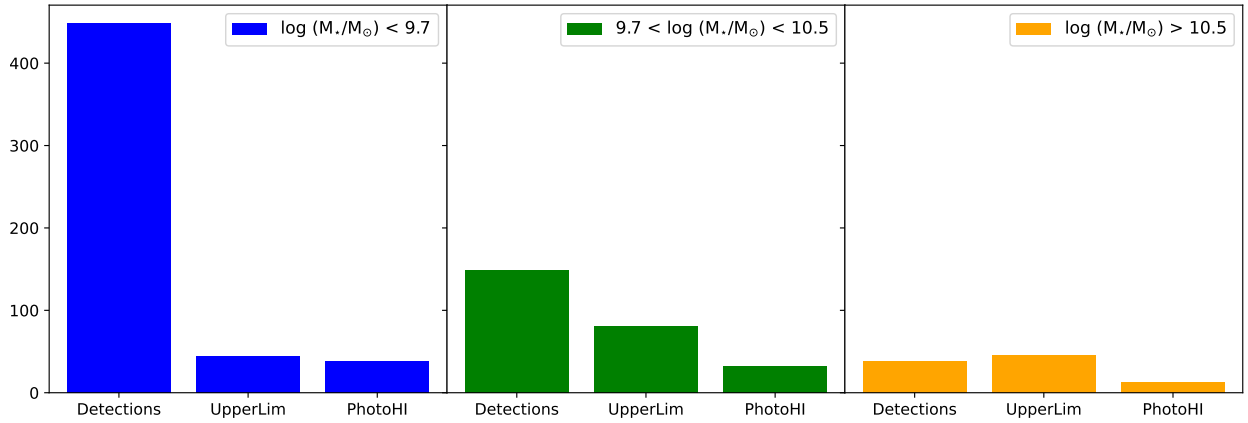

Figure 2.3: Bar plots showing the distribution of HI measurement types - direct detections, upper-limits and photometric gas fraction estimates. The left plot (blue) shows the distribution for low mass galaxies (log $M_\star/M_\odot$< 9.7), the middle plot (green) shows the distribution for intermediate mass galaxies (9.7 < log $M_\star/M_\odot$< 10.5) and the right plot (yellow) shows the distribution for high mass galaxies (log $M_\star/M_\odot$> 10.5)

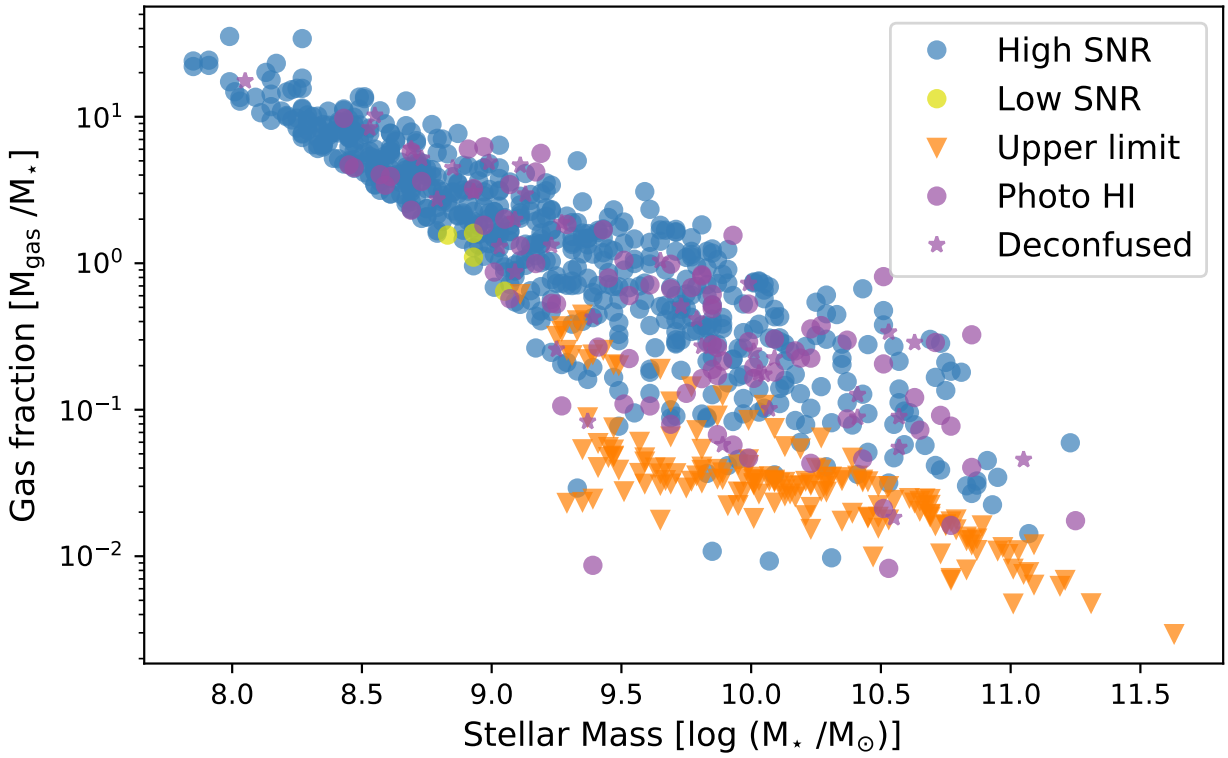

Figure 2.4: Stellar mass vs Gas Fraction for galaxies within the baryonic-mass selected sample in RESOLVE-A. Blue circles represent high signal-to-noise ratio measurements (S/N > 5) (Stark et al., 2016). Lime circles represent galaxies with low signal-to-noise HI detections (S/N < 5). Orange triangles represent upper limit estimates defined in Eckert et al. (2016). Purple circles represent galaxies with photometric gas fraction estimates (Eckert et al., 2015) and purple stars represent successfully deconfused HI measurements.

Sample selection

The RESOLVE survey defines four possible samples within the database according to the volume, luminosity, baryonic and stellar mass limits. Selecting one of these samples ensures consistency and completeness across measurements. Because I am investigating the gas properties of galaxies with respect to the cosmic web, I selected the baryonic mass complete sample with 4500 km/s < Group *cz* < 7000 km/s and complete to log $M_{\rm bary}$ > 9.3 for RESOLVE-A. Because this sample is selected based on a combination of HI mass and stellar mass, it probes galaxies which are more gas-rich than the other samples sample. Figure 2.4 shows the stellar mass vs. gas fraction measurements for each galaxy in the RESOLVE catalogue, as well as which type of HI measurement was used.

2.2 SIMBA simulation data

Cosmological hydrodynamic simulations are useful tools for comparing observational results with theoretical understanding. The SIMBA simulations (Davé et al., 2019) are the next-generation of the MUFASA simulations (Davé et al., 2016), which focus on galaxy evolution over cosmic time. These simulations are state-of-the-art and successfully match observations in many scenarios (Davé et al., 2019), modelling the gas, stellar and dark matter properties of galaxies effectively. Additionally, they have been used by Kraljic et al. (2020) to study the effect of the cosmic web on galaxy spin and gas properties. SIMBA is improved due to its modelling of black hole growth, Active Galactic Nuclei (AGN) feedback, X-ray feedback and dust production and destruction (Davé et al., 2019).

Additionally, ongoing collaborations between SIMBA, RESOLVE and LADUMA are already established, providing access to the data and expertise. In this project, I make use of SIMBA Snapshot `m100n1024_151` from the `s50j7k` model of the simulation [Davé: private communication]. This run of the simulation resolves galaxies at $M_\star \geq 5.8 \times 10^8$ $M_\odot$ and this snapshot corresponds to a $100 \times 100 \times 100$ Mpc^3 box at $z = 0$.

Chapter 3

Method

There are several methods for identifying the components of the cosmic web. One of the earliest approaches used graph-theory to map the voids and superclusters (Zeldovich et al., 1982). More recently, Alpaslan et al. (2014a) used Minimum Spanning Trees to map filaments in the Galaxy and Mass Assembly (GAMA) survey. Stochastic methods, such as the *Bisous* method employed by Tempel et al. (2014), and Hessian-based methods, including the NEXUS (Cautun et al., 2013) and Multiscale Morphology Filter (Aragón-Calvo et al., 2007) formalisms, have been used to identify components of the cosmic web. Additionally, novel, interdisciplinary approaches such as the growth of slime mould have been proposed to study the cosmic web (Burchett et al., 2020).

In this work, the Discrete Persistence Structures Extractor (DisPerSE) is used (Sousbie, 2011; Sousbie et al., 2011). Like the SpineWeb formalism (Aragón-Calvo et al., 2010b), DisPerSE takes advantage of geometric and topological tools to identify cosmic web filaments from a galaxy distribution.

This chapter will describe the computing support used for this project, provide a brief overview of the topological concepts applied in DisPerSE and describe the commands and functions used for filament finding. Once this technique has been established, data from the SIMBA simulations (Davé et al., 2019) are used to test the limits of DisPerSE and ensure that reliable filaments will be detected when applied to observational data. The processes used to prepare the observational data are described before DisPerSE is used to identify filaments within RESOLVE-A. Lastly, the boundary conditions are tested within DisPerSE and the distance metrics used within this work are described and calculated.

3.1 Data Processing with IDIA

The Inter-University Institute for Data-Intensive Astronomy (IDIA) was established to process the large amounts of data produced by the MeerKAT telescope and create capacity for the upcoming SKA in South Africa. IDIA utilises the ilifu cloud computing facility to service the computational needs of the MeerKAT community. Ilifu provides cloud computing resources to users across the world through a Jupyter Hub web browser interface and

command-line capabilities.

As this project falls under the LADUMA Large Survey Project on MeerKAT of which I am a member, I was provided with access to IDIA's services for my research. The open-source DisPerSE software was installed on the ilifu cloud for the purpose of this project and future work on large scale structure by the LADUMA team. A DisPerSE software container was also created by the IDIA team for reproducibility and ease of installation.

Throughout the project I used the `python` programming language through Jupyter notebooks, including packages such as `numpy`, `scipy`, `matplotlib` and `astropy`, for data processing and analysis. Additionally, I used the open-source `Paraview` application to visualise filaments and other structures in 3D since it allows panning, zooming and rotation with ease.

3.2 DisPerSE

The Discrete Persistence Structures Extractor (DisPerSE) (Sousbie, 2011; Sousbie et al., 2011) is the primary method used to determine large scale structure in this work. DisPerSE uses a combination of topological methods, such as the Delaunay Tessellation Field Estimator (DTFE) (van de Weygaert & Schaap, 2009; Schaap & van de Weygaert, 2000), Discrete Morse Theory (Forman, 1998, 2002) and Persistence Theory (Edelsbrunner et al., 2000) to identify structures. DisPerSE was originally designed for studying the cosmic web, but has been applied in other areas of astrophysics research.

Unlike other structure finding methods, DisPerSE is scale free and parameter free and can be applied to smaller fields. DisPerSE is also freely available and accessible. The topological methods are robust and objective, which is advantageous in three dimensions, where visual identification of structures can be challenging. DisPerSE is a widely-used (Kraljic et al., 2017; Laigle et al., 2017; Luber et al., 2019; Malavasi et al., 2017), and reliable when compared to other structure finding methods (see Libeskind et al. (2018) for an in-depth comparison).

3.2.1 General Concepts

DisPerSE relies on several mathematical concepts, the Delaunay Tessellation Field Estimator, Discrete Morse theory and Persistence theory, to extract filaments, walls and other structures from the galaxy distribution. In this section, I will provide a simplified explanation of these concepts, adapted from Sousbie et al. (2011) and how DisPerSE takes advantage of them. For an in-depth explanation of this mathematical framework, refer to Sousbie (2011).

Delaunay Tessellation Field Estimator

The Delaunay Tessellation Field Estimator (DTFE) is a geometric tool for estimating the density field from a discrete distribution and was developed by van de Weygaert & Schaap

(2009). The tessellation works by dividing the field into triangles in such a way that, if all three vertices lay on the circumference of a circle, that circle (called the circumcirle) would not contain any other points from the distribution. Triangles in high density regions would therefore be smaller in size than triangles in low density regions. This is illustrated in Figure 3.1

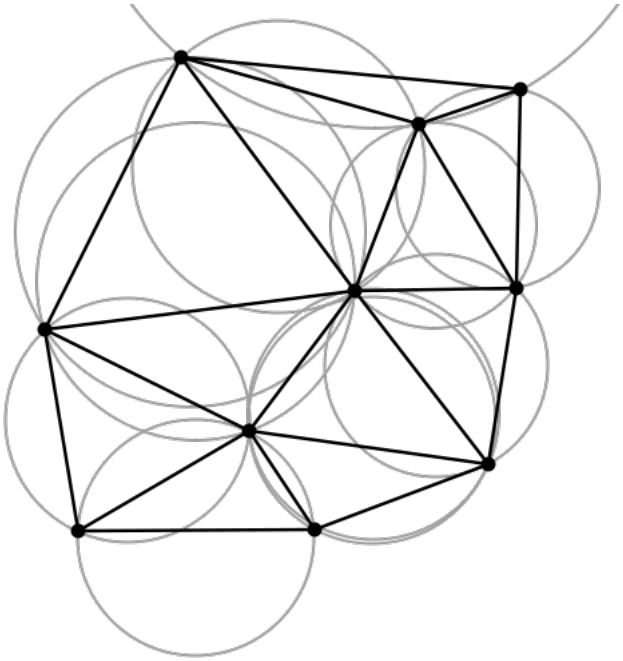

Figure 3.1: The Delaunay Tessellation of a set of points from (WikipediaCommons, 2013) is shown in black. The circumcircles are illustrated by the grey lines.

The area of each triangle in the tessellation is thus inversely proportional to the density of points. This triangulation can therefore be used to determine the density field . The Delaunay tessellation can be defined in higher dimensions, but in this application it is restricted to 2D and 3D.

Discrete Morse theory

DisPerSE uses a discrete application of Morse theory (Forman, 1998, 2002) to find the relationship between the density field and its topology. Morse theory is based on Morse functions, which are a type of twice-differentiable, smooth scalar functions (see Milnor (2016) for an overview of Morse Theory). In practical terms, DisPerSE uses Discrete Morse theory to segment the density field into regions, or cells, based on the gradient.

This requires two components of Morse functions, critical points and integral lines. Critical points are points where the gradient is null and can be minima, maxima or saddle points. Integral lines are curves tangent to the gradient field at every point. Each point has exactly one integral line passing through it, which are gradient lines passing from one critical point to another (see Figure 3.2). Integral lines originating or ending at the same critical point divide

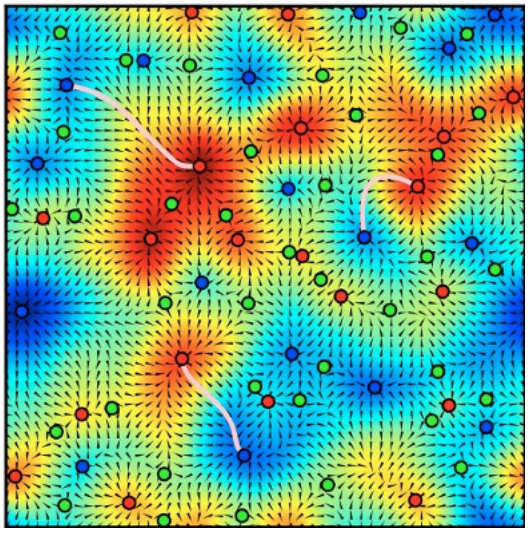

Figure 3.2: This figure from Sousbie et al. (2011) shows the gradient of a field, with black arrows indicating the direction of the gradient. Minima are shown as blue points, saddle points in green and maxima as red points. Examples of integral lines of a Morse function are shown as pink lines.

the space into manifolds. Ascending manifolds are the sets of points belonging to integral lines whose destinations are the same minima (see Figure 3.3), while descending manifolds are described by integral lines ending at maxima (see Figure 3.4). The type of critical point (maximum, minimum or saddle point) associated with the manifold also defines the index assigned to the manifold. The set of these manifolds is called the Morse Complex.

The intersection of an ascending and descending manifold is called a p-cell. Segmenting the space into p-cells makes up the Morse-Smale Complex (see Figure 3.5, which is then used to determine cosmological structures. From the Morse-Smale complex, DisPerSE can return cosmological structures from the corresponding type of manifold and index. Voids are represented by ascending 0-manifolds, walls are represented by ascending 1-manifolds and filaments are represented by ascending 2-manifolds.

Persistence Theory

DisPerSE uses a a topological concept called persistence to evaluate the robustness of structures found from the Morse-Smale Complex. Persistence evaluates the topological robustness by examining pairs of critical points.

To evaluate the robustness of structures, a threshold is chosen and the set of points that are above that threshold is examined. The value of the threshold is varied until it crosses a critical point. If the critical point is a maximum, this creates a new topological feature in the set of points, or destroys a topological feature in the set of points if the critical point is a minimum.

These critical points are combined into *persistence pairs*, consisting of a positive component (at maxima) and a negative component (at minima). The absolute difference in the values of

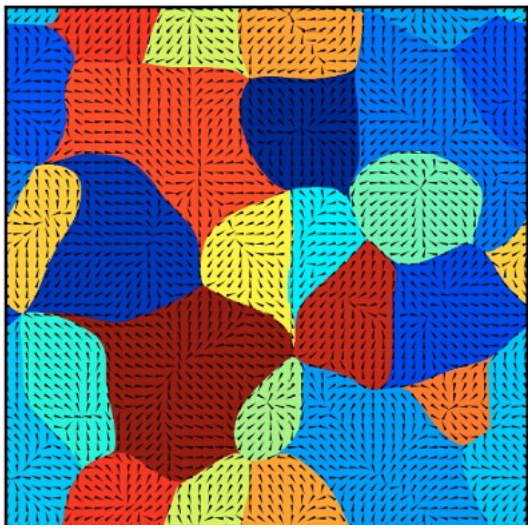

Figure 3.3: This figure from Sousbie et al. (2011) shows the set of ascending manifolds. i.e. the set of points belonging to integral lines whose destination is the same minimum.

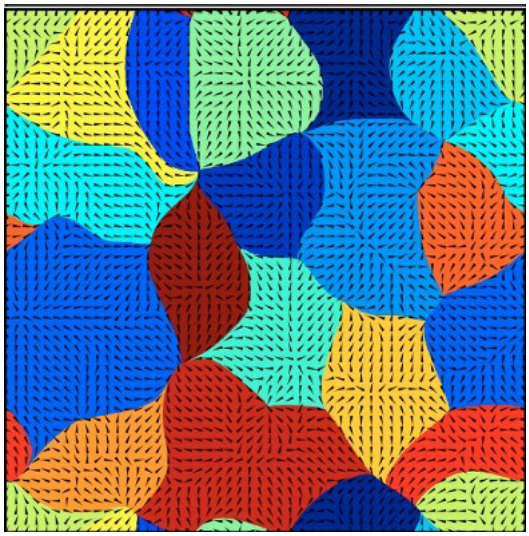

Figure 3.4: This figure from Sousbie et al. (2011) shows the set of descending manifolds. i.e. the set of points belonging to integral lines whose destination is the same maximum.

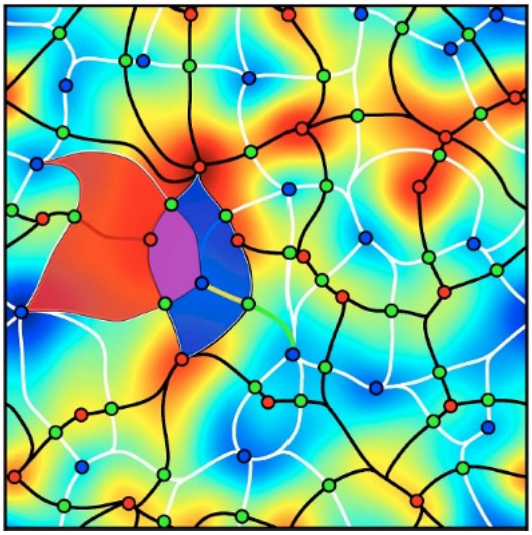

Figure 3.5: This figure from Sousbie et al. (2011) illustrates the Morse-Smale Complex. The blue region corresponds to a descending manifold shown in Figure 3.4, and the red region shows an ascending manifold from Figure 3.3. The purple region shows a p-cell: the intersection of ascending and descending manifolds. Black lines map the boundaries of the descending manifolds and white lines map the boundaries of the ascending manifolds.

the negative and positive critical points is called the *persistence* of the pair. This is illustrated in Figure 3.6

This persistence value is a measure of the robustness. Features that are created by noise will have smaller persistence values and can be removed by setting the persistence threshold in DisPerSE. The persistence may also be expressed as a ratio.

In DisPerSE, the persistence threshold can be set manually, but is typically expressed as a number of sigmas calculated by evaluating the probability that a pair with given persistence ratio occurs in a pure random discrete Poisson distribution.

3.3 Running DisPerSE

DisPerSE allows users to select one of four types of boundary conditions to apply when evaluating the Delaunay Tessellation Field Estimator. This is important for correctly determining the topology of the distribution. The possible boundary conditions are as follows:

- smooth: new particles are added outside the distribution based on the density at the edges.
- mirror: the distribution outside is a mirrored copy of the distribution inside
- periodic: the space outside is 'paved' with copies of the distribution
- void: no boundary is added

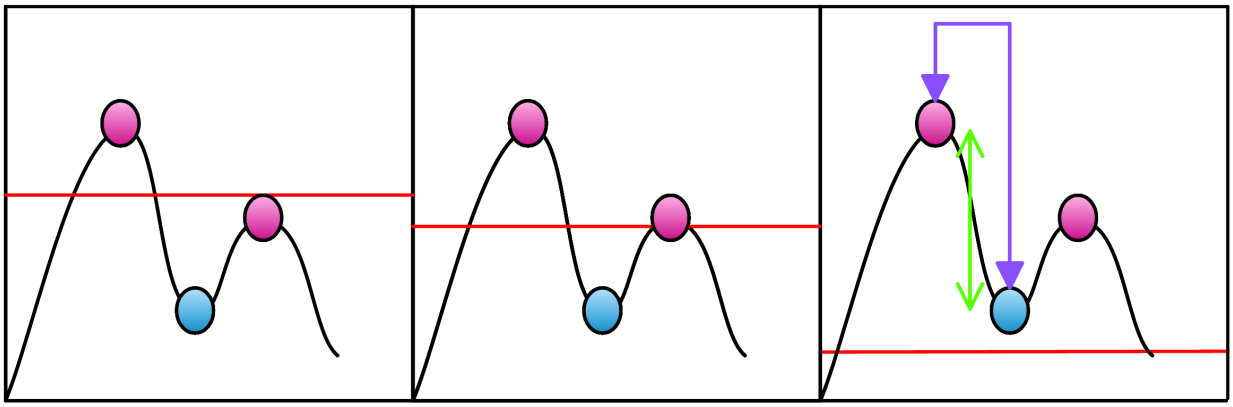

Figure 3.6: This figure illustrates how the persistence is determined. The first panel shows a function with critical points marked in pink (maxima) and blue (minima). The red line indicates the chosen threshold. In the second panel, the threshold crosses a maximum, creating a new topological component in the set of points above the threshold. The third panel shows a pair of critical points, or a persistence pair, indicated by the purple arrows. The green line indicates the persistence value of the pair - i.e. the difference in value between the maximum and minimum. This figure is adapted from Sousbie et al. (2011).

Because the smooth boundary condition is recommended in the online DisPerSE manual for 3D galaxy distributions, which have irregular shapes, it was selected as the fiducial boundary condition. The other boundary conditions will be evaluated on the observational data in Section 3.6.

For the next step, the density field is used to determine the Morse-Smale Complex and the filament 'skeleton' is extracted. The procedure is as follows:

- Use the `mse` function, setting the persistence threshold at the desired level. The 5σ level is commonly selected to produce reliable filaments. The `-forceloops` and `-robustness` commands are applied to this function to remove spurious structures created by the underlying topology and ensure that the returned filaments are robust. The `-manifolds` command is also applied to output the ascending and descending manifolds for later inspection
- The filaments are smoothed and extracted using the `skelconv` function. Filament segments which double back on themselves are merged by applying the `-breakdown` command. The format for exporting the full filament skeleton in vtu format for visualisation in Paraview can be selected with the `-to vtu` command. Alternatively, the filament segments may be exported in ascii format using the `-to segs_ascii` command and critical points may be exported using the `-to crits_ascii` command.

The highest density regions, called nodes, are represented by critical points which are maxima. These are nodes are identified as critical points with the type = 3 when 3-dimensional data are used.

Lastly, the filaments and data points are imported into Paraview for visual inspection to

Sample	Baryonic mass limit	Number of galaxies
High mass limit	$\log(M_{bar}/M_{\odot}) > 10.5$	103
Intermediate mass limit	$\log(M_{bar}/M_{\odot}) > 10$	349
RESOLVE-A mass limit	$\log(M_{bar}/M_{\odot}) > 9.3$	1031
Low mass limit	$\log(M_{bar}/M_{\odot}) > 9$	1218
No mass limit	$\log(M_{bar}/M_{\odot}) > 8.5$	1297

Table 3.1: The subsamples and mass limits used to evaluate filaments in SIMBA

determine if the filament finding procedure was successful.

3.4 Using SIMBA simulations to test DisPerSE

Previous studies using DisPerSE typically use large data sets, of the order $\approx$ 10, 000 galaxies (for example, Kleiner et al. (2016); Laigle et al. (2017); Luber et al. (2019)). Because RESOLVE has a much lower number of galaxies ($\sim$ 1000), the reliability of filaments extracted using DisPerSE had to be tested using simulation data. In this case, data from the SIMBA simulations are used to ensure that DisPerSE will extract reliable filaments in smaller samples.

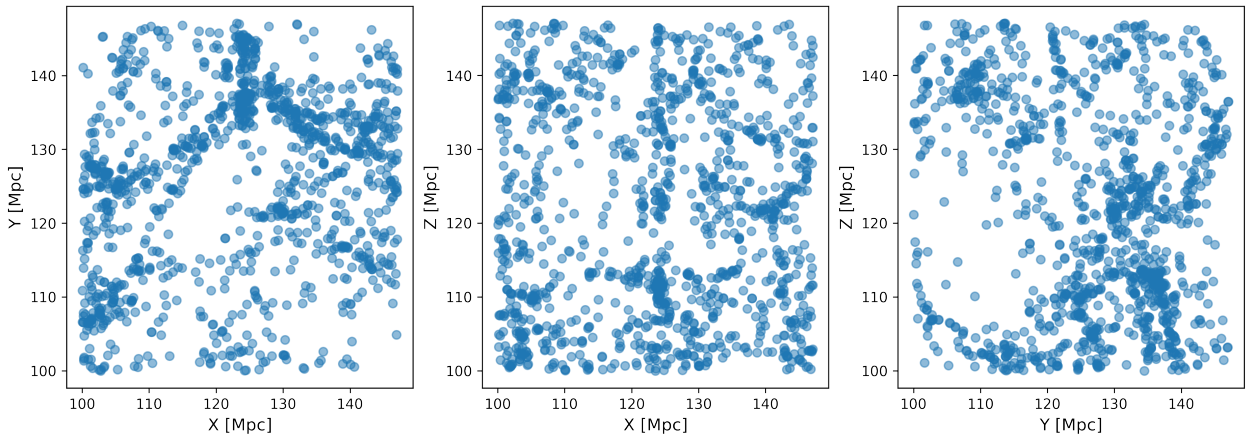

Figure 3.7: The left panel shows the XY projection of galaxies in the SIMBA 25 000 Mpc^3 box. The middle panel shows the XZ projection and the right panel shows the YZ projection

To select a volume that is comparable to RESOLVE, I used Snapshot m100n1024 _151 from the s50j7k model of the simulation. This corresponds to a 100 $\times$ 100 $\times$ 100 Mpc^3 box at z = 0.

Because RESOLVE is approximately 25 000 Mpc^3, a 50 $\times$ 50 $\times$ 50 Mpc^3 section of the box was selected and visually inspected to ensure that the distribution of galaxies approximately matched RESOLVE-A in structure (i.e. that there were no massive clusters and it contained at least one larger group). The XY, YZ, and XY projections of the selection are shown in Figure 3.7.

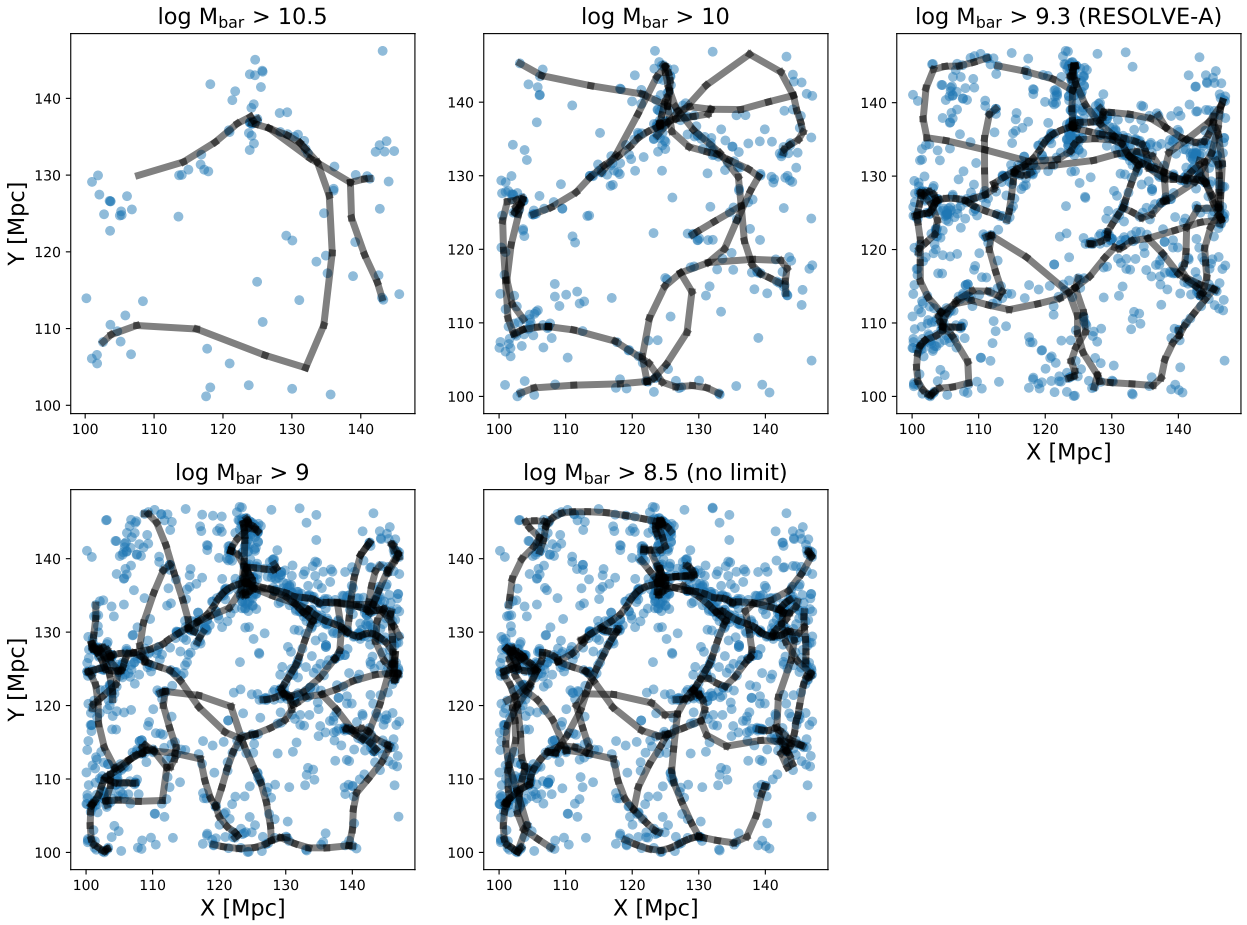

Figure 3.8: This figure shows the XY projection of the filaments and galaxies in each SIMBA subsample. Blue dots represent the simulated galaxies and the black lines represent the filament segments.

I then applied various baryonic mass cuts on the simulated galaxies, including the log($M_{bar}/M_{\odot}$) > 9.3) limit used for the RESOLVE-A data. The limits and number of galaxies in each subsample are shown in Table 3.1. As shown in Figures 3.8 and 3.9, increasing the mass limit reduces the number of galaxies in the distribution and thus affects how DisPerSE will extract filaments.

I used DisPerSE to determine the Delaunay tessellation with a smooth boundary condition and extracted the filaments using the procedure described in Section 3.3. The filaments and subsamples are presented in Figures 3.8 and 3.9. Galaxies are shown in blue and the filament segments extracted using DisPerSE are represented by black lines.

The filaments extracted by DisPerSE vary significantly depending on the mass limit used. In the sample with the highest mass limit, DisPerSE finds some filaments that are consistent with prominent filaments in the more complete samples, but also produces at least one filament that is not seen in any of the more complete samples. At the intermediate mass limit, DisPerSE performs poorly, but is able to extract more filaments than the high mass

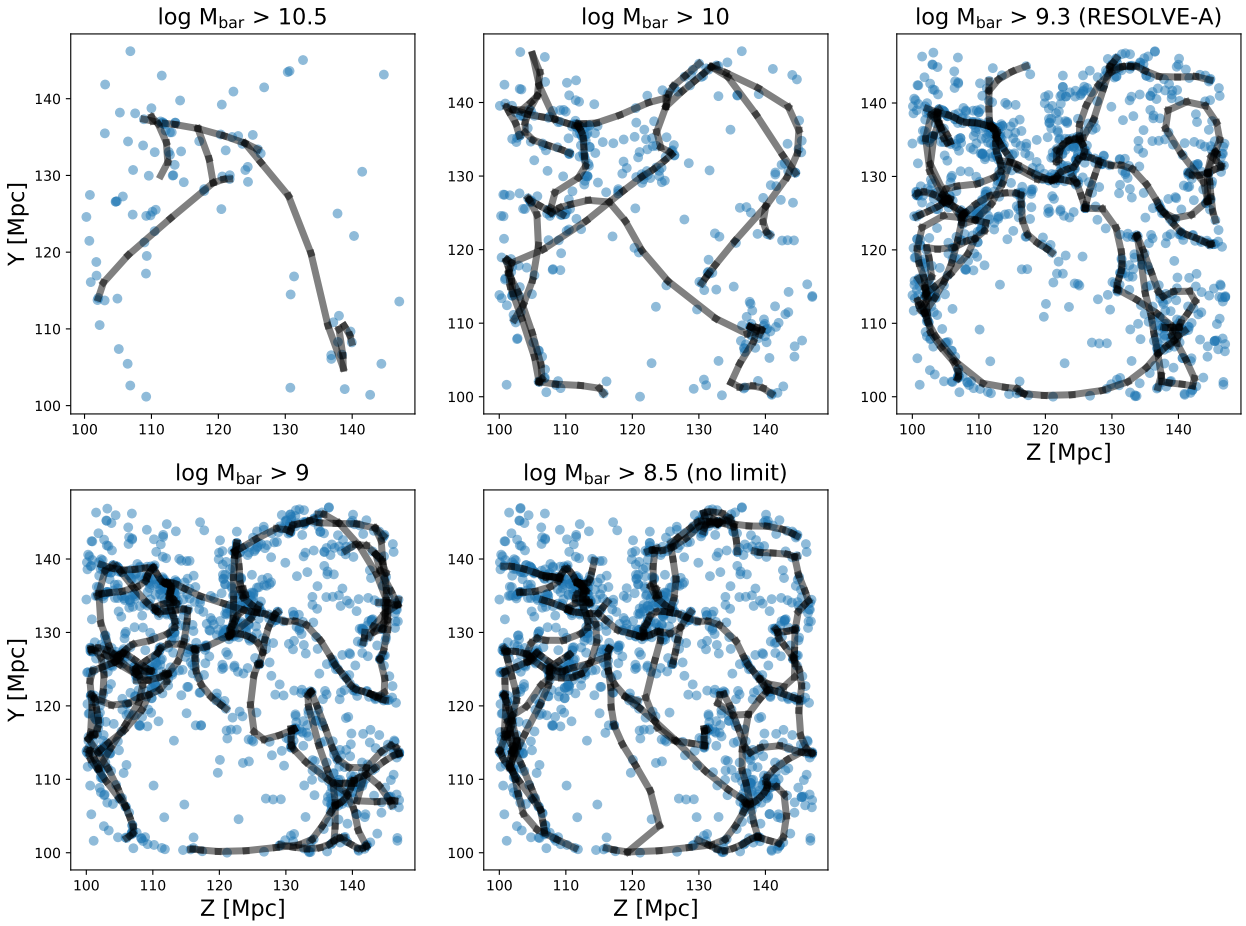

Figure 3.9: This figure shows the ZY projection of the filaments and galaxies in each SIMBA subsample. Blue dots represent the simulated galaxies and the black lines represent the filament segments.

sample.

At the limit of RESOLVE-A, the filaments are in good agreement with the filaments at lower mass limits. However, there are some differences in the filaments identified at the different mass limits, suggesting that some caution is required when analysing filaments when fewer galaxies are used, but that DisPerSE is generally reliable at this mass limit.

3.5 Data Preparation

3.5.1 Correcting for Redshift Space Distortions

Measuring galaxy coordinates in three dimensions poses several challenges. Although a galaxy's on-sky position may be measured accurately, obtaining the physical distance to a galaxy requires measurements based on the Tully-Fisher Relation, the Fundamental Plane or from standard candles. Because these types of measurements are often unavailable or costly to obtain, most surveys rely on redshift and recession velocity observations as a proxy for distance.

When working with recession velocity measurements, galaxies may have an additional velocity component, known as the peculiar velocity, from their distant-independent motion within a galaxy cluster or group. This leads to a stretching-out of the group of cluster known as the 'Fingers of God' effect. By eye, these redshift-space distortions can be easily mistaken for filaments. The total recession velocity (v_{tot}) of a galaxy is given by,

$$v_{tot} = H_0 \times D + v_{pec} \tag{3.1}$$

where D is the distance to the galaxy in Mpc, Hubble constant is H_0 and additional peculiar velocity component is v_{pec} due to motion within a group or cluster.

To correct for this effect, the RESOLVE group catalogue is used to assigned each galaxy in a group to the velocity of the central galaxy within the group. This effectively collapses the Fingers of God back into their respective groups. A comparison of the RESOLVE-A field before and after this correction is shown in Figure 3.10.

3.5.2 Converting to comoving coordinates

Although DisPerSE is capable of finding filaments directly from sky coordinates (Right Ascension (R.A.), Declination (Dec.) and redshift (z)), the internal transformation used for this process is poorly documented. For clarity and ease of calculation, I transformed the galaxy catalogue sky coordinates to comoving coordinates. Comoving coordinates are cosmological coordinates which account for the expansion of the universe and allow calculations of distance when working with redshift information. At low redshifts, like those in RESOLVE, the transformations are as follows:

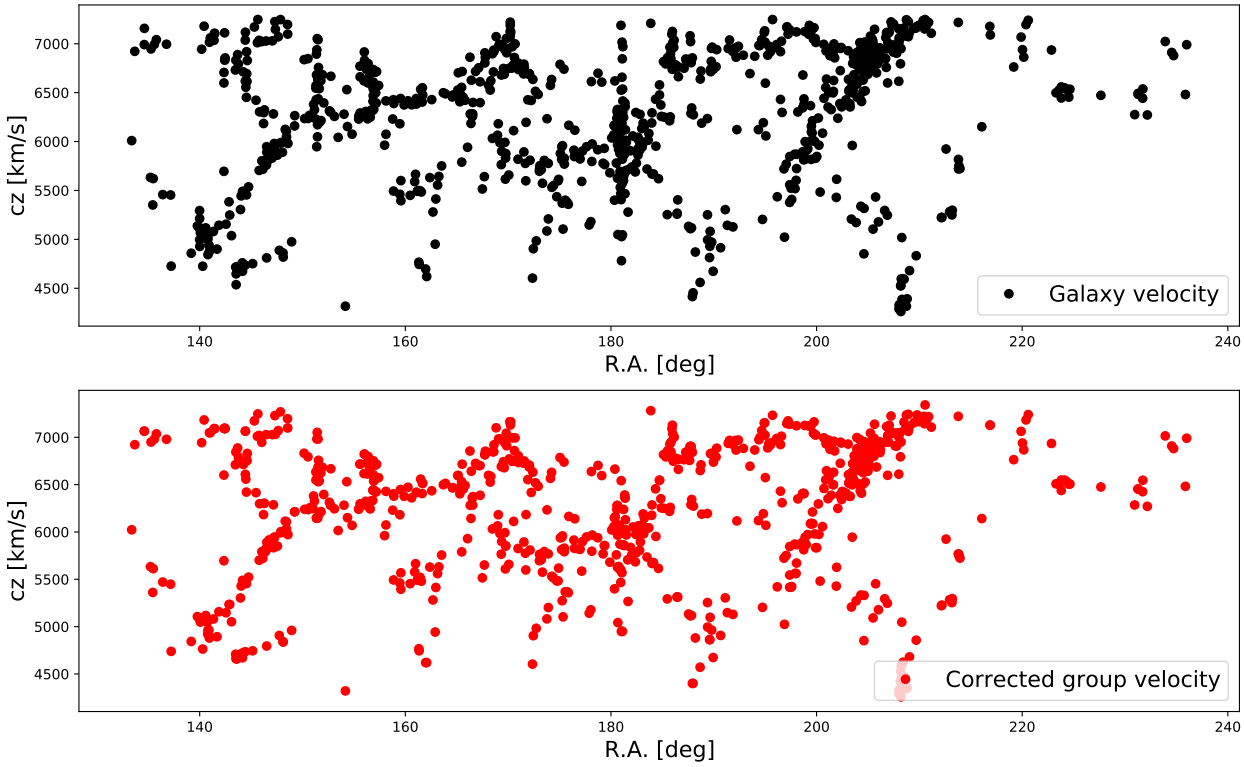

Figure 3.10: The upper panel shows the uncorrected distribution of galaxies in RESOLVE A in the R.A.-velocity plane. The lower panel shows the corrected distribution of galaxies after each group or cluster galaxy was assigned to its group velocity. Notably, the large, Finger of God structure at 180° < R.A. < 200° has been collapsed in the lower panel.

$$\begin{aligned} R &= cz[\mathrm{km/s}]/H_0[\mathrm{km/s/Mpc}] \\ X &= R\sin(90° - Dec)\cos(RA) \\ Y &= R\sin(90° - Dec)\sin(RA) \\ Z &= R\cos(90° - Dec) \end{aligned} \tag{3.2}$$

Under this transformation, the coordinates are presented as distances in Megaparsecs (Mpc) from the observer, the *X* coordinate corresponds most closely to *cz*, *Z* correspond most closely to the Dec and *Y* corresponds approximately to the RA.

3.6 Filament Finding in RESOLVE-A

Once the galaxy data were converted to comoving coordinates and formatted into the appropriate survey ascii format required by DisPerSE, I used the `delaunay_3d` function in DisPerSE to run the Delaunay Tessellation Field Estimator with a smooth boundary condition in 3D, as described in Section 3.3. The filaments were extracted using the Morse-Smale Complex, applying a 3 σ and 5 σ persistence threshold for comparison. Figure 3.11 shows

that the filaments extracted at both thresholds overlap. However, the 3 σ cut produces several, additional filaments which are not as robust as the 5 σ filaments. The 5σ cut is used in the rest of this dissertation to ensure that the most robust filaments are selected.

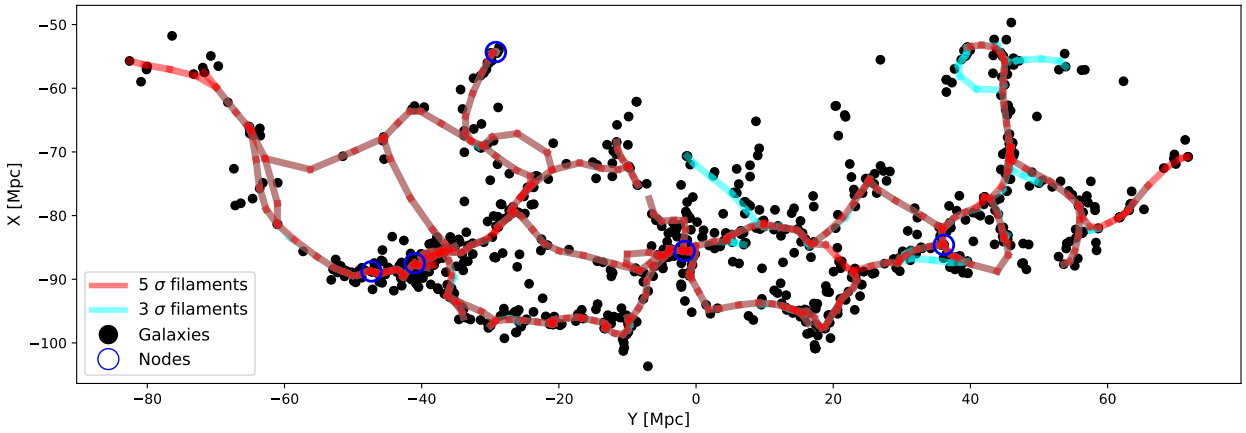

Figure 3.11: The galaxy distribution is shown in black points. Filaments extracted using the 3σ persistence threshold are shown in transparent cyan. The filaments extracted with a 5σ persistence threshold are shown in transparent, bright red. Dark red lines indicate where the filaments found with the two thresholds overlap. They are in overall agreement with each other. However, there are filaments which are removed when the 5σ threshold is applied.

The filaments were visually inspected in Paraview to ensure that the filaments traced the galaxy distribution in all three dimensions. Figure 3.12 shows a 3D view of the Delaunay tessellation estimated by DisPerSE with the filaments found using the Morse-Smale Complex overlaid, visualised in Paraview. This illustrates how the filaments are mapped according to the density field. Additionally, Figure 3.13 shows that the filaments trace the galaxy distribution in 3D.

3.7 Comparing the filaments found using different boundary conditions

The different boundary conditions available in DisPerSE are compared in Figure 3.14. The top panel shows the filaments found when the fiducial smooth boundary condition is applied. The filament segments connect to each other and the nodes lie in the high density regions. This boundary condition produces the most filament segments and the fewest number of nodes.

When the periodic boundary is applied, as shown in the second panel, the filaments show some discontinuities. Additionally, this boundary produces nodes which lie at different locations to the smooth boundary condition.

The mirror boundary condition, shown in the third panel, produces filaments which closely resemble the filaments produced by the smooth boundary condition. These filaments are

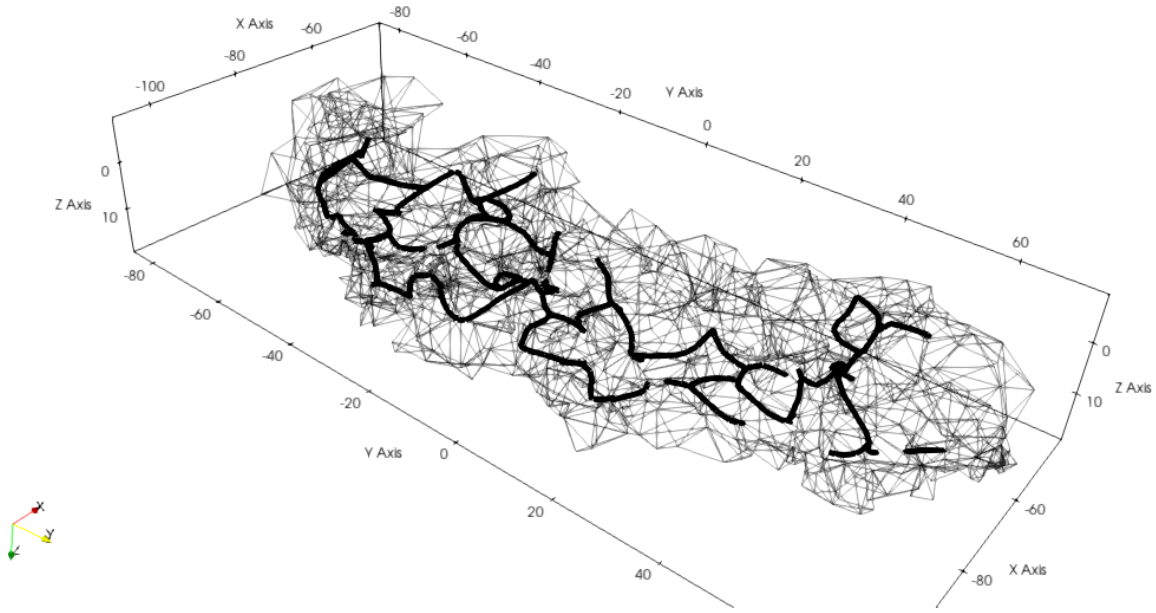

Figure 3.12: The Delaunay tessellation estimated by DisPerSE calculated for the RESOLVE A field with a smooth boundary. The solid lines show the filaments extracted based on this Delaunay tessellation.

well-connected. However, as with the periodic boundary condition, the nodes do not lie at the same locations as the nodes found with the smooth boundary condition. Additionally, this boundary condition produces fewer filament segments.

The void boundary condition, as shown in the last panel, produces filaments that trace the galaxy distribution well. However, the nodes produced by this boundary condition do not match the nodes found with the smooth boundary condition.

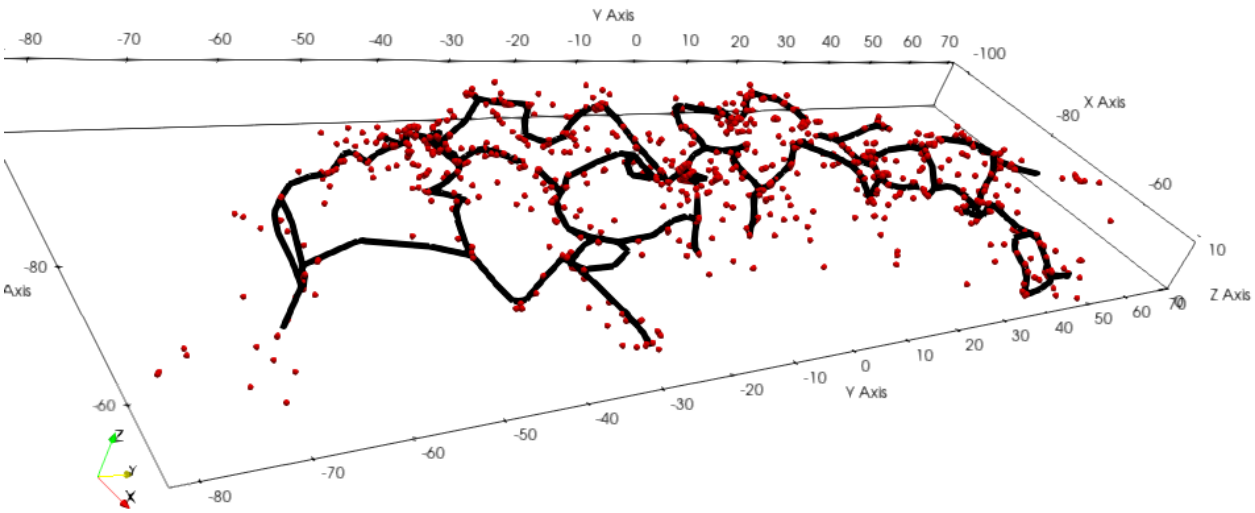

Figure 3.13: A 3D view of the 5σ filaments in black lines extracted using DisPerSE and the galaxy distribution as red spheres.

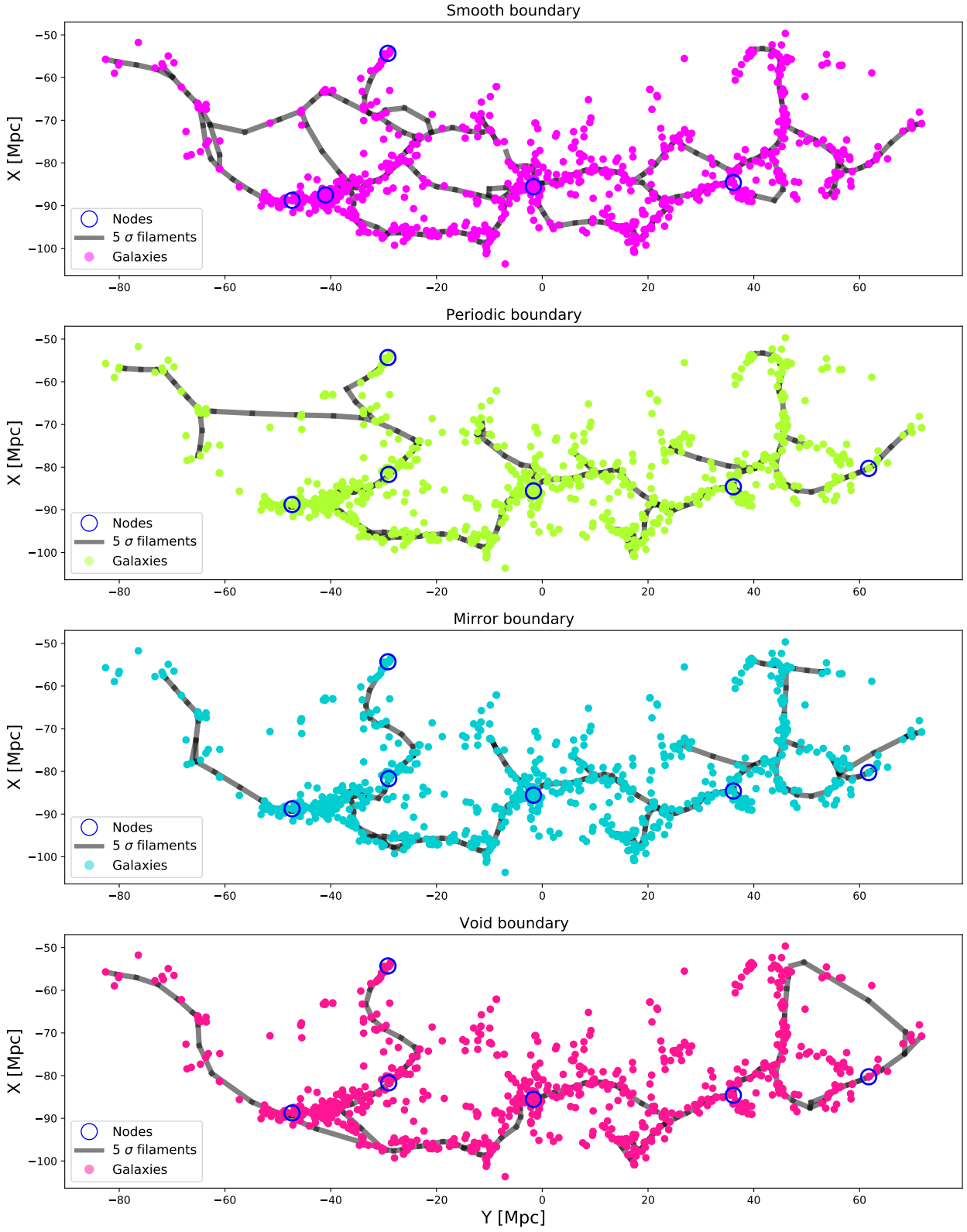

Figure 3.14: The filaments extracted when different boundary conditions are compared. The smooth boundary condition, which is the fiducial boundary condition, is shown in the top panel. The periodic boundary condition is shown in the second panel, followed by the mirror boundary condition in the third panel. The lower panel shows the void boundary condition. Nodes are represented by dark blue open circles. The grey lines represent the 5 σ filaments. The galaxy distribution is shown by coloured circles.

Overall, the filaments generally match, regardless of boundary conditions. Although the smooth boundary does produce a higher number of filaments than the other boundary conditions, these additional filament segments do not contain many galaxies and thus would not have a significant effect on the results. Additionally, the smooth boundary condition is the only boundary condition which places nodes near the centre of the large galaxy group located in the lower left of the galaxy distribution. Due to the strong recommendation to use the smooth boundary condition for observational data by the DisPerSE manual (Sousbie, 2013), this boundary condition is used in this project.

3.8 Calculating the Distance to filaments

When studying the effect of filaments on galaxy evolution, one of the most important parameters is the distance from a galaxy to the nearest filament. For studies that use DisPerSE, this is measured as the distance to the nearest critical point, D_{cp} (for e.g. Luber et al.; Blue Bird et al.), or the perpendicular distance to the nearest filament segment or 'skeleton', (D_{skel}) (see Kraljic et al.). These metrics are illustrated in the diagram in Figure 3.15.

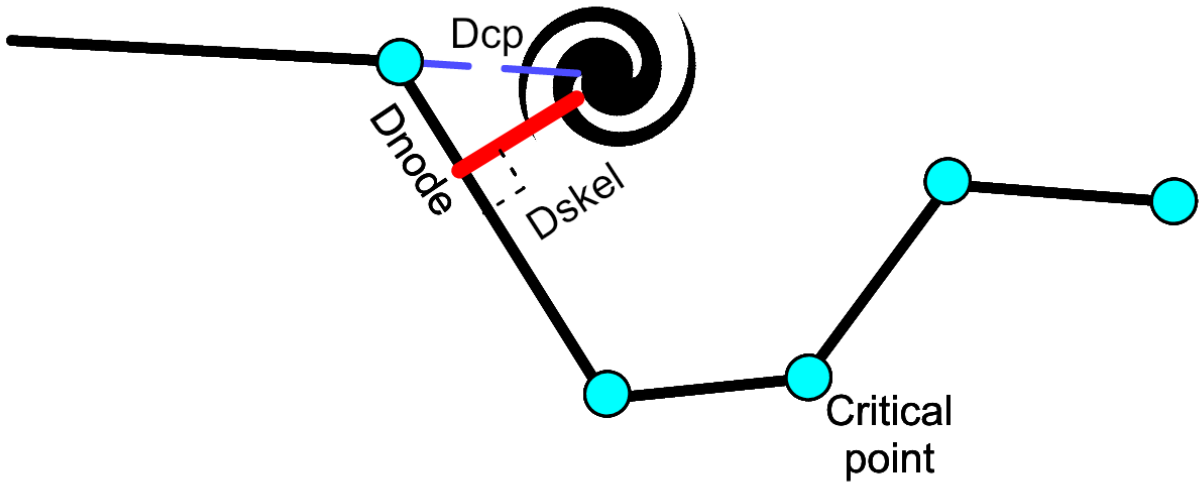

Figure 3.15: This diagram shows the difference between the D_{cp}, parameter (dashed, blue line), which shows the distance to the nearest critical point, and the D_{skel}(red, solid line), which measures the perpendicular distance to the nearest filament segment. The critical points are marked with cyan circles and the filament segments are represented by the solid black lines.

The distance between each filament segment and is calculated using standard 3D vector calculus to find the nearest filament for each galaxy.

For comparison, the distance to the nearest critical point for each galaxy is also calculated. This comparison is shown in the histogram in Figure 3.16. The distances estimated with D_{skel} are smaller than the distances calculated with D_{cp}, which is expected because galaxies

situated near the midpoint of a filament segment may have shorter distances to the nearest filament segment, compared to the nearest critical point, which are found at the ends of filament segments.

Although both parameters show a similar distribution, the D_{skel} parameter more accurately describes the physical distance from a filament to a galaxy and is more commonly used in the literature. However, this method is more computationally expensive to calculate and is difficult to optimise, unlike D_{cp}, which can easily be optimised for large samples using techniques like KD-trees. The distance to critical point is calculated to compare my results to other works in the literature.

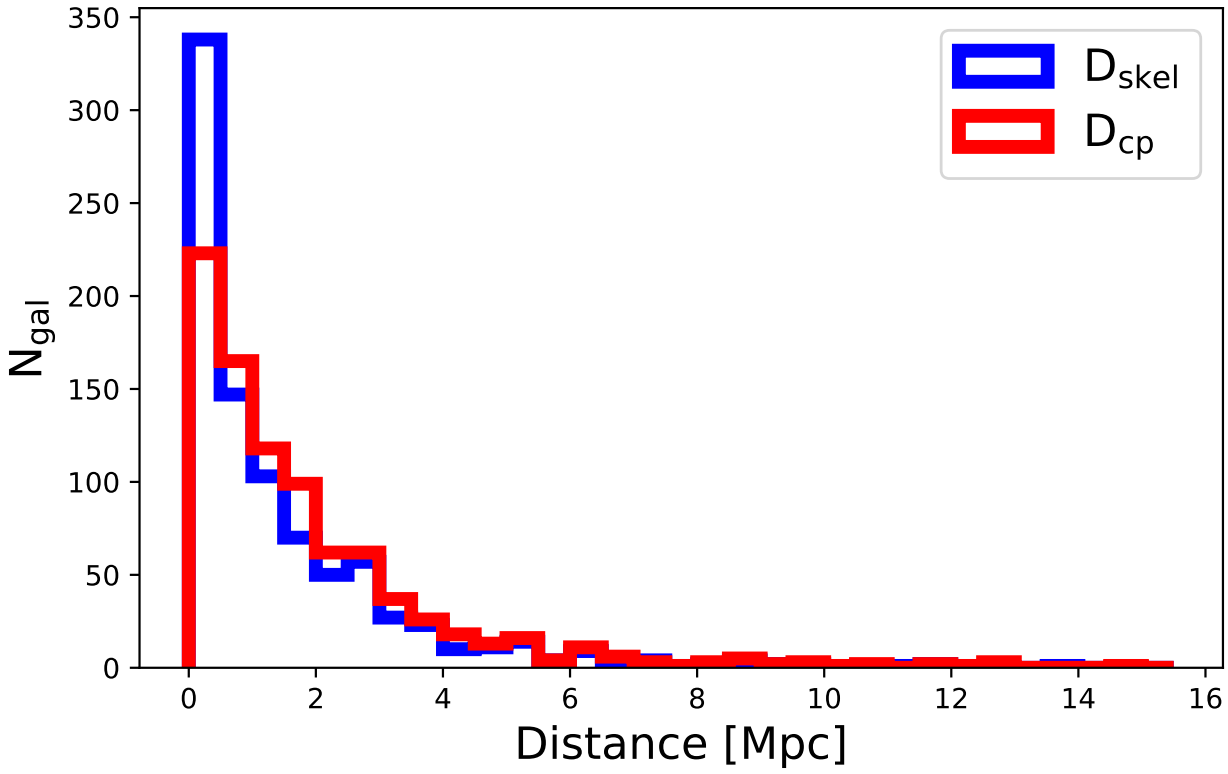

Figure 3.16: Histogram showing the distances calculated using D_{skel} vs D_{cp},. The distances estimated with the D_{skel} parameter are lower than the distances calculated with the D_{cp}, parameter.

Chapter 4

Results and Analysis

The previous chapter demonstrated that DisPerSE is a reliable tool for extracting filaments from an observational data set. This chapter will present the results of the filament identification in RESOLVE-A and the analysis of the galaxy properties with respect to distance to filament. Lastly, I will examine the role of groups in driving trends.

4.1 The effect of filaments on galaxy properties

Since the focus of this dissertation is how filaments affect galaxy evolution - specifically, the gas properties of galaxies - this analysis will examine how the median stellar mass, *u*-*r* colour and gas fraction change with distance to filament.

The galaxies in RESOLVE-A are concentrated close to the filaments. Figure 4.1 shows the filaments in RESOLVE-A. Galaxies are colour-coded by the mass of their host dark matter halo. Although DisPerSE does not receive any input indicating the halo masses, high mass halos are found at the intersection of filaments and correspond to the nodes, which represent the maxima of the underlying density field. This is consistent with the predictions of large scale structure models (Cautun et al., 2014).

To examine trends with distance to filament and achieve robust statistics across the range of distances, the galaxies are sorted by distance and divided into bins with an equal number of galaxies in each bin throughout this analysis. Although this results in bin edges that do not correspond to the typical sizes of physical structures, such as the radius of a group or filament, it ensures that observed trends are independent of the fluctuating number of galaxies at each scale. In each distance bin, the median value of the binned values, along with the number-weighted bin center, are calculated. Bootstrapping [1] (1000 iterations with replacement) is used to determine the 1σ confidence interval for each bin median. Additionally, the Spearman's rank test [2] is applied to the median galaxy properties and binned distance to filament to determine the strength of the trends and statistical significance. Be-

[1] `astropy` implementation at https://docs.astropy.org/en/stable/api/astropy.stats.bootstrap.html
[2] `scipy` implementation at https://docs.scipy.org/doc/scipy/reference/generated/scipy.stats.spearmanr.html

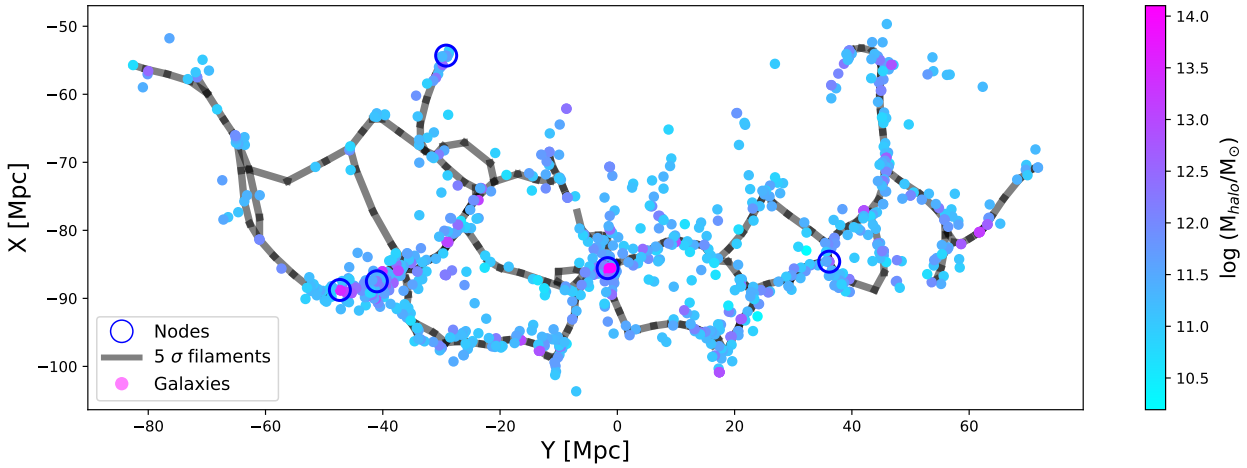

Figure 4.1: The YX projection of filaments and galaxies in RESOLVE-A. Black lines represent filament segments identified by DisPerSE. Open, blue circles show the location of nodes. Galaxies are colour coded by the mass of their host dark matter halos.

cause each trend is represented by a small number of bins, the significance is assessed by comparing the correlation coefficient r_s to the critical values of the Spearman's rank test for *n* number of bins, such that the trend is considered significant if $|r_s| \geq$ critical value at the α = 0.1 level (see Appendix B).

4.1.1 Stellar mass

Because most galaxy properties depend on stellar mass, it is important to analyse how stellar mass is affected by filaments. RESOLVE includes galaxies across a range of stellar masses, but notably probes galaxies at very low stellar masses as shown in the histogram in Figure 4.2. This histogram shows the mean (mean $\log\ (\mathrm{M}_\star/\mathrm{M}_\odot)$ = 9.74) and median (median $\log\ (\mathrm{M}_\star/\mathrm{M}_\odot)$ = 9.45) stellar mass values for the entire sample, as well as lines indicating the gas-richness threshold and bimodality threshold, which divide the sample into low, intermediate and high mass subsamples (see subsection 4.1.2).

Figure 4.3 shows the location of galaxies with respect to the filaments, colour-coded by their log stellar mass. Although there are some high mass galaxies far away from the filaments, the filaments are mostly made up of high stellar mass galaxies. This is reflected in Figure 4.4, which shows the median stellar mass vs distance to filament. In this figure, the median stellar mass of galaxies decreases as distance from filament increases. For distances with $\mathrm{D}_{\mathrm{skel}}$< 1.5 Mpc, the median decreases by $\sim$ 0.5 dex and this trend is statistically significant (see Table 4.1). However, beyond 1.5 Mpc, this trend flattens out. This indicates that galaxies within a typical filament radius have higher stellar masses than galaxies outside of filaments.

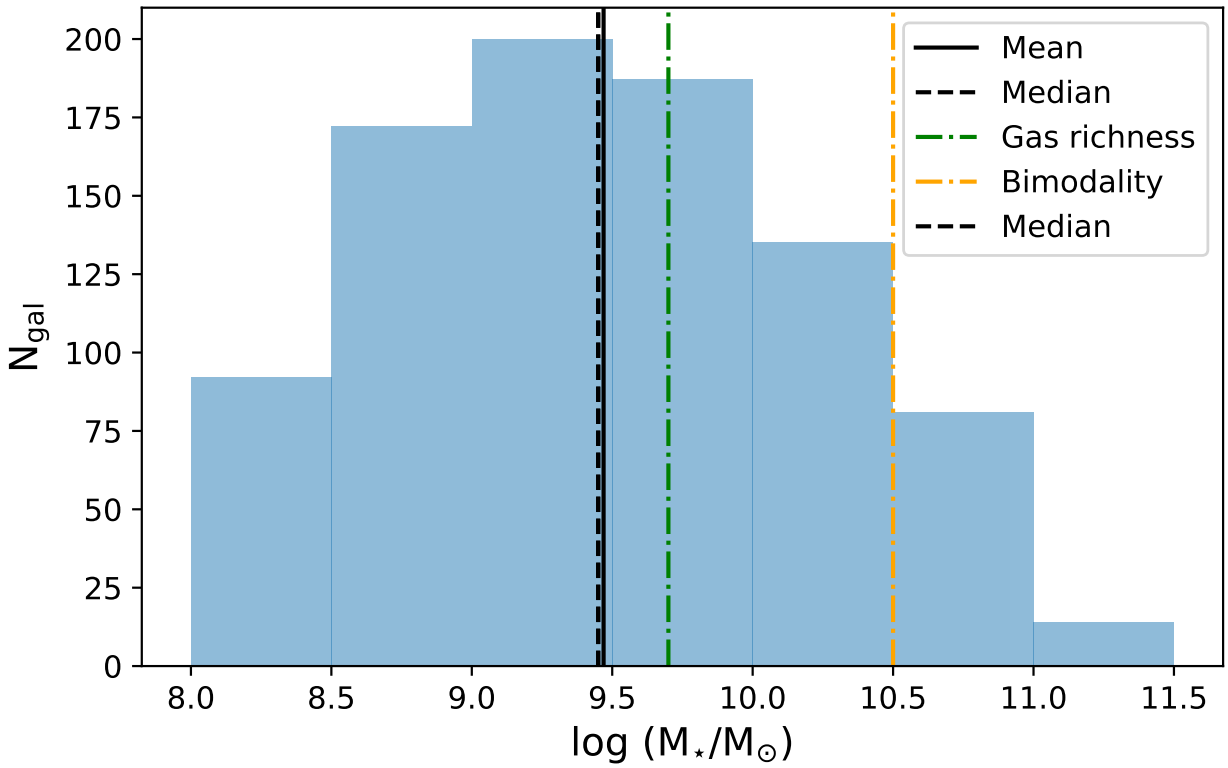

Figure 4.2: Histogram showing the number of galaxies in RESOLVE-A in stellar mass (log ($M_\star$/ $M_\odot$)) bins of 0.5 dex. The mean stellar mass and median stellar mass are represented by solid and dashed black lines respectively. The gas-richness and bimodality thresholds are indicated by the green and orange lines.

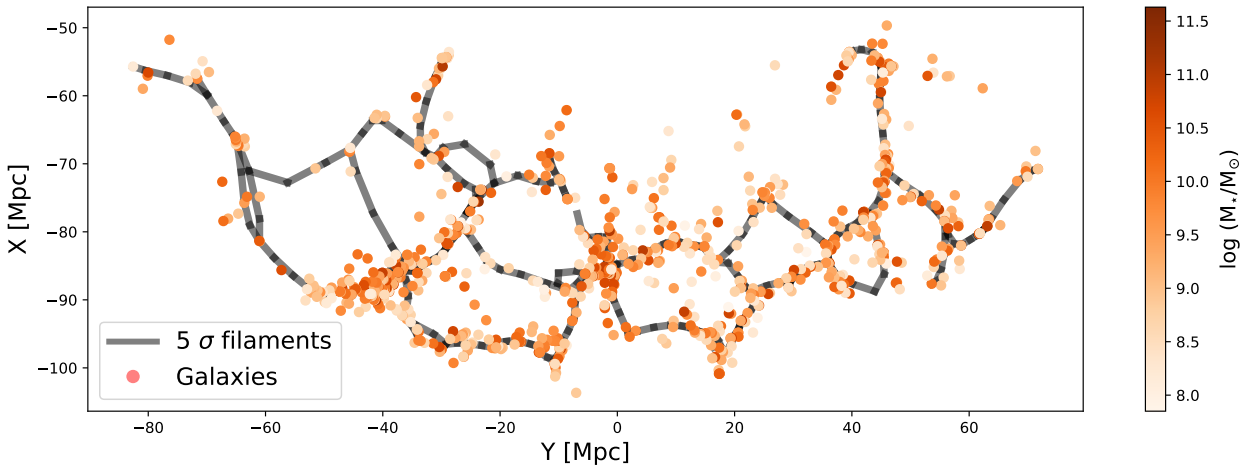

Figure 4.3: The YX projection of filaments in RESOLVE-A, overlaid with galaxies colour coded by their stellar mass. Darker colours indicate more massive galaxies.

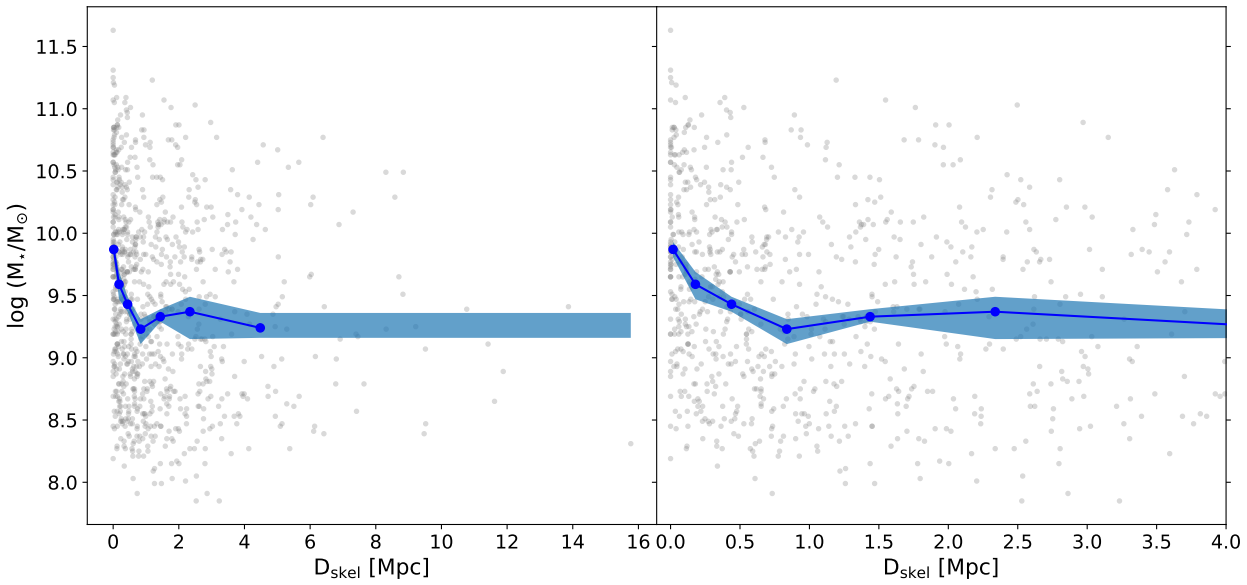

Figure 4.4: The median stellar mass vs distance to filament (D_{skel}) is shown in blue. Individual galaxies are shown in grey. The coloured band indicates the 1σ error on the median in each bin. The right panel shows this distribution for 0 Mpc < D_{skel} < 4 Mpc to highlight the behaviour close to the filaments. The median stellar mass increases by $\sim$ 0.5 dex for D_{skel} < 1.5 Mpc.

Table 4.1: Spearman's Rank Test properties for stellar mass vs distance to filament for galaxies, by mass, as shown in Figure 4.4.

Measurement	N_{bins}	N_{dof}	Critical value for N_{dof}	r_s	Significant
log ($M_\star/M_\odot$) (D_{skel}< 1.5 Mpc)	5	3	0.9	-0.9	Yes
log ($M_\star/M_\odot$)	7	5	0.714	-0.75	Yes

4.1.2 Colour

Galaxy colour (in this case, the *u-r* colour) is an indicator of star-formation and quenching, dust content and stellar age (Mo et al., 2010). In terms of environment, the fraction of red galaxies is typically higher in dense regions than in low-density regions. Figure 4.5 shows the distribution of galaxy colour with respect to the filaments. Galaxies in the high density regions, close to the nodes, of this map are typically red compared to galaxies spread across the filaments.

Kannappan et al. (2013) connected two observed scales in galaxy properties, the gas-richness threshold (log $(M_\star/M_\odot)$ < 9.7) and bi-modality threshold (log $(M_\star/M_\odot)$ > 10.5) to gas refuelling regimes. Below the gas-richness threshold, originally defined by Dekel & Silk (1986), gas-dominated, quasi-bulgeless galaxies are most common and are refuelled by accretion mechanisms. Galaxies above the bi-modality threshold (Kauffmann et al., 2003) are typically gas-poor and are elliptical or S0 type galaxies, which fall within the quenched regime. Galaxies between these scales are "processing-dominated", where they use gas at approximately the same rate at which it is accreted. Because these scales segregate galaxies by

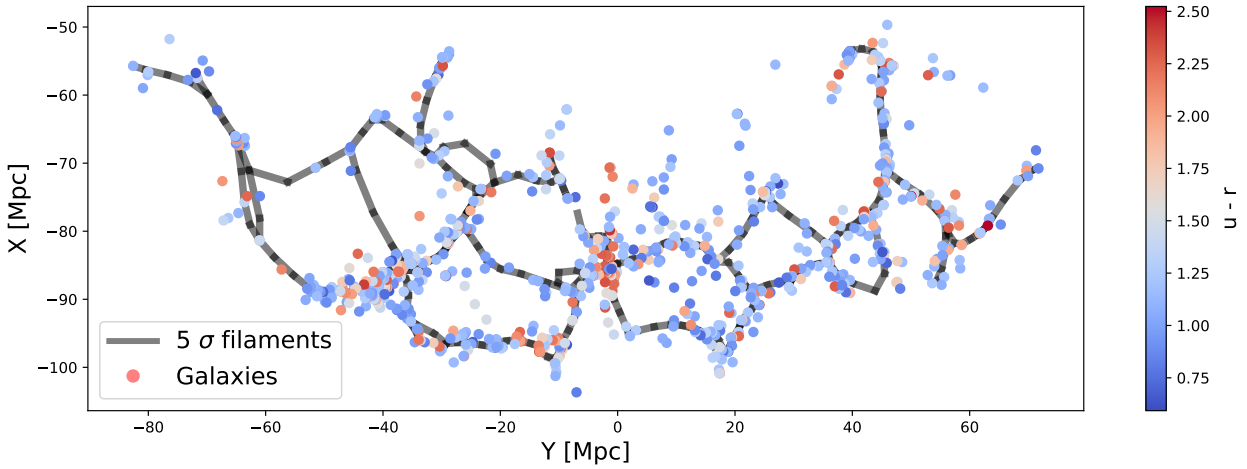

Figure 4.5: The YX projection of filaments in RESOLVE-A, showing the distribution of galaxies by their *u*-*r* colour.

type and are connected to gas refuelling, they are useful for ensuring that observed effects on colour and gas fraction are due to environmental effects rather than inherent to the galaxy type or stellar mass. Additionally, these mass scales are broad enough to contain a sizeable number of galaxies for calculating medians and determining trends. To control for the effect of stellar mass on colour, the sample is split into a low mass subsample (below the gas-richness threshold), an intermediate mass subsample and a high-mass subsample (above the bi-modality threshold).

The colour-magnitude diagram, shown in Figure 2.2, features a prominent 'blue cloud' of star-forming galaxies and a smaller red sequence, separated by a less populous 'green valley'. This is reflected in the histograms shown in Figure 4.6. Galaxies in the low-mass subsample are the most numerous and are bluer in colour than the high and intermediate mass subsample. The intermediate mass samples, which consists of galaxies of various morphological types, is redder than the the low mass subsample and is bluer than the high mass subsample. Galaxies in the high mass subsample are the reddest of the all the categories, which is typical for this mass range.

The median *u*-*r* colour vs distance to filament in each of these mass bins are shown in Figure 4.7. The overall increase in median colour with increasing mass is expected from the known relations between colour and stellar mass. In each subsample, the median colour decreases as distance to filament increases (i.e. galaxies close to filaments are redder than galaxies futher away). Due to the limited statistics, the trend is only statistically significant for the low mass bin (see Table 4.2).

4.1.3 Gas fraction

The effect of filaments on the gas content of galaxies is poorly understood in the literature. To examine this effect, the gas fraction - that is, the ratio of HI mass to stellar mass ($M_{HI}/M_{\star}$), is calculated. Figure 4.8 shows the gas fraction of galaxies distributed with respect to the

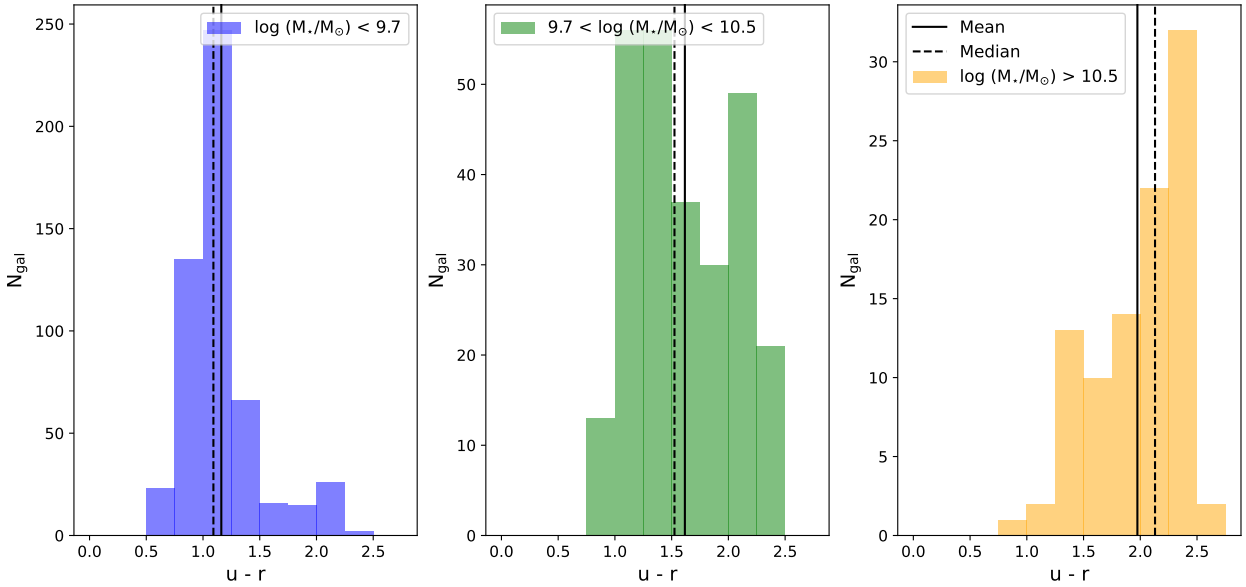

Figure 4.6: Histograms showing the distribution of *u-r* colour for galaxies in the low mass (blue), intermediate mass (green) and high mass (yellow) subsamples. The solid black lines indicate the mean colour in each subsample and the dashed lines indicate the median.

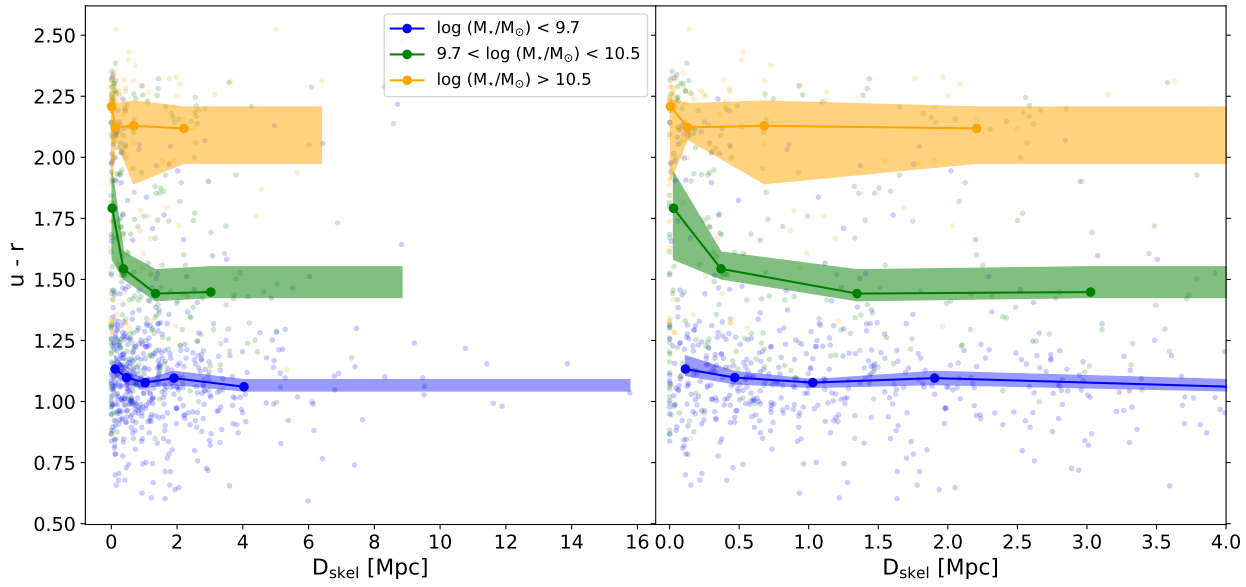

Figure 4.7: The median u-r colour vs distance to filament (D_{skel}[Mpc]) is shown in bins of stellar mass. The median for low mass galaxies is shown in blue, while high mass galaxies are shown in yellow. The coloured bands indicate the 1σ error on the median. The right-hand panel shows this distribution for 0 Mpc < D_{skel}< 4 Mpc to highlight the behaviour close to the filaments

Table 4.2: Spearman's Rank Test properties for *u* - *r* colour vs distance to filament for galaxies, by mass, as shown in Figure 4.7.

Measurement	N_{bins}	N_{dof}	Critical value for N_{dof}	r_s	Significant
u - *r* colour - low mass	5	3	0.9	-0.9	Yes
u - *r* colour - intermediate mass	4	2	1	-0.8	No
u - *r* colour - high mass	4	2	1	-0.8	No

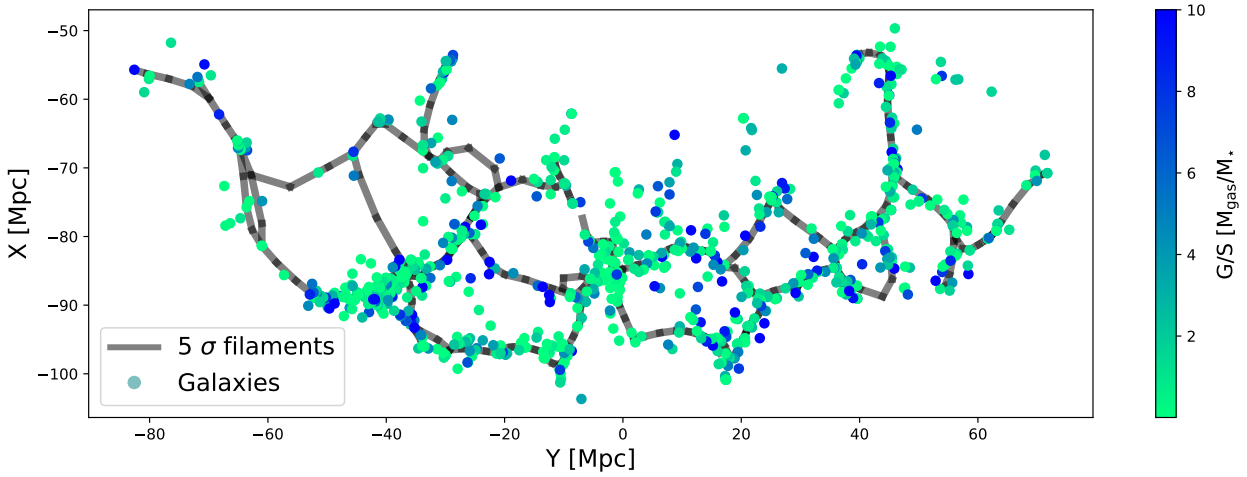

Figure 4.8: The YX projection of filaments in RESOLVE-A, overlaid with galaxies colour coded by their gas fraction. Darker colours indicate galaxies with higher gas fractions, while lower gas-fraction galaxies are shown in the brighter colours.

filaments. Galaxies with lower gas fractions are concentrated at high-density regions. The data are divided into the same mass bins as in subsection 4.1.2 to remove any mass dependence. These mass bins also correspond to the accretion-dominated ($\log\ (M_\star/M_\odot)$ < 9.7), process-dominated (9.7 < $\log\ (M_\star/M_\odot)$ < 10.5) and quenching ($\log\ (M_\star/M_\odot)$ > 10.5) refuelling regimes described in Kannappan et al. (2013). Histograms showing the gas fraction in each mass bin are shown in Figure 4.9. This shows that the low-mass subsample has the largest spread in gas fraction and is represented by a larger x-axis in the figure, with values ranging from 0 to several galaxies with G/S > 8, while the intermediate and high mass subsamples have narrow distributions with gas fractions ranging 0 < G/S < 2. Note that while the majority of gas fraction measurements are calculated using direct HI detections, upper limit estimates and photometric gas fraction estimates are treated as measurements in this work. Section 2.1.1 describes this choice and provides the frequency of each gas fraction type within each mass bin.

To understand whether filaments affect the gas content of galaxies, the median gas fraction vs distance to filament is calculated in each mass bin, as shown in Figure 4.10. This figure shows that the median gas fraction increases for low mass galaxies as distance to filament increases. This trend is statistically significant, as shown in Table 4.3. The low mass subsample contains two galaxies with extremely high gas fractions ($M_{HI}/M_\star$ > 30). These galaxies were checked to confirm the validity of the gas fractions. These galaxies have reliable stellar

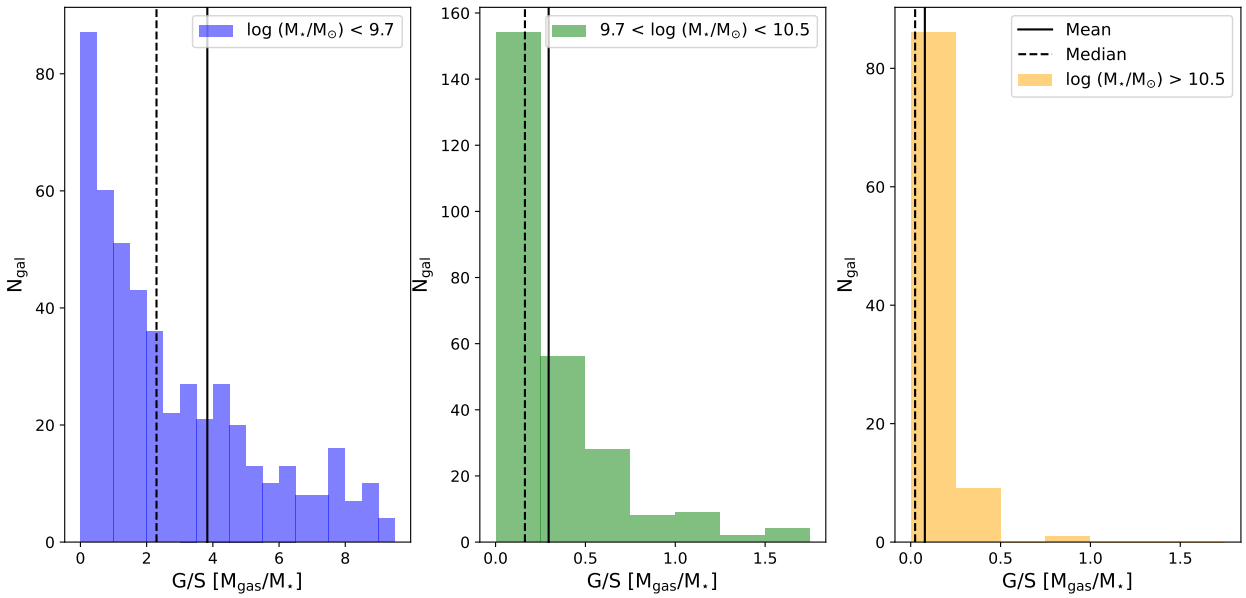

Figure 4.9: Histograms showing the distribution of gas fraction for galaxies in the low mass (blue), intermediate mass (green) and high mass (yellow) subsamples. The solid black lines indicate the mean gas fraction in each subsample and the dashed lines indicate the median.

mass estimates and high signal-to-noise ALFALFA HI detections and are therefore kept in the sample. Additionally, because a baryonic mass limited sample is used (see Chapter 2), the sample contains low stellar mass galaxies which may have been excluded if a luminosity or stellar mass limited sample was used.

The gas fraction for high mass galaxies also increases as D_{skel}increases. However, this trend is not significant. For intermediate mass galaxies, there is no statistically significant trend in median gas fraction with distance to filament.

Table 4.3: Spearman's Rank Test properties for gas fraction, shown in Figure 4.10.

Measurement	N_{bins}	N_{dof}	Critical value for N_{dof}	r_s	Significant
G/S - low mass	5	3	0.9	0.9	Yes
G/S - intermediate mass	4	2	1	0.4	No
G/S - high mass	4	2	1	0.8	No

4.2 The effect of groups and filaments on galaxy properties

Galaxy groups have a significant effect on the evolution of galaxies. Large galaxy groups may occur at the high density nodes of the cosmic web, which also form the intersection of filaments. These high-density regions may introduce additional gradients and trends in galaxy properties, as demonstrated by Laigle et al. (2017). Pre-processing, where galaxies are quenched through strangulation or evaporation (Fujita, 2004), may occur in small groups that reside within filaments (Sarron et al., 2019). Along with galaxy-galaxy interactions, this

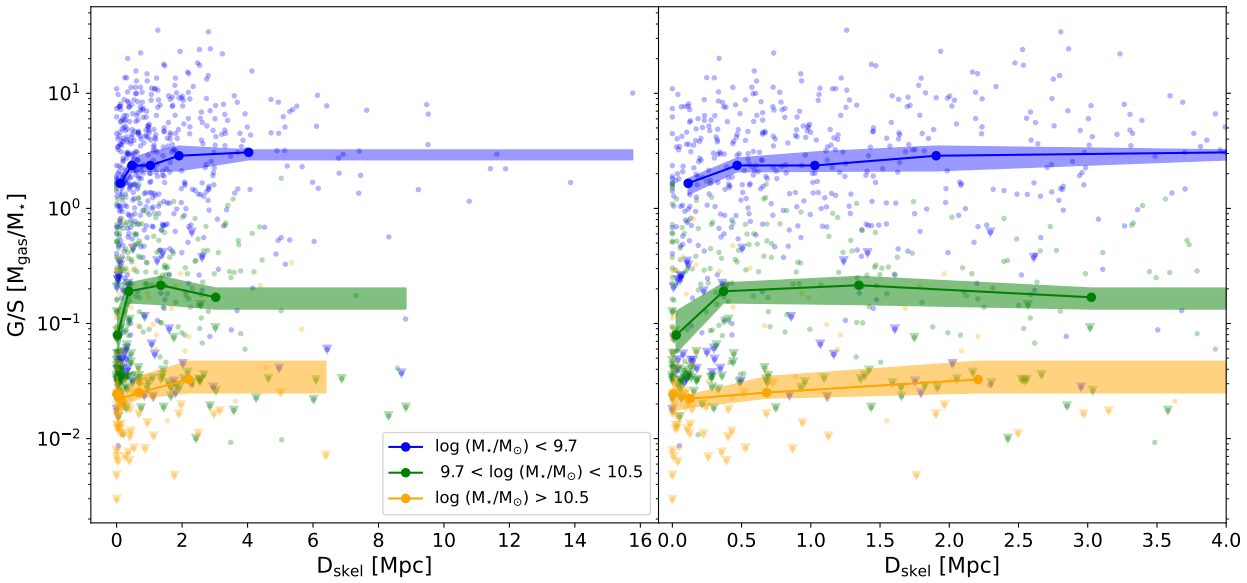

Figure 4.10: The median gas to stellar mass fraction vs distance to filament is shown in bins of stellar mass, as described in Figure 4.7. The gas fraction is represented on a log y-axis. Arrows indicate galaxies where upper limit estimates are used to determine the gas fraction. The right-hand panel shows this distribution for 0 Mpc < $D_{\rm skel}$< 4 Mpc to highlight the behaviour close to the filaments.

may alter the morphology, colour, stellar mass and gas content of galaxies in addition to the effect of the filaments themselves. To isolate the effect of filaments, galaxy groups must be carefully considered. Figure 4.11 shows the number of galaxies belonging to groups of different sizes in relation to their distance to filament. While most galaxy pairs are concentrated at $D_{\rm skel}$< 0.5 Mpc, several pairs can be found at larger distances. Small groups (3 $\leq$ $N_{\rm gal}\leq$ 5) are concentrated at $D_{\rm skel}$< 0.5 Mpc, although a few small groups may be found at larger distances. Large groups ($N_{\rm gal}$> 5) all occur within $D_{\rm skel}$< 4 Mpc

Many galaxy groups occur close to the filaments, at distances which trends in stellar mass, colour and gas fraction were observed in Section 4.1.

This section will consider the effect of filaments on galaxies' properties after the contributions due to groups are removed. Additionally, the HI deficiency of galaxies will be examined to provide a more detailed analysis of the gas properties of galaxies.

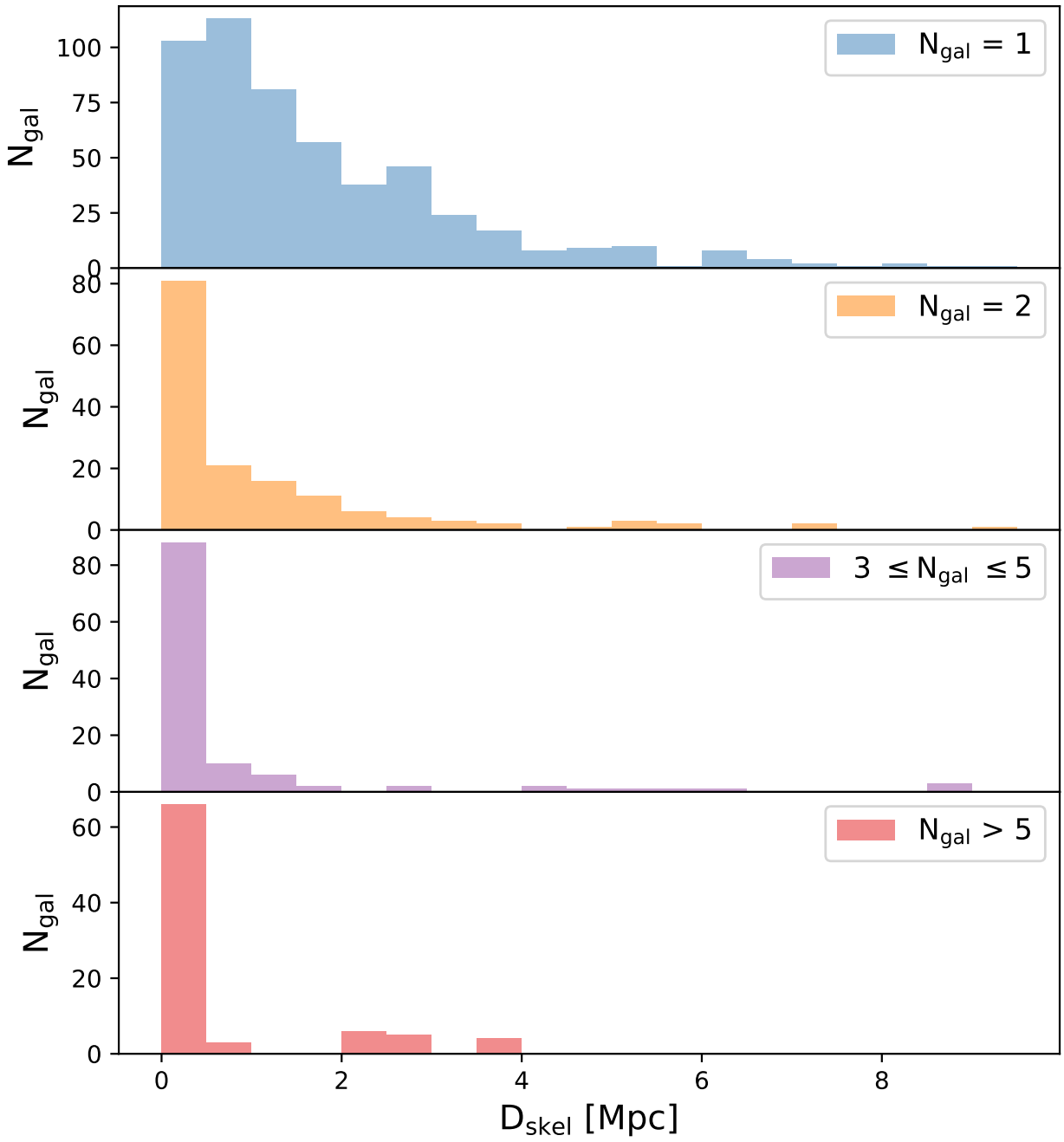

Figure 4.11: Histograms showing the number of galaxies of belonging to various group sizes in bins of distance to filament (D_{skel}[Mpc]). The top panel corresponds to single galaxies, the second panel shows galaxy pairs, the third panel shows small groups ($3 \leq N_{gal} \leq 5$), with the bottom panel showing large groups ($N_{gal} > 5$).

4.2.1 HI deficiency

The HI deficiency parameter is useful to examine the effect of filaments and groups on the gas content of galaxies. The HI deficiency compares the observed HI mass and the expected HI mass of a galaxy, based on observations of galaxies that are completely isolated and free of environmental effects (Haynes & Giovanelli, 1984). It is given by,

$$\mathrm{HI_{def}} = \log \mathrm{M_{HI}^{exp}} - \log \mathrm{M_{HI}^{obs}}, \tag{4.1}$$

where $\log \mathrm{M_{HI}^{exp}}$ is the expected HI mass determined using empirical relations and $\log \mathrm{M_{HI}^{obs}}$ is the observed HI mass. Positive values indicate that galaxies are more HI deficient, or gas-poor, than expected, while negative values indicate galaxies with an excess of HI gas. The relation from Bok et al. (2020), determined using isolated galaxies from the AMIGA project (Verdes-Montenegro et al., 2005), is used to determine the expected HI mass:

$$\log \mathrm{M_{HI}^{exp}} = 0.44 \times \log \mathrm{M_{\star}}/\mathrm{M_{\odot}} + 5.19, \tag{4.2}$$

where $\log \mathrm{M_{HI}^{exp}}$ is the expected HI mass and $\mathrm{M_{\star}}$ is the stellar mass of the galaxy. The range for 'normal' galaxies, as defined by Haynes & Giovanelli (1984), is -0.3 $\leq \mathrm{HI_{def}} \leq$ 0.3. Using this relation and the observed HI masses from the RESOLVE catalogue, histograms showing the HI deficiency for galaxies in groups of different sizes is shown in Figure 4.12. The histogram showing the HI deficiency for single galaxies peaks in the HI excess range, with a wide 'tail' extending to the HI deficient range. The histogram showing paired galaxies peaks within the 'normal' range for HI deficiencies. For galaxies in small groups, with 3 $\leq \mathrm{N_{gal}} \leq$ 5, the histogram features a peak within the normal range as well as a peak within the HI deficient range. The galaxies in large groups ($\mathrm{N_{gal}}$> 5) distribution peaks in the HI deficient range. As the number of galaxies per group increases, the peak of the histogram shifts from HI excess to HI deficiency, indicating that galaxy group size has an impact on the HI deficiency of galaxies.

To illustrate the contribution to the HI deficiency histograms from the direct detections compared to the non-detections, I overplot the histograms for the detections only in Figure 4.12. The distributions for single galaxies and pairs are largely unaffected since the majority of those samples are composed of galaxies which were directly detected in HI. For the group galaxies, there are very few directly detected HI deficient galaxies, and the HI deficient peaks are driven mainly by the HI non-detections. However, this is expected since upper limits represent the lowest detectable HI mass and HI deficient galaxies would not have enough HI gas to cross this limit.

Figure 4.13 shows the HI deficiencies for galaxies vs distance to filament. Each galaxy is colour coded by the size of its host group. Galaxies in large groups are more HI deficient and closer to filaments than single galaxies. However, there is some variation for small groups. Most single galaxies show an excess in HI.

For the remaining analysis, the sample is split into groups, where $\mathrm{N_{gal}} \geq 3$, and singles + pairs, where $\mathrm{N_{gal}} < 3$. Median properties are calculated as described in Section 4.1 for the remainder of this section.

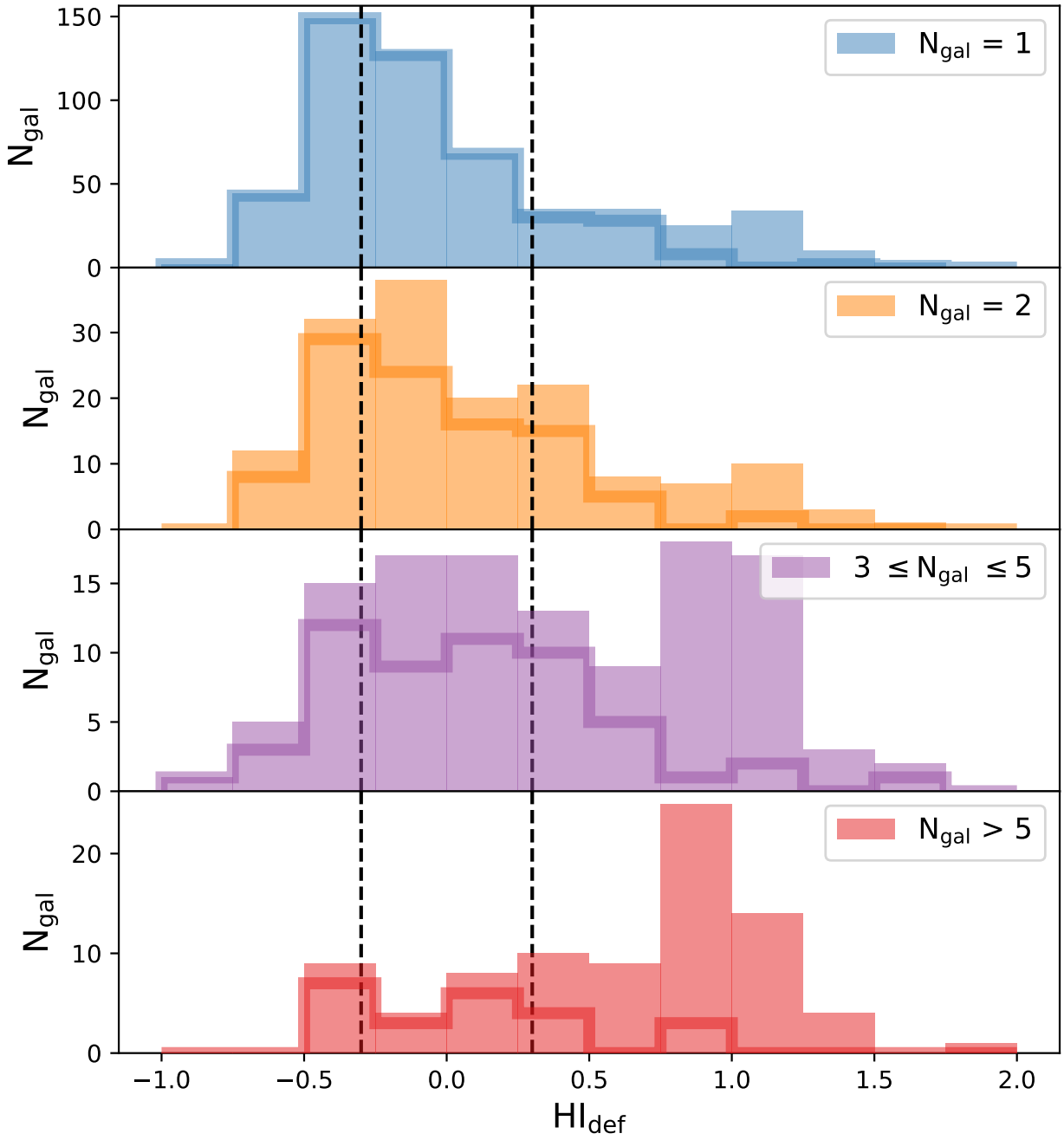

Figure 4.12: Histograms showing the number of galaxies belonging to groups of different sizes in bins of HI deficiency. Single galaxies are found in the top panel, with paired galaxies in the second panel, small galaxy groups ($3 \leq N_{gal} \leq 5$) in the third panel. The bottom panel shows galaxies in large groups (N_{gal}>5). Vertical lines indicate the 'normal' range for HI deficiencies (-0.3 $\leq HI_{def} \leq$ 0.3). Histograms showing the HI deficiency calculated using direct detections only are over-plotted in solid lines for each group size.

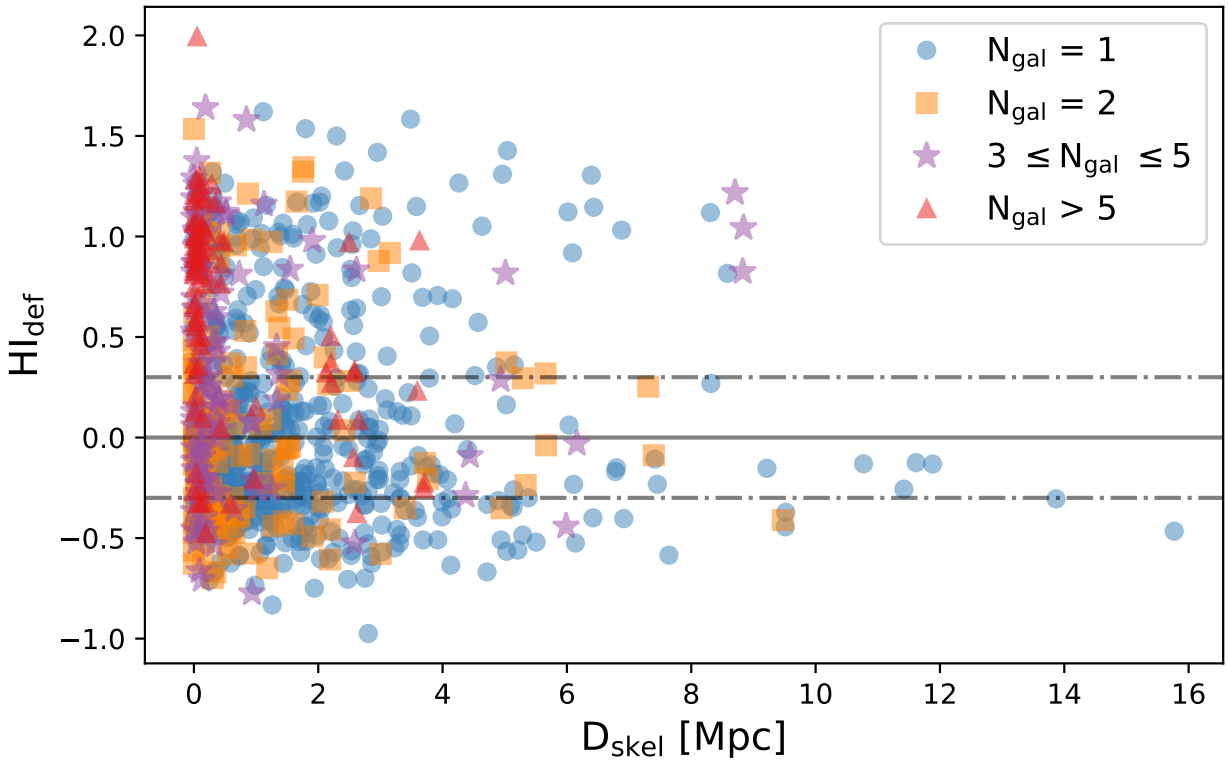

Figure 4.13: The HI deficiency vs distance to filament (D_{skel}) for galaxies. Red triangles represent galaxies which belong to groups containing more than 5 members. Purple stars represent galaxies belonging to groups containing 3-5 members. Orange squares represent galaxies in pairs and blue circles represent single galaxies. Points above the dot-dashed line indicate galaxies that are deficient in HI and galaxies below the solid line have an excess of HI. The range for 'normal' HI values ($HI_{def} \pm 0.3$) is indicated by the dot-dashed lines.

4.2.2 Stellar mass

Since the stellar mass trend with respect to distance to filament is one of the most prominent trends in this data and in the literature, it is worth examining if this trend may be driven by groups in addition to the filament environment. Figure 4.14 shows that the median stellar mass for galaxies in groups ($N_{gal} > 2$) is systematically higher than the median stellar mass for single + pairs. Although the decreasing trend in median stellar mass with increasing distance from filament for single + pairs is not statistically significant (see Table 4.4), the decreasing trend is stronger for single + paired galaxies than for group galaxies. This may suggest that the trend in Figure 4.4 is due to the filament environment rather than the group environment.

4.2.3 Colour

As shown in subsection 4.1.2, galaxies in RESOLVE-A are redder, on average, close to filaments than galaxies further away. However, as shown in Figure 4.11, there are several

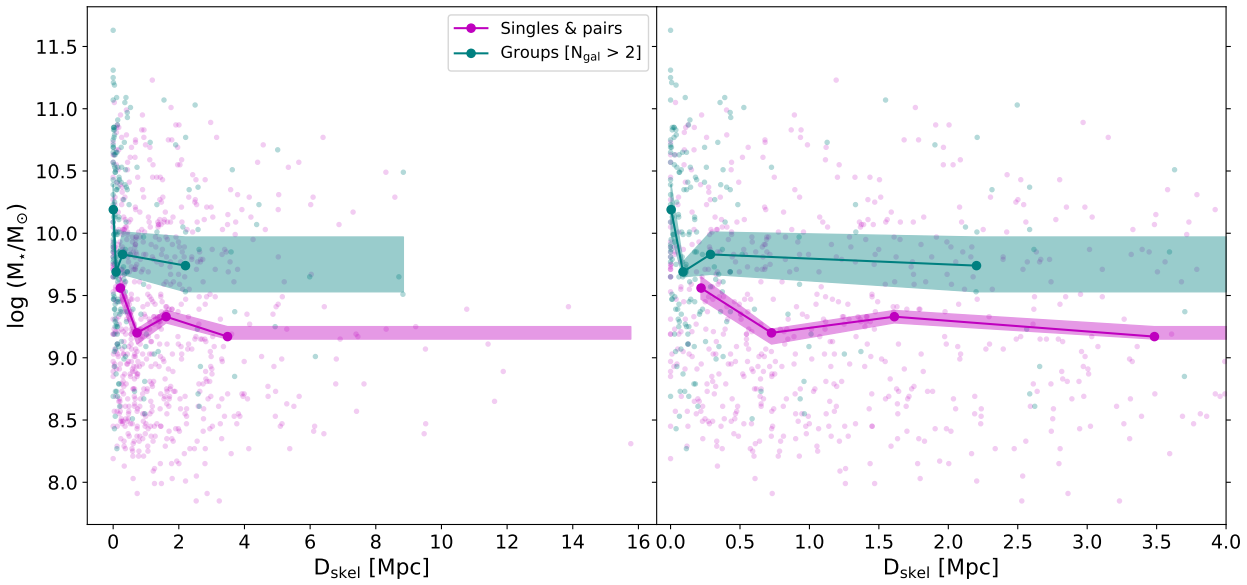

Figure 4.14: The median stellar mass ($\log(M_\star/M_\odot)$ vs distance to filament (D_{skel} [Mpc]) for galaxies in groups (in teal) compared to single and paired galaxies (pink). The right-hand panel shows the distributions for 0 Mpc < D_{skel} < 4 Mpc to highlight the behaviour close to the filaments.

Table 4.4: Spearman's Rank Test properties for log stellar mass vs distance to filament for galaxies in groups and singles + pairs, as shown in Figure 4.14

Measurement	N_{bins}	N_{dof}	Critical value for N_{dof}	r_s	Significant
log ($M_\star/M_\odot$) - groups	4	2	1	-0.4	No
log ($M_\star/M_\odot$) - singles + pairs	4	2	1	-0.8	No

groups that make up the filaments. These groups may pre-process galaxies, quenching star formation (Fujita, 2004), and resulting in an observed reddening in colour that is due to the groups rather than the filaments themselves.

To examine this effect, Figure 4.15 shows the number of galaxies in bins of *u* - *r* colour, by mass and group environment. These histograms show the bimodality of galaxies, where low-mass galaxies are bluer than high mass galaxies, and also indicate the environmental effect of groups by showing that group galaxies are redder than single and paired galaxies. Figure 4.16 shows that the median *u*-*r* colour for galaxies in groups ($N_{gal} \geq 3$) is higher than the median colour for single + pairs (N_{gal} < 3). This is expected because of group pre-processing, resulting in redder colours. Galaxies close to filaments in groups appear to be redder than galaxies further away. However, this trend is not statistically significant (see Table 4.5). The median colour for single + pair galaxies shows no trend with distance to filament. Similarly, when broken down by mass as in Figure 4.17, the low mass, group galaxies show a decreasing trend in median colour with distance to filament, but this trend is not statistically significant (see Table 4.6).

Overall, this suggests that the trend for low mass galaxies described in subsection 4.1.2 may

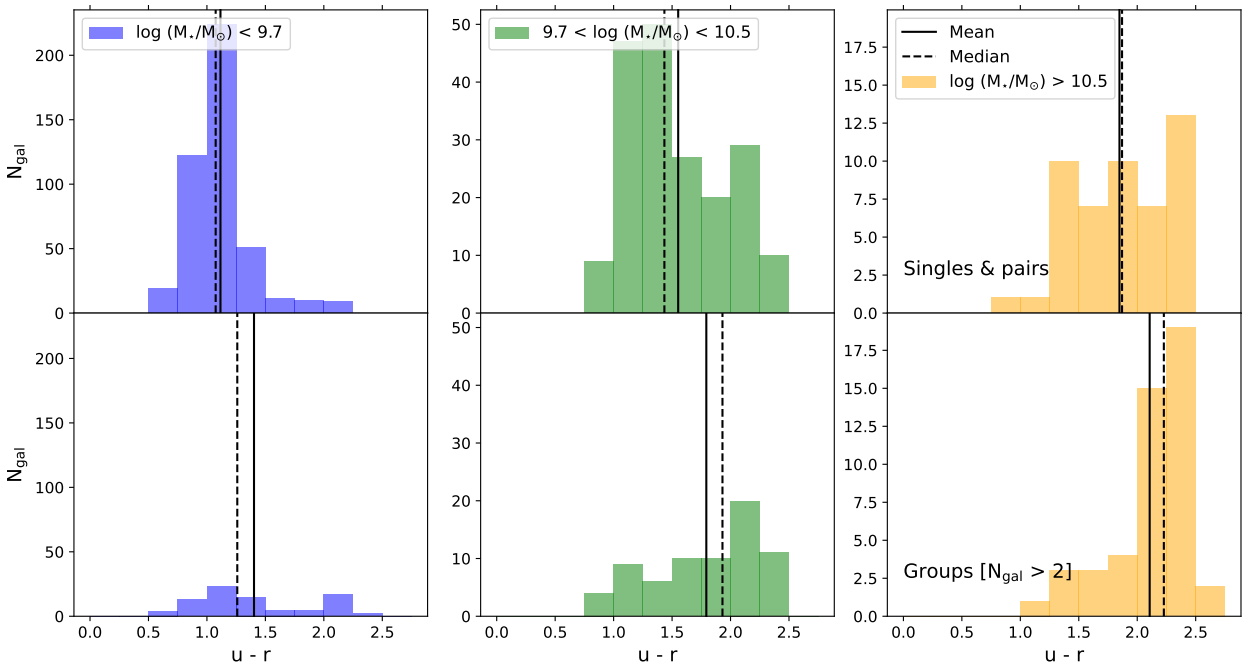

Figure 4.15: Histograms showing the number of galaxies in bins of *u-r* colour. The top row shows galaxies with $N_{gal} < 3$ and the bottom row shows galaxies in groups ($N_{gal} \geq 3$). Dashed lines indicate the median value and solid lines indicate the mean value for each subsample.

be due to the group environment rather than the filament environment.

Table 4.5: Spearman's Rank Test properties for *u - r* colour vs distance to filament for galaxies in groups and singles + pairs, as shown in Figure 4.16.

Measurement	N_{bins}	N_{dof}	Critical value for N_{dof}	r_s	Significant
u - r colour - groups	4	2	1	0.8	No
u - r colour - singles + pairs	4	2	1	0.4	No

4.2.4 Gas fraction

As shown in subsection 4.2.1, groups may affect the gas content of galaxies. To investigate the effect of filaments when group galaxies are removed, Figure 4.19 shows the median gas fraction vs distance to filament for singles + pairs ($N_{gal} < 3$) and groups ($N_{gal} \geq 3$). The median gas fraction for single + pair galaxies is systematically higher than group galaxies. Additionally, the median gas fraction for group galaxies increases significantly for $D_{skel} < 2.5$ Mpc (Table 4.7). When broken down by mass, as shown in Figure 4.20, this increase is reflected by the increase in gas fraction for low and intermediate mass group subsamples. However, these trends are not significant at the $\alpha = 0.1$ level. Additionally, low-mass, single + pair galaxies show a significant increasing trend in gas fraction with distance to filament (Table 4.8).

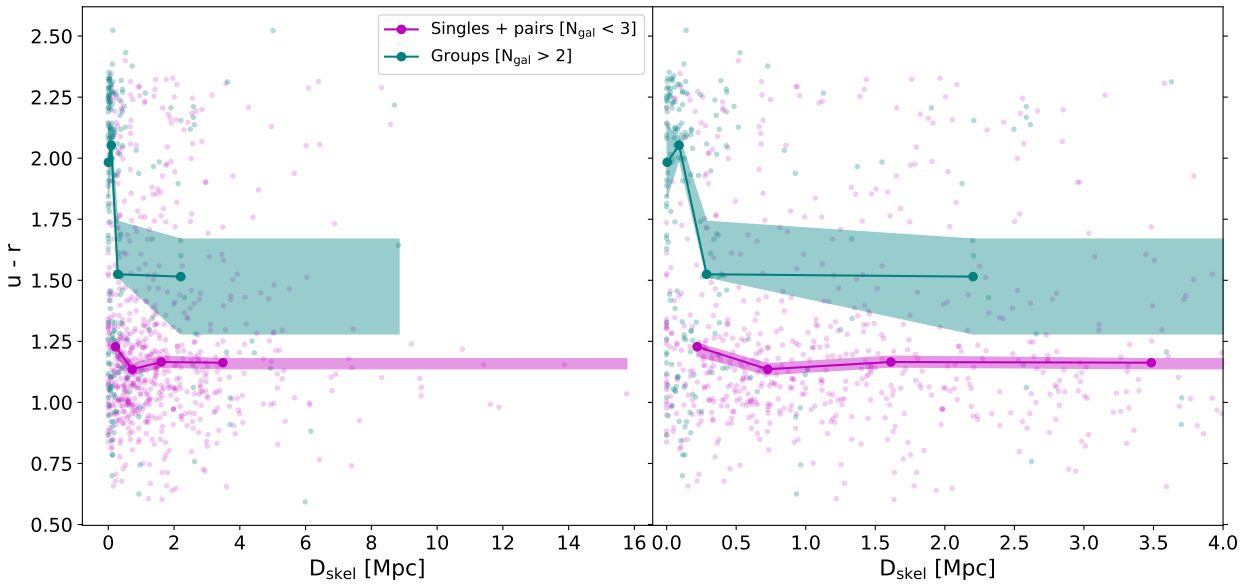

Figure 4.16: The median *u*-*r* colour vs distance to filament (D_{skel} [Mpc]) for galaxies in groups (in teal) compared to single and paired galaxies (pink). The right-hand panel shows the distributions for 0 Mpc < D_{skel} < 4 Mpc to highlight the behaviour close to the filaments.

Table 4.6: Spearman's Rank Test properties for *u* - *r* colour vs distance to filament for galaxies in groups and singles + pairs, by mass, as shown in Figure 4.17

Measurement	N_{bins}	N_{dof}	Critical value for N_{dof}	r_s	Significant
u - *r* colour - low mass group	4	2	1	-0.8	No
u - *r* colour - int mass group	4	2	1	-0.6	No
u - *r* colour - high mass group	4	2	1	0.4	No
u - *r* colour - low mass singles + pairs	5	3	0.9	0.3	No
u - *r* colour - int mass singles + pairs	4	2	1	0.2	No
u - *r* colour - high mass singles + pairs	4	2	1	0.4	No

4.3 Summary

In this chapter, I have shown that galaxies in RESOLVE-A have higher stellar masses close to filaments and that the median stellar mass of galaxies decreases as distance to filament increases up to D_{skel}= 1.5 Mpc. Low mass galaxies are redder close to filaments. However, when group galaxies are removed, this trend is no longer present. This may indicate that the redder colours of low mass galaxies close to filaments is due to group pre-processing, rather than the effects of filaments. Additionally, low mass galaxies increase in gas fraction as distance to filament increases, even when group galaxies are accounted for.

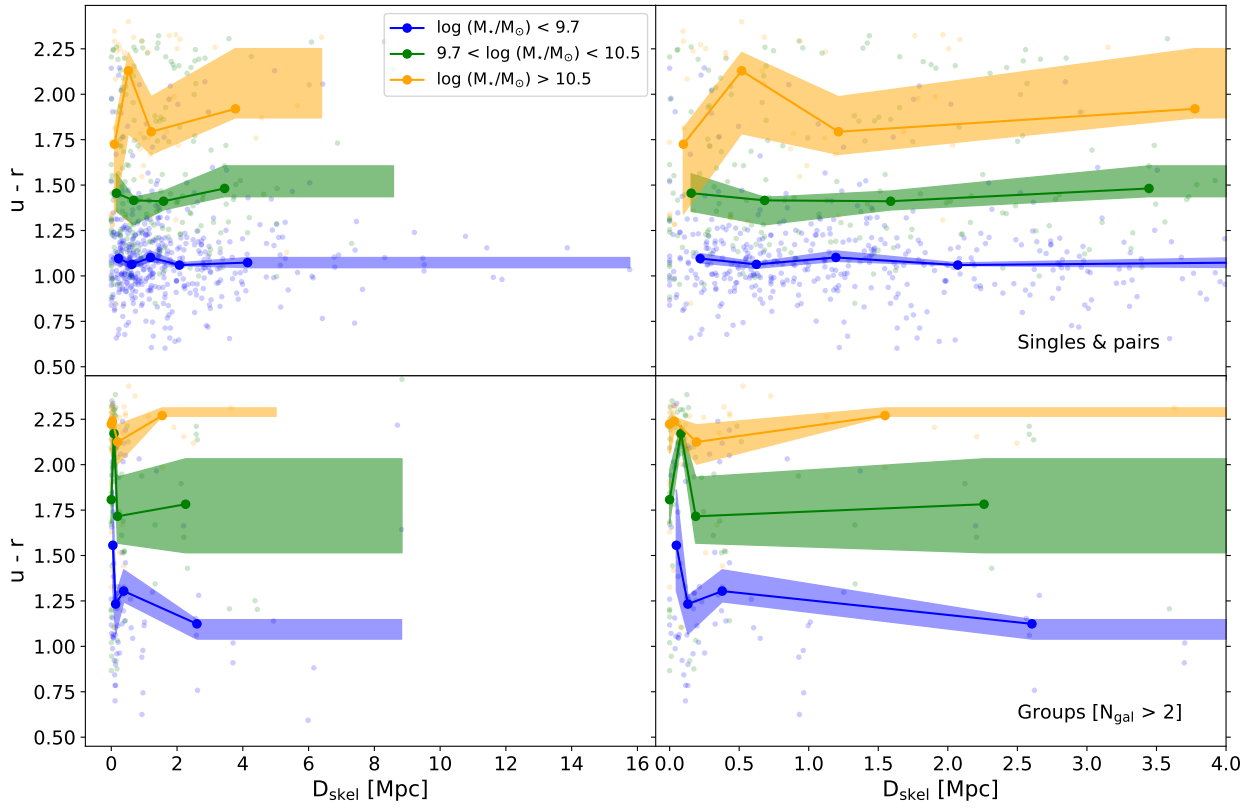

Figure 4.17: The median *u-r* colour vs distance to filament (D_{skel}[Mpc]) for single and paired galaxies is shown in the upper panels, in stellar mass bins. Low mass galaxies are represented in blue. Intermediate mass galaxies are shown in green, with high mass galaxies shown in orange. The lower panels show the trends for galaxies in groups. The right-hand panels shows the distributions for 0 Mpc < D_{skel}< 4 Mpc to highlight the behaviour close to the filaments.

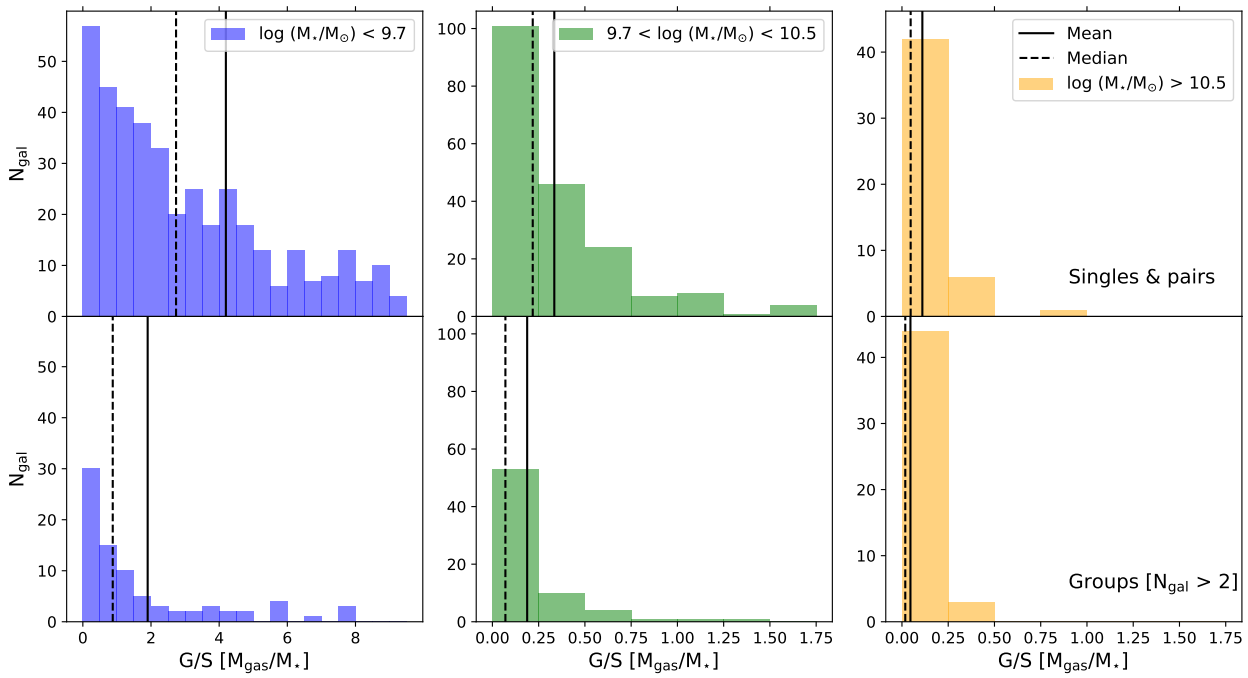

Figure 4.18: Histograms showing the number of galaxies in bins of gas fraction ($M_{HI}/M_{\star}$). The top row shows galaxies with $N_{gal}< 3$ and the bottom row shows galaxies in groups ($N_{gal}\geq 3$. Dashed lines indicate the median value and solid lines indicate the mean value for each subsample. The low-mass galaxies are assigned larger bins, to capture the full range of values.

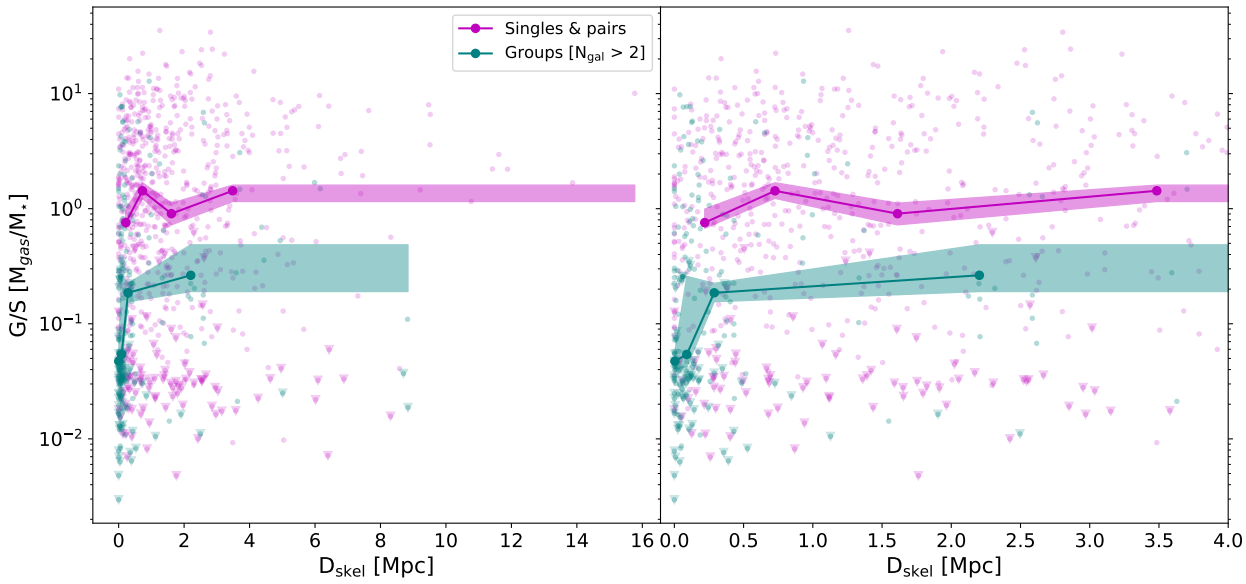

Figure 4.19: The median gas fraction ($M_{HI}/M_{\star}$) vs distance to filament (D_{skel} [Mpc]) for galaxies in groups (in teal) compared to single and paired galaxies (pink). The gas fraction is represented on a log axis for clarity. Arrows indicate galaxies where upper limit estimates are used to determine the gas fraction. The right-hand panel shows the distributions for 0 Mpc < D_{skel} < 4 Mpc to highlight the behaviour close to the filaments.

Table 4.7: Spearman's Rank Test properties for gas fraction vs distance to filament for galaxies in groups and singles + pairs, as shown in Figure 4.19

Measurement	N_{bins}	N_{dof}	Critical value for N_{dof}	r_s	Significant
G/S - groups	4	2	1	1	Yes
G/S - singles + pairs	4	2	1	0.8	No

Table 4.8: Spearman's Rank Test properties for gas fraction vs distance to filament for galaxies in groups and singles + pairs, by mass, as shown in Figure 4.20

Measurement	N_{bins}	N_{dof}	Critical value for N_{dof}	r_s	Significant
G/S - low mass group	4	2	1	0.8	No
G/S - int mass group	4	2	1	0.8	No
G/S - high mass group	4	2	1	0	No
G/S - low mass singles + pairs	5	3	0.9	0.9	Yes
G/S - int mass singles + pairs	4	2	1	-0.8	No
G/S - high mass singles + pairs	4	2	1	0	No

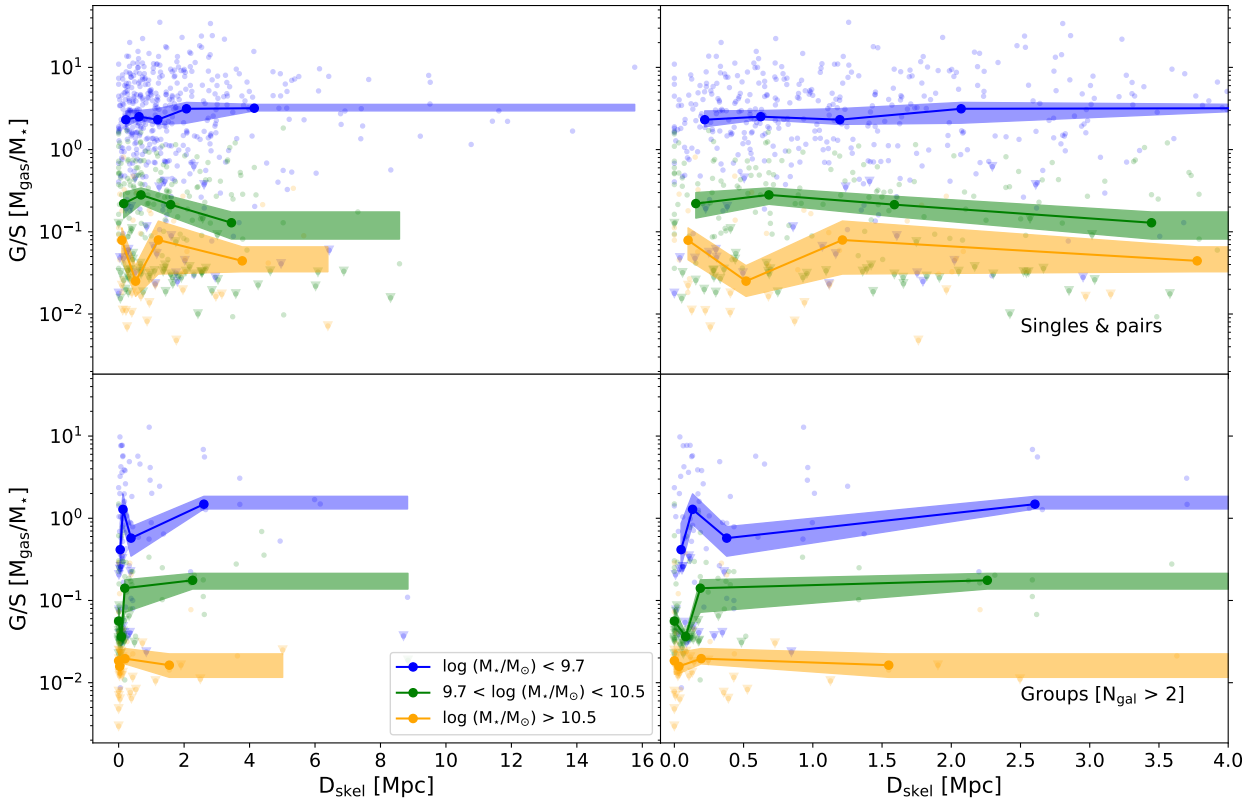

Figure 4.20: The median gas fraction ($M_{HI}/M_\star$) vs distance to filament (D_{skel}[Mpc]) is shown for single and paired galaxies (upper panels) and group galaxies (lower panels), in bins of stellar mass. The gas fraction is represented on a log axis. Arrows indicate galaxies where upper limit estimates are used to determine the gas fraction. The right-hand panel shows the distributions for 0 Mpc < D_{skel}< 4 Mpc to highlight the behaviour close to the filaments.

Chapter 5

Discussion

The current framework for understanding how filaments affect galaxy evolution suggests that the filament 'backbone' is made up of higher-mass galaxies and groups. This has been supported by observations of mass segregation within filaments - where galaxies at the core of filaments have higher stellar masses than galaxies outside filaments (Chen et al., 2017; Kraljic et al., 2017). Furthermore, Tidal Torque Theory (Hoyle, 1949; Peebles, 1969; Doroshkevich, 1970; White, 1984) provides a mechanism for low-mass galaxies to accrete gas at the 'vorticity-rich' outskirts of filaments (Laigle et al., 2015). Additionally, as galaxies enter filaments, they may become detached from their primordial gas supply through major mergers, accretion of satellites or as they cross the filament. Filaments are typically classified as intermediate-density regions. As such, various authors (Guo et al., 2015; Kuutma et al., 2017; Aragon Calvo et al., 2019) suggest that galaxy-galaxy mergers and interactions may occur frequently and drive morphological transformations such as those observed by Kuutma et al. (2017). Galaxies in groups travelling along filaments to higher-density regions such as clusters may be pre-processed by the groups, which may result in morphological and gas fraction changes to the galaxies (Fujita, 2004; Sarron et al., 2019).

In the previous chapter, I showed that galaxies in RESOLVE-A are more massive close to filaments. Low mass galaxies increase in gas fraction as the distance to filament increases. Although low-mass galaxies are redder close to filaments, this trend is no longer present when groups are removed. In this chapter, I will place these observed trends into context by comparing to previous work and explore how these trends may be affected by the choice of distance metric and contributions from high-density nodes. I will also examine possible mechanisms for driving these trends.

5.1 Stellar Mass

It is well established that stellar mass is the most crucial predictor of a galaxy's properties, even when environment is considered (Kauffmann et al., 2004; Kauffmann et al., 2003; Peng et al., 2010; Alpaslan et al., 2014b). In the previous chapter, Figure 4.4 showed that the median stellar mass of galaxies is higher within 1.5 Mpc of filaments than further away.

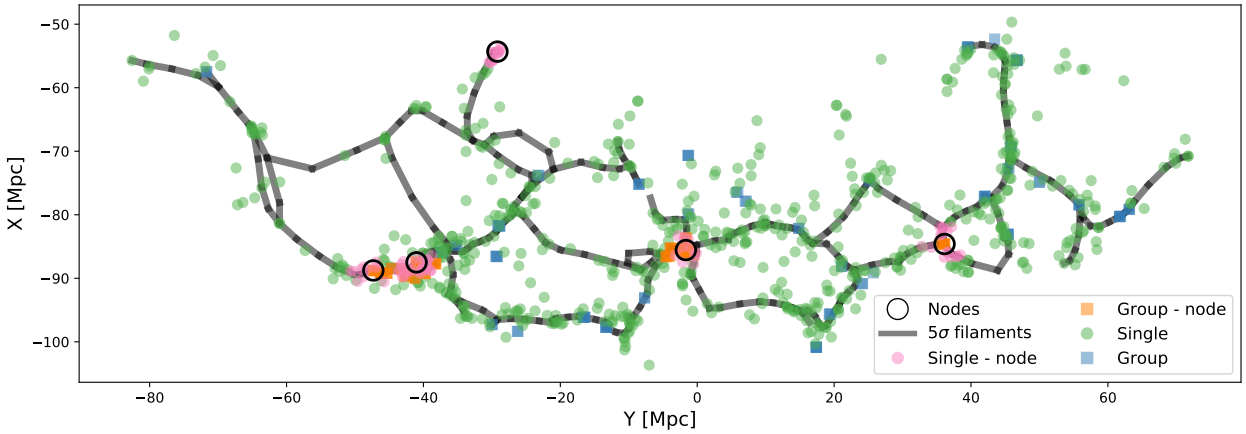

Figure 5.1: The distribution of galaxies with respect to nodes. Nodes are marked by open, black circles. Galaxies that are within 3.5 Mpc of a node and are removed from the analysis in this section are marked in pink and orange. Square symbols denote galaxies that belong to groups. The majority of 'node galaxies' fall within groups.

Laigle et al. (2017) and Kraljic et al. (2017) showed that high-density nodes (see Section 3.3), found at the intersection of filaments, may introduce additional gradients in properties like stellar mass which may be mis-attributed to filaments. This is typically corrected by removing galaxies within the vicinity of these nodes before performing further analysis. In this work, nodes correspond closely to many of the large groups (see Figure 5.1). Separating groups from single and paired galaxies, as done in Chapter 4, therefore has a similar result as removing galaxies near nodes with the additional advantage of removing the effects of smaller groups. However, to test whether nodes have an effect on the observed trends and to compare directly to Laigle et al. (2017); Malavasi et al. (2017); Kraljic et al. (2017), galaxies within 3 Mpc of the nodes identified by DisPerSE are removed. These galaxies are shown using pink and orange symbols in Figure 5.1. The average stellar mass vs distance to filament when 'node galaxies' are excluded and when they are included is shown in Figure 5.2. Note that in this chapter, the coloured bands indicating the 1 σ uncertainty are removed from the figures to facilitate comparisons.

Figure 5.2 shows that the trends with stellar mass persist when node galaxies are removed. This indicates that this trend is driven by the filaments, rather than affected by nodes. As shown in Figure 4.14 in the previous chapter, groups may also contribute to this trend.

The increase in stellar mass close to filaments after removing node galaxies is in agreement with the trends in stellar mass observed by Laigle et al. (2017); Kraljic et al. (2017) in the COSMOS2015 and GAMA surveys and Malavasi et al. (2017) in the high-redshift VIMOS survey.

While D_{skel} is most commonly used as the metric for measuring the distance to filaments in studies that use DisPerSE for filament identification, Luber et al. (2019) and Blue Bird et al. (2020) use the distance to nearest critical point, D_{cp}, in their analysis of galaxy properties. As described in Chapter 3, D_{cp} was also calculated for each galaxy. Figure 5.3 shows the comparison of D_{skel} and D_{cp}. Although there is an overall agreement between the two

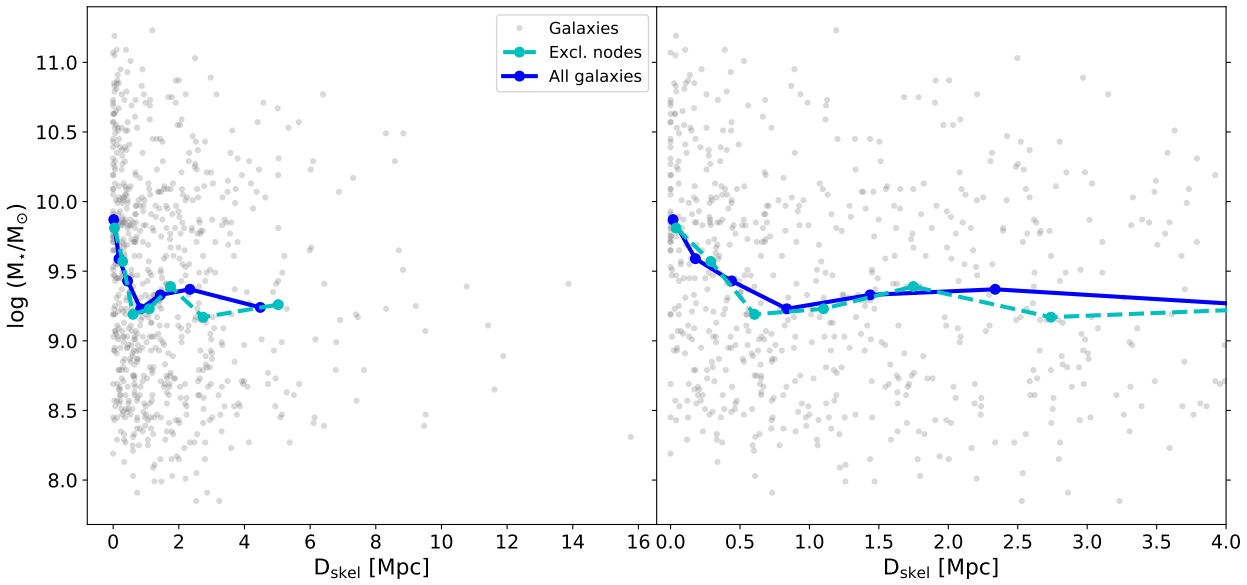

Figure 5.2: The median stellar mass vs distance to filament (D_{skel}) for all galaxies is shown as a solid blue line. For comparison, the median stellar mass vs $D_{skel}$when galaxies within 3.5 Mpc from the nodes are removed is shown as a cyan dashed line. The right-hand panel shows the distributions for 0 Mpc < D_{skel} < 4 Mpc to highlight the behaviour close to the filaments

metrics, the critical point distances are larger than the distance to skeleton in several cases. Critical points form the endpoints of filament segments. D_{skel}measures the perpendicular distance to the nearest filament segment, while D_{cp} measures the distance to the nearest critical point. For a galaxy near the center of a filament segment, $D_{skel}$is expected to be smaller than D_{cp}.

In comparison to Luber et al. (2019), the average stellar mass is calculated in bins of D_{cp} and is shown in Figure 5.4. This figure shows that the same trend in stellar mass is found when D_{cp} is used rather than D_{skel}. Galaxies at distances less than 1.5 Mpc are more massive than galaxies at larger distances when D_{cp} is used. Unlike the D_{skel}trend, there is no 'bump' between 1-3 Mpc. This may indicate that the 'bump' may be caused by the choice of distance metric and binning process, rather than physical mechanisms. Additionally, the decrease in average stellar mass is larger in this work than in (Luber et al., 2019), dropping by $\approx$ 0.7 dex, whereas Luber et al. (2019) find a decrease of $\approx$ 0.4 dex. The results are in good agreement with each other, overlapping within the 1 σ uncertainties.

When comparing how the stellar mass changes with respect to filaments, the results from this study are in good agreement with the literature. I have shown that the trend where galaxies close to filaments have higher stellar masses than galaxies further away from filaments holds when galaxies near nodes are excluded and when a different distance indicator is used. This supports the notion that the core of filaments are made up of more massive galaxies.

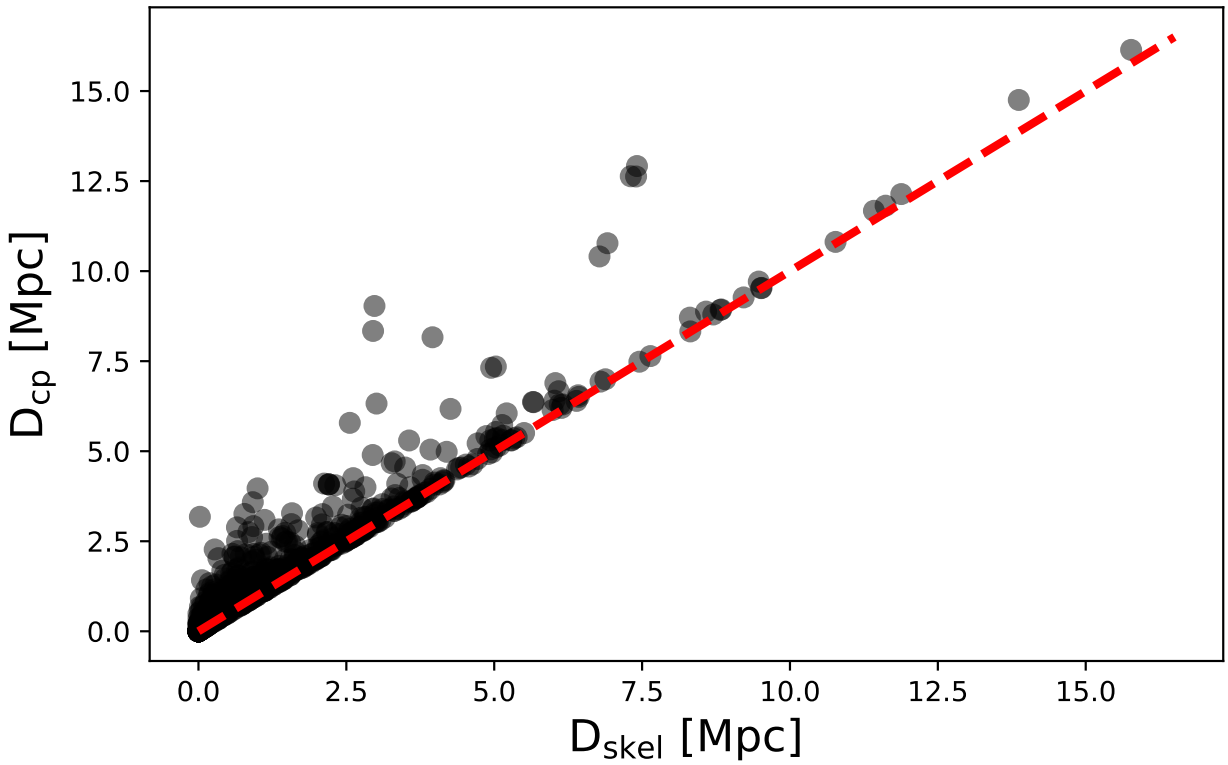

Figure 5.3: The distance to critical point (D_{cp}) in Mpc vs distance to skeleton D_{skel}in Mpc are compared. A line indicating a one-to-one relation is overplotted in red. While both distance metrics produce similar results, the D_{cp} values are typically larger than the D_{skel}values.

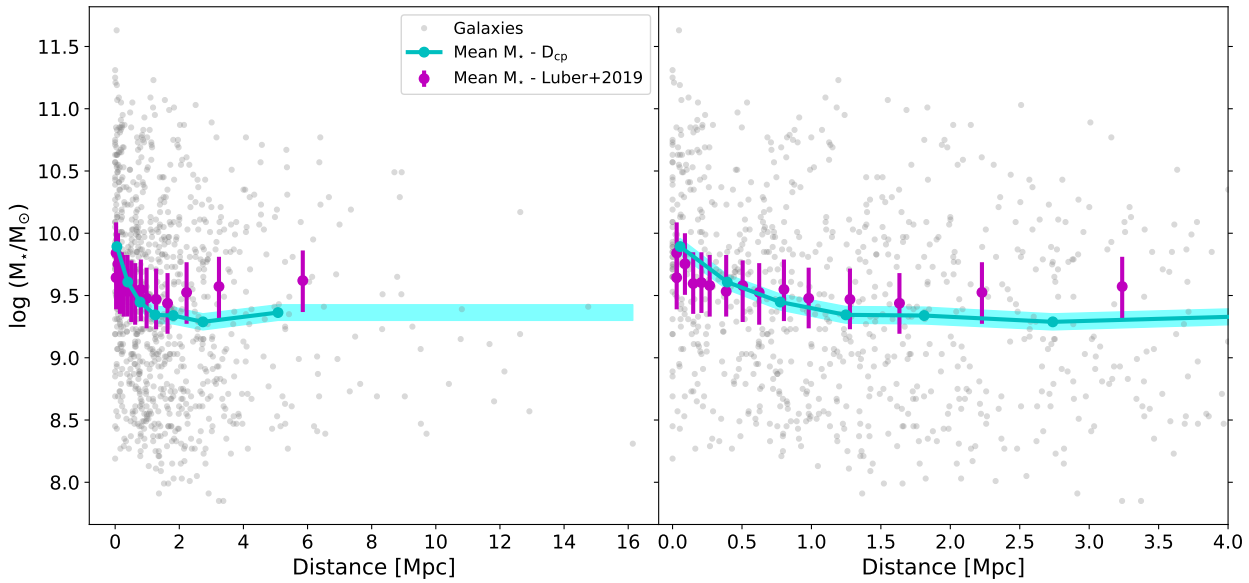

Figure 5.4: The average stellar mass vs distance to nearest critical point in this work (cyan) is shown in comparison to the average stellar mass vs distance to nearest critical point from Luber et al. (2019) (magenta). The cyan band shows the 1 σ error on the mean. The right-hand panel shows the distributions for 0 Mpc < D_{cp} < 4 Mpc to highlight the behaviour at small distances.

5.2 Colour and star formation

The colour-magnitude diagram reveals that a sample of galaxies will typically form a bimodal distribution - a red sequence consisting of quenched, mostly early-type galaxies, and a 'blue cloud' of galaxies that are actively forming stars (Baldry et al., 2004).

Colour is also closely tied to environment and galaxy density. In high-density regions such as galaxy clusters, the red sequence dominates (Hogg et al., 2003). Pre-processing may redden of galaxies in groups by quenching star-formation through mechanisms such as strangulation and evaporation, which reduce the quantity of gas available to form stars (Fujita, 2004). In addition, recent studies found evidence for an enhanced red fraction (Kraljic et al., 2017; Chen et al., 2017), redder colour (Laigle et al., 2017; Kuutma et al., 2017; Luber et al., 2019) and an increased fraction of passive (i.e. non star-forming) galaxies) close to filaments (Kraljic et al., 2017; Malavasi et al., 2017; Sarron et al., 2019; Laigle et al., 2017). This suggests that quenching mechanisms may be at play within filaments.

To isolate the effect of filaments on colour and compare to Kraljic et al. (2017), the median colour with respect to distance to filament, when node galaxies are removed, is examined. Kraljic et al. (2017) found an increase in non-star forming galaxies or a reddening of galaxies, indicative of quenching. Figure 5.5 shows the median colour vs distance to filament (D_{skel}) when the contribution of nodes is removed, in bins of stellar mass described in Chapter 4 to control for the mass-dependence. The low mass subsample shows no difference in median *u-r* colour when node galaxies are removed. The median colour for intermediate mass galax-

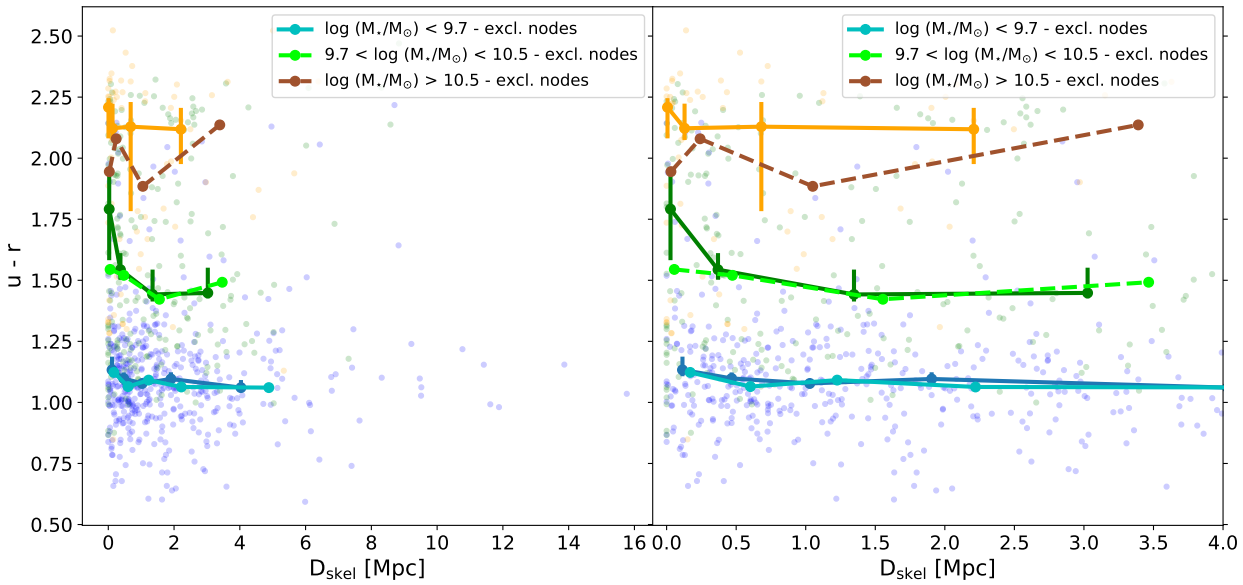

Figure 5.5: The median *u-r* colour vs distance to filament when galaxies within 3.5 Mpc from nodes are removed is shown for low mass galaxies (cyan), intermediate mass galaxies (lime) and high mass galaxies (brown). For comparison, the blue, green and orange lines indicate the median *u-r* colour vs distance to filament when galaxies close to nodes are not removed. The uncertainty on the median colour is plotted using errorbars for the samples when node galaxies are included for comparison. The right-hand panel shows the distributions for 0 Mpc < D_{skel} < 4 Mpc to highlight the behaviour at small distances.

ies is also unaffected when node galaxies are removed, except in the lowest distance bin. The median colour for the high mass subsample is lower (i.e. galaxies are bluer) when node galaxies are removed, indicating that nodes contribute to reddening. The result is only in partial agreement with Kraljic et al. (2017) since a statistically significant decrease in colour is only found for low mass galaxies while Kraljic et al. (2017) identified trends in colour at higher masses (log $M_\star/M_\odot \geq$ 9.92). However, as shown in Section 4.2.3, this trend may be additionally influenced by groups which do not occur at the nodes.

Using data from the CHILES survey, Luber et al. (2019) found that *NUV - r* colour decreased with increasing distance from the nearest critical point (D_{cp}). Figure 5.6 shows the average *u - r* colour vs distance to nearest critical point for galaxies in RESOLVE. Similarly to the results for stellar mass, the average colour is 'smoothed out' when D_{cp} is used. However, the overall trends in colour are unaffected by the change in distance metric. The decrease in colour in the low-mass subsample is likely due to the effect of groups, as shown in Section 4.2.3.

Overall, although reddening in colour for galaxies closer to filaments is observed throughout the literature (Kraljic et al., 2017; Luber et al., 2019; Kuutma et al., 2017; Chen et al., 2017), the same trend is not seen in this work after accounting for nodes.

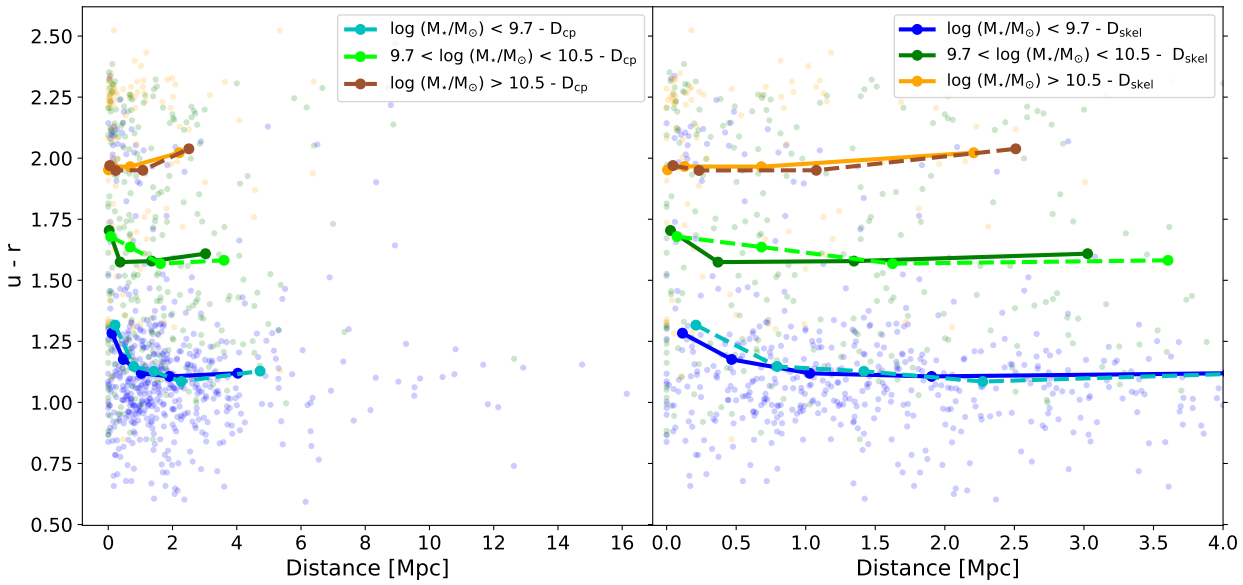

Figure 5.6: The average colour vs distance to nearest critical point and distance to filament in Mpc, in bins of mass, is shown. High mass galaxies are shown as brown (D_{cp}) and orange (D_{skel}) lines. Intermediate mass galaxies are shown in green (D_{skel}) and lime (D_{cp}). The low mass galaxies are shown in blue (D_{skel}) and cyan (D_{cp}).The right-hand panel shows the distributions for 0 Mpc < D_{cp}/ D_{skel}< 4 Mpc to highlight the behaviour at small distances.

5.3 Gas Fraction

While trends in colour and stellar mass with respect to filaments have been well-established, understanding the role of filaments on the gas content of galaxies requires more investigation. Tidal Torque Theory predicts that high stellar mass galaxies will have perpendicular spin (angular momentum), while low stellar mass galaxies are spin aligned to their host filament (Porciani et al., 2002; Codis et al., 2015). Laigle et al. (2017) suggests that this spin alignment allows low stellar mass galaxies to accrete cold gas efficiently at the 'vorticity-rich' outskirts of filaments. This stellar mass-dependent spin alignment has been observed by Welker et al. (2019) for galaxies with stellar masses below the 10.4 < log $M_\star/M_\odot$< 10.9 'transition mass' range (where galaxies transition from being spin-aligned to spin-perpendicular to filaments) and was later also observed by (Blue Bird et al., 2020) using observations from the CHILES survey. Using the SIMBA simulations, Kraljic et al. (2020) found that galaxies with high HI mass (log $M_{HI}/M_\odot$> 9.5) were spin-aligned with their host filaments and galaxies with low HI mass (log $M_{HI}/M_\odot$< 9.5) were spin-perpendicular to filaments, further implying that spin alignment and gas accretion are linked. Additionally, when examining gas refuelling and the resultant star formation properties of galaxies, independent of the cosmic web environment, Kannappan et al. (2013) showed that the low stellar mass, gas-richness threshold corresponds to an accretion-dominated refuelling regime, where galaxies grow through gas accretion.

Observationally, Kleiner et al. (2016) observed that high mass (log $M_\star/M_\odot$> 11) galaxies close to filaments (with D_{skel}< 0.7 Mpc) had higher gas fractions than their control sample

with $D_{skel} > 5$ Mpc. They interpreted this as possible HI cold accretion by massive galaxies from filaments. The RESOLVE-A sample contains only 15 galaxies with $\log M_\star/M_\odot > 11$. Within this mass range, only 11 galaxies lie within $D_{skel} < 0.7$ Mpc, with the remaining 4 galaxies at $D_{skel} < 2.5$ Mpc. Although this is not directly comparable to Kleiner et al. (2016) due to the limited statistics at this mass range, the highest stellar mass bin used in this work ($\log M_\star/M_\odot > 10.5$) does not show a trend in gas fraction with distance to filament. However, in the CHILES survey, Luber et al. (2019) predicted that the gas fraction for galaxies would decrease close to filaments and Blue Bird et al. (2020), using a sample of 10 galaxies, found that galaxies had higher HI masses further away from filaments, but found no increase in gas fraction within their small sample.

Additionally, Odekon et al. (2018) found that at fixed stellar masses and colour, filament galaxies, with $8.5 < \log M_\star/M_\odot < 10.5$, are more HI deficient than non-filament galaxies. They suggest a scenario where galaxies enter filaments and are cut off from their gas supply, resulting in the observed HI deficiencies and later redden as star formation is quenched. This is in agreement with the Cosmic Web Detachment model (Aragon Calvo et al., 2019), which describes how galaxies are quenched after being detached from the cosmic web.

Although Odekon et al. (2018) detect a decrease in the gas content of galaxies and Kleiner et al. (2016) detect an increase in the gas content of galaxies due to the cosmic web, these changes are observed in different stellar mass regimes. One interpretation of this is that galaxies with very high stellar masses may have enough gravitational potential to funnel gas from the cosmic web (Kleiner et al., 2016), while low mass galaxies are more susceptible to ram-pressure stripping within filaments (Benítez-Llambay et al., 2013).

Stark et al. (2016) examined the gas properties of galaxies in the RESOLVE survey. They found that the fraction of gas-poor, central galaxies increased with large scale structure density. Their work suggested that the cosmic web may be influencing the gas properties of galaxies, but required more investigation.

Because the RESOLVE survey has a high level of completeness and extensive HI data, it is possible to study the effect of the cosmic web on gas fraction in detail. The large sample size is sufficient for examining trends in separate bins of stellar mass. Additionally, the inclusion of a group catalogue ensures that trends due to group environments can be disentangled from trends due to cosmic web filaments. As shown in Section 4.2.4 and Figure 4.10, the gas fraction for galaxies in RESOLVE-A increases when the distance to filament increases for low-mass, single and paired galaxies. Galaxies in groups are closer to filaments and more HI deficient than galaxies further away. Group galaxies have, on average, lower gas fractions than single and paired galaxies.

Figure 5.7 shows the average gas fraction vs distance to critical point (D_{cp}) and distance to filament (D_{skel}), in bins of stellar mass, in comparison to Luber et al. (2019) and Blue Bird et al. (2020), which included galaxies with $7.5 < \log M_\star/M_\odot < 11.5$. This figure shows that when D_{cp} is used the average gas fraction shows the same trends as in Figure 4.10 - the gas fraction increases as distance to critical point increases for low-mass galaxies and shows little variation with distance for the intermediate and high mass samples.

There are several ways of interpreting the change in gas fraction with distance to filament

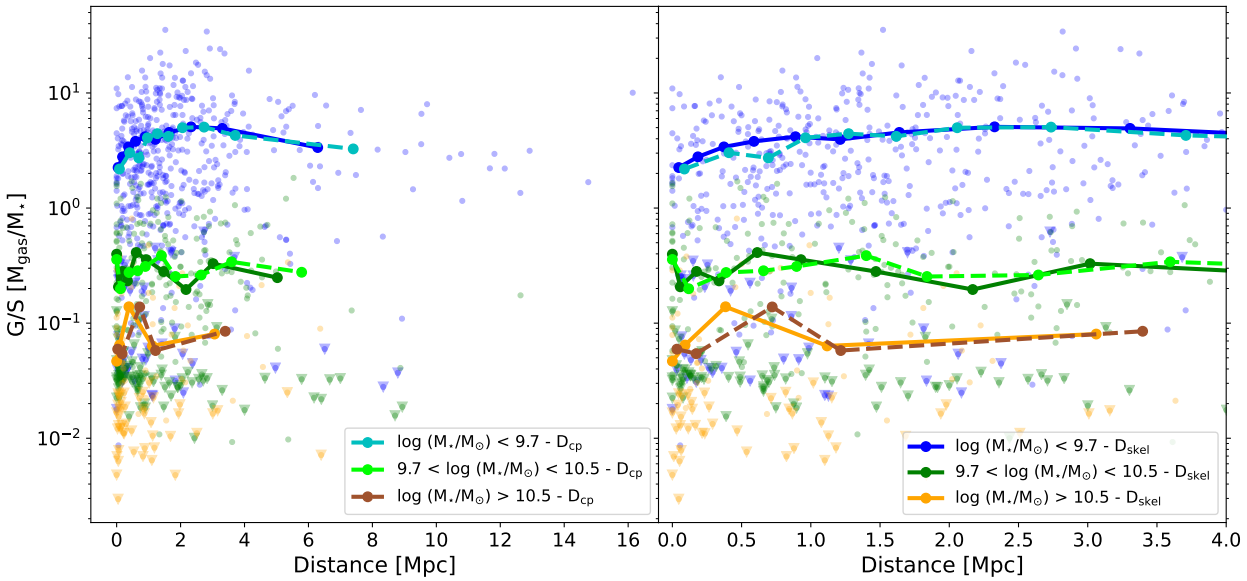

Figure 5.7: The average gas fraction vs distance to nearest critical point and distance to filament in Mpc, in bins of mass, is shown. High mass galaxies are shown as brown (D_{cp}) and orange (D_{skel}) lines. Intermediate mass galaxies are shown in green (D_{skel}) and lime (D_{cp}). The low mass galaxies are shown in blue (D_{skel}) and cyan (D_{cp}). The gas fraction is shown on a log y-axis to emphasise the trends in the intermediate and high mass bins. Arrows indicate galaxies where upper limit estimates are used to determine the gas fraction. The right-hand panel shows the distributions for 0 Mpc < D_{cp}/ D_{skel}< 4 Mpc to highlight the behaviour at small distances.

for low-mass galaxies. As shown in Figure 4.20, the trends persist when group galaxies are removed. The gas fraction for low mass galaxies increases as distance to filament increases, indicating that galaxies are less gas-rich close to or within filaments. This may suggest that these low-mass galaxies are cut-off from their primordial gas supply once they enter filaments, as suggested by Cosmic Web Detachment (Aragon Calvo et al., 2019). Similarly, Cosmic Web Stripping, which was identified in simulations by Benítez-Llambay et al. (2013), is a process which removes gas from low-mass, dwarf galaxies through ram-pressure as they interact with cosmic web filaments.

While one would expect a subsequent change in colour, due to star formation quenching, corresponding to this cut-off, there may be a delay between the cut-off in gas supply and change in colour, particularly for low-mass galaxies which may be gas-rich enough to continue star formation.

Because this increase in gas fraction in Figure 4.20 'peaks' at $D_{\rm skel} \sim$ 2 Mpc, another interpretation is that 2-3 Mpc from the filament is close enough to the filament outskirts for the low-mass galaxies to accrete gas from the filaments, resulting in a peak in average gas fraction within this distance range. This could be investigated by examining if these galaxies are spin-aligned with the filaments, which is beyond the scope of this project. However, a large sample at higher distances from filaments is needed to fully determine how this trend continues. Alternatively, a combination of these effects, along with the effects described in Stark et al. (2016) such as fly-by and 'splash-back' interactions between groups, where galaxies enter larger haloes and are stripped of their gas before being ejected, may be contributing to the overall trends in gas fraction.

Chapter 6

Summary and Conclusion

Observational studies of galaxy properties and large scale structure are key to understanding the role of the cosmic web and other environments on galaxy evolution. Previous studies and theoretical predictions suggest that galaxies within cosmic web filaments have higher stellar mass, redder colour and lower star formation rate than galaxies outside of filaments, and follow the morphology-density relation (Dressler, 1980). However, there is still tension in the literature with regards to the role of filaments on the gas properties of galaxies.

In this study, I took advantage of the high quality, complete data from the Resolved Spectroscopy Of a Local VolumE (RESOLVE) survey to examine the role of the cosmic web filaments on the stellar mass, *u-r* colour and gas properties of galaxies in the RESOLVE-A field. RESOLVE has extensive data on the gas, stellar and group properties of galaxies and covers a total volume of $\sim$50 000 Mpc^3. This data-set is ideal for examining the role of cosmic web filaments on the gas properties of galaxies.

While there are several approaches for identifying components of the cosmic web, in this work, I used the Discrete Persistence Structures Extractor (DisPerSE). DisPerSE applies topological techniques to identify robust cosmic web filaments and is well suited to observational survey data. The filaments identified with DisPerSE in the RESOLVE-A field matched the galaxy distribution well.

To investigate the filament environment on galaxy properties compared to galaxies outside filaments, I examined the stellar mass, *u-r* colour, HI deficiency and gas fraction with respect to distance from filament and group environment in the RESOLVE-A field. My results are as follows:

- The average stellar mass of galaxies close to filaments is higher than the average stellar mass of galaxies further away from filaments. This trend is in agreement with the literature (Laigle et al., 2017; Luber et al., 2019; Kraljic et al., 2017) and persists when group galaxies are removed.
- When galaxy groups are removed there is no difference in *u-r* colour with respect to proximity to filament for all bins in stellar mass. Galaxies belonging to groups are redder than single + paired galaxies. Groups typically lie along filaments and may be

responsible for driving trends in colour, even when accounting for stellar mass.

- Low mass galaxies (log $M_\star/M_\odot < 9.7$) have lower gas fractions close to filaments on average. When group galaxies are accounted for, the trend in average gas fraction with distance to filament persists for low mass galaxies. This indicates that the filament environment, in addition to the group environment, influences the gas content of low mass galaxies.

Additionally, I examined the role of nodes, which are high density regions at the intersection of filaments and found no changes in the observed trends. My results for the trends in colour and gas fraction for low mass galaxies support the scenario where low-mass galaxies lose some of their gas as they enter filaments, but remain gas-rich enough to continue forming stars and thus do not express a change in colour. Additionally, there is no observed increase in gas fraction for high mass galaxies, as was found in Kleiner et al. (2016). However, this may be due to the limited sample of high mass galaxies in the RESOLVE-A field.

6.1 Future Outlook

There are several avenues for future work on this topic which may be explored beyond this work. The spin properties of galaxies may be examined to provide further insight into the question of gas accretion or quenching. The RESOLVE dataset would enable a study of this broken down by mass which would enable comparison to various models. The halo mass properties, along with the differences between central and satellite galaxies in groups, could be studied as an extension of the work by Stark et al. (2016). Additionally, data from the RESOLVE-B field and the Environmental COntext (ECO) catalogue (Moffett et al., 2015) could be used to further examine the effects of the cosmic web on galaxy evolution properties by increasing the number of galaxies in the sample and including larger filaments and other structures such as galaxy clusters.

The recently completed MeerKAT radio telescope is currently obtaining HI data for surveys such as the Looking At the Distant Universe with the MeerKAT Array (LADUMA) survey (Blyth et al., 2016) and the MeerKAT International GHz Tiered Extragalactic Exploration (MIGHTEE) survey (Jarvis et al., 2017), which will provide an exciting opportunity to examine the role of HI gas in the universe. The filament finding techniques and galaxy property analysis used in this work can be applied to data from these surveys to understand the mechanisms which affect HI gas at higher redshifts.

Overall, this work showed that observational studies of cosmic web filaments are important for understanding the mass assembly, morphological transformations and gas processes responsible for galaxy evolution and that there is still more work to be done to identify the different processes at work and how they affect galaxies in different mass regimes.

Appendix A

Data Tables

This appendix contains tables showing the number of bins, number of galaxies per bin and the bin median values for each plot in Chapter 4.

Table A.1: Log stellar mass in bins of distance to filament, as shown in Figure 4.4. The bin number, distance of the bin, the median log stellar mass, the lower and upper 1σ confidence intervals and the number of galaxies in each bin are shown.

Bin	D_{skel}	Med.	CI_{low}	CI_{up}	N_{gal}
1	0.02	9.87	9.81	9.91	127
2	0.18	9.59	9.47	9.69	127
3	0.44	9.43	9.35	9.49	127
5	0.84	9.23	9.13	9.31	127
5	1.44	9.33	9.29	9.39	127
6	2.34	9.37	9.17	9.49	127
7	4.48	9.24	9.17	9.36	126

Table A.2: The *u-r* colour by mass, in bins of distance to filament, as shown in Figure 4.7 for low mass (first column), intermediate mass (second column) and high mass (third column) galaxies. The bin number, distance of the bin, the median *u - r* colour, the lower and upper 1σ confidence intervals and the number of galaxies in each bin are shown.

	$\log\ (M_\star/M_\odot)$ < 9.7					9.7 < $\log\ (M_\star/M_\odot)$ < 10.5					$\log\ (M_\star/M_\odot)$ > 10.5)				
Bin	D_{skel}	Med.	CI_{low}	CI_{up}	N_{gal}	D_{skel}	Med.	CI_{low}	CI_{up}	N_{gal}	D_{skel}	Med.	CI_{low}	CI_{up}	N_{gal}
1	0.11	1.133	1.107	1.187	107	0.03	1.791	1.582	1.938	66	0.01	2.208	2.081	2.246	25
2	0.47	1.098	1.073	1.123	107	0.37	1.543	1.506	1.612	66	0.13	2.122	2.075	2.219	25
3	1.03	1.078	1.058	1.089	107	1.35	1.442	1.413	1.558	66	0.68	2.129	1.984	2.230	25
4	1.91	1.096	1.064	1.123	107	3.03	1.448	1.426	1.542	64	2.21	2.118	1.976	2.206	21
5	4.03	1.061	1.044	1.094	102										

Table A.3: Gas fraction by mass, in bins of distance to filament, as shown in Figure 4.10 for low mass (first column), intermediate mass (second column) and high mass (third column) galaxies. The bin number, distance of the bin, the median gas fraction, the lower and upper 1σ confidence intervals and the number of galaxies in each bin are shown.

	$\log\ (M_\star/M_\odot)$ < 9.7					9.7 < $\log\ (M_\star/M_\odot)$ < 10.5					$\log\ (M_\star/M_\odot)$ > 10.5)				
Bin	D_{skel}	Med.	CI_{low}	CI_{up}	N_{gal}	D_{skel}	Med.	CI_{low}	CI_{up}	N_{gal}	D_{skel}	Med.	CI_{low}	CI_{up}	N_{gal}
1	0.11	1.65	1.31	1.82	107	0.03	0.08	0.06	0.13	66	0.01	0.02	0.02	0.04	25
2	0.47	2.36	2.08	2.74	107	0.37	0.19	0.15	0.22	66	0.13	0.02	0.02	0.02	25
3	1.03	2.36	2.10	3.09	107	1.35	0.21	0.15	0.26	66	0.68	0.03	0.02	0.03	25
4	1.91	2.87	2.12	3.41	107	3.03	0.17	0.13	0.19	64	2.21	0.03	0.02	0.05	21
5	4.03	3.07	2.65	3.19	102										

Table A.4: Log stellar mass in bins of distance to filament, for galaxies in groups (left column) and singles + pairs (right column), as shown in Figure 4.14. The bin number, distance of the bin, the median log stellar mass, the lower and upper 1σ confidence intervals and the number of galaxies in each bin are shown.

	Groups					Singles + Pairs				
Bin	D_{skel}	Med.	CI_{low}	CI_{up}	N_{gal}	D_{skel}	Med.	CI_{low}	CI_{up}	N_{gal}
1	0.00	10.19	10.09	10.31	51	0.22	9.56	9.47	9.65	172
2	0.09	9.69	9.61	9.77	51	0.73	9.20	9.13	9.25	172
3	0.29	9.83	9.67	10.01	51	1.61	9.33	9.29	9.37	172
4	2.20	9.74	9.55	9.94	48	3.48	9.17	9.13	9.27	171

Table A.5: The *u* - *r* colour in bins of distance to filament, for galaxies in groups (left column) and singles + pairs (right column), as shown in Figure 4.16. The bin number, distance of the bin, the median *u* - *r* colour, the lower and upper 1σ confidence intervals and the number of galaxies in each bin are shown.

	Groups					Singles + Pairs				
Bin	D_{skel}	Med.	CI_{low}	CI_{up}	N_{gal}	D_{skel}	Med.	CI_{low}	CI_{up}	N_{gal}
1	0.00	1.983	1.844	2.131	51	0.22	1.228	1.192	1.248	172
2	0.09	2.053	1.997	2.082	51	0.73	1.136	1.114	1.158	172
3	0.29	1.525	1.514	1.690	51	1.61	1.166	1.144	1.191	172
4	2.20	1.515	1.281	1.779	48	3.48	1.163	1.132	1.186	171

Table A.6: Gas fraction in bins of distance to filament, for galaxies in groups (left panel) and singles + pairs (right column), as shown in Figure 4.19. The bin number, distance of the bin, the median gas fraction, the lower and upper 1σ confidence intervals and the number of galaxies in each bin are shown.

	Groups					Singles + Pairs				
Bin	D_{skel}	Med.	CI_{low}	CI_{up}	N_{gal}	D_{skel}	Med.	CI_{low}	CI_{up}	N_{gal}
1	0.00	0.05	0.04	0.06	51	0.22	0.76	0.67	0.99	172
2	0.09	0.05	0.04	0.26	51	0.73	1.43	1.23	1.66	172
3	0.29	0.19	0.13	0.22	51	1.61	0.91	0.73	1.12	172
4	2.20	0.26	0.19	0.53	48	3.48	1.43	1.17	1.58	171

Table A.7: The *u* - *r* colour in bins of distance to filament, for galaxies in groups (upper table) and singles + pairs (lower table), as shown in Figure 4.17, for low mass (first column), intermediate mass (second column) and high mass (third column) galaxies. The bin number, distance of the bin, the median *u* - *r* colour, the lower and upper 1σ confidence intervals and the number of galaxies in each bin are shown.

	$\log\ (M_\star/M_\odot)$ < 9.7					9.7 < $\log\ (M_\star/M_\odot)$ < 10.5					$\log\ (M_\star/M_\odot)$ > 10.5)				
Bin	D_{skel}	Med.	CI_{low}	CI_{up}	N_{gal}	D_{skel}	Med.	CI_{low}	CI_{up}	N_{gal}	D_{skel}	Med.	CI_{low}	CI_{up}	N_{gal}
1	0.05	1.556	1.315	1.840	22	0.00	1.807	1.678	1.969	18	0.00	2.223	2.058	2.246	12
2	0.13	1.233	1.067	1.270	22	0.08	2.171	2.118	2.218	18	0.03	2.239	2.191	2.256	12
3	0.38	1.304	1.252	1.400	22	0.19	1.716	1.568	1.931	18	0.19	2.125	2.003	2.219	12
4	2.60	1.124	1.040	1.147	18	2.26	1.782	1.515	2.016	16	1.55	2.270	2.206	2.313	11
1	0.22	1.096	1.075	1.125	90	0.16	1.455	1.398	1.562	49	0.10	1.725	1.341	1.813	13
2	0.62	1.064	1.040	1.075	90	0.68	1.416	1.281	1.432	49	0.52	2.129	1.783	2.230	13
3	1.20	1.102	1.080	1.137	90	1.59	1.411	1.363	1.521	49	1.21	1.794	1.669	1.986	13
4	2.07	1.060	1.054	1.072	90	3.45	1.481	1.423	1.606	45	3.78	1.920	1.870	2.251	10
5	4.14	1.074	1.045	1.101	86										

Table A.8: Gas fraction in bins of distance to filament, for galaxies in groups (upper table) and singles + pairs (lower table), as shown in Figure 4.20, for low mass (first column), intermediate mass (second column) and high mass (third column) galaxies. The bin number, distance of the bin, the gas fraction, the lower and upper 1σ confidence intervals and the number of galaxies in each bin are shown.

	$\log\ (M_\star/M_\odot)$ < 9.7					9.7 < $\log\ (M_\star/M_\odot)$ < 10.5					$\log\ (M_\star/M_\odot)$ > 10.5)				
Bin	D_{skel}	Med.	CI_{low}	CI_{up}	N_{gal}	D_{skel}	Med.	CI_{low}	CI_{up}	N_{gal}	D_{skel}	Med.	CI_{low}	CI_{up}	N_{gal}
1	0.05	0.42	0.26	0.87	22	0.00	0.06	0.05	0.08	18	0.00	0.02	0.01	0.02	12
2	0.13	1.28	0.90	1.79	22	0.08	0.04	0.03	0.04	18	0.03	0.02	0.01	0.02	12
3	0.38	0.57	0.35	0.74	22	0.19	0.14	0.07	0.18	18	0.19	0.02	0.02	0.03	12
4	2.60	1.48	1.30	1.85	18	2.26	0.18	0.14	0.21	16	1.55	0.02	0.01	0.02	11
1	0.22	2.31	1.89	2.96	90	0.16	0.22	0.15	0.36	49	0.10	0.08	0.05	0.11	13
2	0.62	2.51	2.29	2.98	90	0.68	0.28	0.22	0.36	49	0.52	0.03	0.02	0.04	13
3	1.20	2.31	1.98	3.15	90	1.59	0.21	0.15	0.27	49	1.21	0.08	0.03	0.14	13
4	2.07	3.14	2.12	3.69	90	3.45	0.13	0.09	0.17	45	3.78	0.04	0.03	0.06	10
5	4.14	3.19	2.96	3.57	86										

Appendix B

Spearman's Rank Test

The Spearman's Rank Correlation coefficient (r_s) (Spearman, 1904) is used to assess the strength and statistical significance of trends. This test determines if two variables are monotonically increasing or decreasing by ranking the variables and comparing their rank. The `scipy spearmanr` function is used in this work to calculate r_s.

For small numbers of *n* (i.e. the number of observations), statistical significance can be determined by comparing r_s to a corresponding critical value (r_{crit}). In this case, a non-directional null hypothesis is assumed, (i.e. H_0: ρ_s = 0 and there is no trend in the data) and H_0 can be rejected if $|r_s| \geq r_{crit}$. The degrees of freedom are calculated as *n - 2* and the corresponding critical values for an α = 0.01 significance level, from Weathington et al. (2012) is shown in Table B.1.

Table B.1: spearman rank test critical values for N and N - 2 degrees of freedom from Weathington et al. (2012)

N	N_{dof}	r_{crit} at α = 0.1
4	2	1.00
5	3	0.900
6	4	0.829
7	5	0.714
8	6	0.643

Acknowledgements

I would like to thank my supervisors, Ros and Sarah, for their unwavering support, mentorship and care throughout my career. I could not have completed my Masters during a pandemic if I did not have such incredible supervisors. I would also like to thank my collaborators from the LADUMA, RESOLVE, ECO and SIMBA teams for contributing their excellent data, resources and expertise to this project. In particular, the RESOLVE survey is supported by the NSF AST CAREER grant 0955368, PI S. Kannappan. Additionally, I would like to thank the National Astrophysics and Space Sciences Programme (NASSP) for funding my Masters.

I would like to thank my family and friends for all of the tea time, love and support throughout my degree. Lastly, I would like to thank the Almighty for His guidance on this path.

Bibliography

Aihara H., et al., 2011, The Astrophysical Journal Supplement Series, 193, 29

Alpaslan M., et al., 2014a, Monthly Notices of the Royal Astronomical Society, 438, 177

Alpaslan M., et al., 2014b, Monthly Notices of the Royal Astronomical Society, 440, L106

Alpaslan M., et al., 2015, Monthly Notices of the Royal Astronomical Society, 451, 3249

Aragón-Calvo M. A., Jones B. J. T., van de Weygaert R., van der Hulst J. M., 2007, Astronomy and Astrophysics, 474, 315

Aragón-Calvo M. A., Van de Weygaert R., Jones B. J., 2010a, Monthly Notices of the Royal Astronomical Society, 408, 2163

Aragón-Calvo M. A., Platen E., van de Weygaert R., Szalay A. S., 2010b, The Astrophysical Journal, 723, 364

Aragon Calvo M. A., Neyrinck M. C., Silk J., 2019, The Open Journal of Astrophysics, 2, 7

Baldry I. K., Glazebrook K., Brinkmann J., Ivezić Ž., Lupton R. H., Nichol R. C., Szalay A. S., 2004, The Astrophysical Journal, 600, 681

Benítez-Llambay A., Navarro J. F., Abadi M. G., Gottï Ober S., Yepes G., Hoffman Y., Steinmetz M., 2013, The Astrophysical Journal Letters, 763, 41

Berlind A. A., et al., 2006, The Astrophysical Journal Supplement Series, 167, 1

Blue Bird J., et al., 2020, Monthly Notices of the Royal Astronomical Society, 492, 153

Blyth S., et al., 2016, in MeerKAT Science: On the Pathway to the SKA. p. 4

Bok J., Skelton R. E., Cluver M. E., Jarrett T. H., Jones M. G., Verdes-Montenegro L., 2020, Monthly Notices of the Royal Astronomical Society, 499, 3193

Bond J. R., Kofman L., Pogosyan D., 1996, Nature, 380, 603

Burchett J. N., Elek O., Tejos N., Prochaska J. X., Tripp T. M., Bordoloi R., Forbes A. G., 2020, The Astrophysical Journal Letters, 891, L35

Cautun M., van de Weygaert R., Jones B. J. T., 2013, Monthly Notices of the Royal Astronomical Society, 429, 1286

Cautun M., Van De Weygaert R., Jones B. J., Frenk C. S., 2014, Monthly Notices of the Royal Astronomical Society, 441, 2923

Chen Y.-C., et al., 2017, Monthly Notices of the Royal Astronomical Society, 466, 1880

Codis S., Pichon C., Pogosyan D., 2015, Monthly Notices of the Royal Astronomical Society, 452, 3369

Davé R., Thompson R., Hopkins P. F., 2016, Monthly Notices of the Royal Astronomical Society, 462, 3265

Davé R., Anglés-Alcázar D., Narayanan D., Li Q., Rafieferantsoa M. H., Appleby S., 2019, Monthly Notices of the Royal Astronomical Society, 486, 2827

Dekel A., Silk J., 1986, Astrophysical Journal, 303, 39

Doroshkevich A. G., 1970, Astrophysics, 6, 320

Dressler A., 1980, The Astrophysical Journal, 236, 351

Eckert K. D., Kannappan S. J., Stark D. V., Moffett A. J., Norris M. A., Snyder E. M., Hoversten E. A., 2015, Astrophysical Journal, 810, 166

Eckert K. D., Kannappan S. J., Stark D. V., Moffett A. J., Berlind A. A., Norris M. A., 2016, The Astrophysical Journal, 824, 124

Eckert K. D., et al., 2017, Astrophysical Journal, 849, 20

Edelsbrunner H., Letscher D., Zomorodian A., 2000, in Proceedings 41st annual symposium on foundations of computer science. pp 454–463

Falco E. E., et al., 1999, Publications of the Astronomical Society of the Pacific, 111, 438

Forman R., 1998, Morse theory for cell complexes

Forman R., 2002, Transactions of the American Mathematical Society, 354, 5063

Fujita Y., 2004, Publications of the Astronomical Society of Japan, 56, 29

Giovanelli R., et al., 2005, The astronomical journal, 130, 2598

Gott III J. R., Jurić M., Schlegel D., Hoyle F., Vogeley M., Tegmark M., Bahcall N., Brinkmann J., 2005, The Astrophysical Journal, 624, 463

Gregory S. A., Thompson L. A., Tifft W. G., 1981, Astrophysical Journal, 243, 411

Gunn J. E., Gott III J. R., 1972, The Astrophysical Journal, 176, 1

Guo Q., Tempel E., Libeskind N. I., 2015, Astrophysical Journal, 800, 112

Hambly N., et al., 2008, Monthly Notices of the Royal Astronomical Society, 384, 637

Haynes M. P., Giovanelli R., 1984, Astronomical Journal, 89, 758

Hogg D. W., et al., 2003, The Astrophysical Journal Letters, 585, L5

Hopkins A., 2004, The Astrophysical Journal, 615, 209

Hoyle F., 1949, Central Air Documents Office, Dayton, OH, p. 195

Jarvis M. J., et al., 2017, arXiv preprint arXiv:1709.01901

Jonas J., MeerKAT Team 2016, in MeerKAT Science: On the Pathway to the SKA. p. 1

Kannappan S. J., 2004, Astrophysical Journall, 611, L89

Kannappan S., 2019, RESOLVE survey database tutorial, https://github.com/resolvesurvey/database-tutorial

Kannappan S. J., Wei L. H., 2008, in Minchin R., Momjian E., eds, American Institute of Physics Conference Series Vol. 1035, The Evolution of Galaxies Through the Neutral Hydrogen Window. pp 163–168, doi:10.1063/1.2973572

Kannappan S. J., et al., 2013, The Astrophysical Journal, 777, 42

Kauffmann G., et al., 2003, Monthly Notices of the Royal Astronomical Society, 341, 54

Kauffmann G., White S. D., Heckman T. M., Ménard B., Brinchmann J., Charlot S., Tremonti C., Brinkmann J., 2004, Monthly Notices of the Royal Astronomical Society, 353, 713

Kereš D., Katz N., Weinberg D. H., Davé R., 2005, Monthly Notices of the Royal Astronomical Society, 363, 2

Kleiner D., Pimbblet K. A., Jones D. H., Koribalski B. S., Serra P., 2016, Monthly Notices of the Royal Astronomical Society, 466, 4692

Kraan-Korteweg R. C., Cluver M. E., Bilicki M., Jarrett T. H., Colless M., Elagali A., Böhringer H., Chon G., 2016, Monthly Notices of the Royal Astronomical Society: Letters, 466, L29

Kraljic K., et al., 2017, Monthly Notices of the Royal Astronomical Society, 474, 547

Kraljic K., Davé R., Pichon C., 2020, Monthly Notices of the Royal Astronomical Society, 493, 362

Kuutma T., Tamm A., Tempel E., 2017, Astronomy and Astrophysics, 600, L6

Laigle C., et al., 2015, Monthly Notices of the Royal Astronomical Society, 446, 2744

Laigle C., et al., 2017, Monthly Notices of the Royal Astronomical Society, 474, 5437

Libeskind N. I., et al., 2018, Monthly Notices of the Royal Astronomical Society, 473, 1195

Luber N., van Gorkom J. H., Hess K. M., Pisano D. J., Fernández X., Momjian E., 2019, The Astronomical Journal, 157, 254

Malavasi N., et al., 2017, Monthly Notices of the Royal Astronomical Society, 465, 3817

Milnor J., 2016, Morse theory.(AM-51). Vol. 51, Princeton university press

Mo H., Bosch F. V. d., White S., 2010, Galaxy Formation and Evolution. Cambridge University Press

Moffett A. J., Kannappan S. J., Berlind A. A., Eckert K. D., Stark D. V., Hendel D., Norris M. A., Grogin N. A., 2015, Astrophysical Journal, 812, 89

Moore B., Katz N., Lake G., Dressler A., Oemler A., 1996, nature, 379, 613

Morrissey P., et al., 2007, The Astrophysical Journal Supplement Series, 173, 682

Odekon M. C., Hallenbeck G., Haynes M. P., Koopmann R. A., Phi A., Wolfe P.-F., 2018, The Astrophysical Journal, 852, 142

Peebles P. J. E., 1969, Astrophysical Journal, 155, 393

Peng Y.-j., et al., 2010, The Astrophysical Journal, 721, 193

Porciani C., Dekel A., Hoffman Y., 2002, Monthly Notices of the Royal Astronomical Society, 332, 325

Santiago-Bautista I., Caretta C. A., Bravo-Alfaro H., Pointecouteau E., Andernach H., 2020, Astronomy & Astrophysics, 637, A31

Sarron F., Adami C., Durret F., Laigle C., 2019, Astronomy and Astrophysics, 632, A49

Schaap W. E., van de Weygaert R., 2000, Astronomy and Astrophysics, 363, L29

Skrutskie M., et al., 2006, The Astronomical Journal, 131, 1163

Sousbie T., 2011, Monthly Notices of the Royal Astronomical Society, 414, 350

Sousbie T., 2013, Manual, http://www2.iap.fr/users/sousbie/web/html/index4f3e.html?category/Manual

Sousbie T., Pichon C., Kawahara H., 2011, Monthly Notices of the Royal Astronomical Society, 414, 384

Spearman C., 1904, The American Journal of Psychology, 15, 72

Springel V., et al., 2005, Nature, 435, 629

Springob C. M., Haynes M. P., Giovanelli R., Kent B. R., 2005, The Astrophysical Journal Supplement Series, 160, 149

Stark D. V., et al., 2016, The Astrophysical Journal, 832, 126

Tempel E., Libeskind N. I., 2013, Astrophysical Journal Letters, 775

Tempel E., Stoica R. S., Saar E., 2013, Monthly Notices of the Royal Astronomical Society, 428, 1827

Tempel E., Stoica R. S., Martínez V. J., Liivamägi L. J., Castellan G., Saar E., 2014, Monthly Notices of the Royal Astronomical Society, 438, 3465

Toomre A., Toomre J., 1972, Astrophysical Journal, 178, 623

Verdes-Montenegro L., Sulentic J., Lisenfeld U., Leon S., Espada D., Garcia E., Sabater J., Verley S., 2005, Astronomy & Astrophysics, 436, 443

Weathington B. L., Cunningham C. J., Pittenger D. J., 2012, Understanding business research. John Wiley & Sons

Welker C., et al., 2019, Monthly Notices of the Royal Astronomical Society, 491, 2864

White S. D. M., 1984, Astrophysical Journal, 286, 38

WikipediaCommons 2013, A Delaunay triangulation with circumcircles by Gjacquenot, https://commons.wikimedia.org/w/index.php?curid=30370476

Zel'Dovich Y. B., 1970, Astronomy and Astrophysics, 500, 13

Zeldovich I. B., Einasto J., Shandarin S. F., 1982, Nature, 300, 407

van de Weygaert R., Schaap W., 2009, The Cosmic Web: Geometric Analysis. Springer Berlin Heidelberg, Berlin, Heidelberg, p. 291, doi:10.1007/978-3-540-44767-2_11, https://doi.org/10.1007/978-3-540-44767-2_11